Volumetric Additive Manufacturing of Arbitrary Three-Dimensional Geometries in Photopolymer Materials

By

Brett Edward Kelly

A dissertation submitted in partial satisfaction of the

requirements for the degree of

Doctor of Philosophy

in

Engineering - Mechanical Engineering

In the

Graduate Division

of the

University of California, Berkeley

Committee in Charge:

Professor Hayden K. Taylor, Chair
Professor Tarek I. Zohdi
Professor Laura Waller

Fall 2018

Abstract

Volumetric Additive Manufacturing of Arbitrary Three-Dimensional Geometries in Photopolymer Materials

By

Brett Edward Kelly

Doctor of Philosophy in Engineering - Mechanical Engineering

University of California, Berkeley

Professor Hayden Taylor, Chair

Additive manufacturing (AM) capabilities are rapidly expanding and AM is increasingly used for the production of end-use and multi-component parts. The field of AM now encompasses technologies that rely on a broad range of process physics, from which the ASTM has delineated 7 distinct categories. The term "3D printing" is often used synonymously with additive manufacturing to describe systems that build parts of custom 3D geometry on demand. While the final parts produced by 3D printing are three-dimensional, the printing processes typically rely on serial repetition of unit printing operations of dimensionality less than three. Three-dimensional parts are built up point-by-point or layer-by-layer.

This thesis covers the design, implementation, and development of new methods for volumetric or volume-at-once additive manufacturing, where entire complex three-dimensional geometries are printed all together. After an introduction to the current state of additive manufacturing in Chapter 1, Chapter 2 presents a background and modeling of photopolymer chemistry, which is leveraged to develop the novel manufacturing methods discussed in detail in Chapters 3 and 4. In addition to development of the core operating principles behind these technologies, this thesis presents demonstrations of printed components and manufacturing capabilities. Potential applications spaces are discussed with proof-of-concept demonstrations in bioprinting and multi-process AM. These include printing of soft (~1-10kPa stiffness) hydrogel structures along with a demonstration of a novel "overprinting" capability that prints complex polymer geometries onto pre-manufactured metal components.

The concluding chapter (5) discusses current capabilities and limitations of these novel processes and looks ahead toward further development directions.

Table of Contents

Acknowledgements

The Author of this thesis would like to thank a number of people who have contributed to the work presented herein. First and foremost, I would like to thank my academic Advisor, Hayden Taylor, for the tremendous support and guidance throughout the course of this thesis work. I would also like to thank my co-advisor, Tarek Zohdi.

I would like to thank both the Center for Engineering Materials and Manufacturing (CEMM) at Lawrence Livermore National Laboratory (LLNL) and the Design for Nanomanufacturing group at the University of California, Berkeley. I would specifically like to acknowledge useful discussions with and support from Maxim Shusteff, Robert Panas, Allison Browar, James Oakdale, and Ryan Hensleigh at LLNL as well as with Indrasen Bhattacharya, Hossein Heidari, Prof. Laura Waller, and Prof. Ren Ng at Berkeley.

Some of the work in this thesis was performed at LLNL as part of a research collaboration. This work was performed under the auspices of the U.S. Department of Energy of Lawrence Livermore National Laboratory under Contract DE-AC52-07NA27344. This work was performed under LDRD funding 14-SI-004, and 17-ERD-116. This document has been released under IM review #LLNL-TH-753780.

Chapter 1 Introduction

This thesis presents the invention and reduction to practice of a novel manufacturing method. To position this new method within the broad context of manufacturing, we can first consider historical drivers that have led to prior innovation in manufacturing. Dornfeld *et al.* (*1*,*2*) describe five "Ages of Manufacturing" as illustrated in Figure 1-1. During the Industrial Revolution, manufacturing process innovation was driven by a call for mass production of standardized parts. This led to major early innovations in machines and machine tools to replace craft production, which was performed mostly by hand. With the advent of computers and digital design, demand has begun to revert to agile, rapid production, on demand.

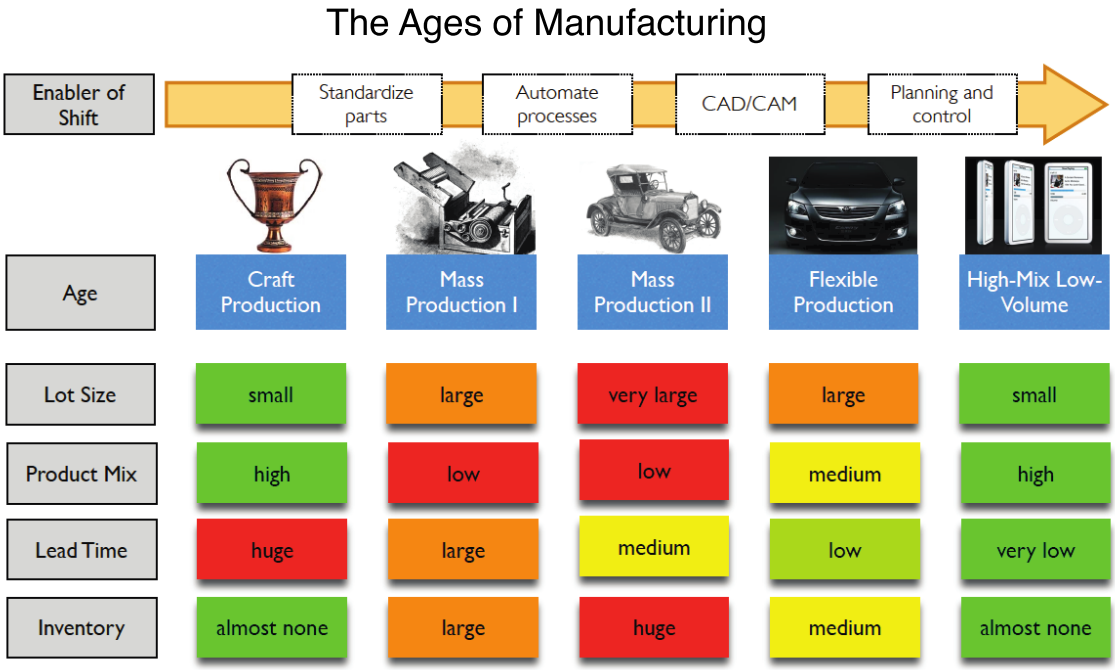

Figure 1-1 Schematic to describe the ages of manufacturing, drivers of major shifts, and characteristics of common manufacturing processes in each age. Adapted from (*2*).

The recent trend toward mass customization in manufacturing has been followed by the development of additive manufacturing technologies. *Additive manufacturing*, in this thesis considered generally synonymous with the other commonly used terms *3D printing* and *Solid Freeform Fabrication (SFF)*, refers to a paradigm in manufacturing where objects are constructed by adding or forming material only where it is desired. In contrast, more conventional methods such as machining tend to operate starting from a solid structure and selectively cutting away material to form a 3D geometry. From the use of cutting operations to remove material, we categorize such methods as "subtractive". Other commonly used

manufacturing methods, for example injection molding processes commonly used in the mass production of plastic components, form material, often through applying heat and forces, into the final part geometry. Because they start with roughly the same volume of material that goes in to the final part, and simply re-form its geometry, we classify such methods as "conservative". Once again, in the past several decades, we've entered a realm where parts are produced by "additive" manufacturing methods.

Since the inception of "Stereolithography" in 1984 (*3*), the umbrella of additive manufacturing (AM) has grown to now include a diverse set of technologies which build up parts by exploiting a range of physical phenomena. The ASTM standards organization has now delineated AM printing processes into 7 broad categories (*4*) based on the underlying physical operations by which they create parts. The categories include "vat photopolymerization", "powder bed fusion" (PBF), "binder jetting", "material jetting", "sheet lamination", "material extrusion", and "directed energy deposition" (DED). These processes bring capabilities in printing of a wide range of materials including polymers, metals, and ceramics.

Vat photopolymerization methods operate by selectively solidifying a precursor polymer material by spatially controlled optical illumination, a process central to the work in this thesis. Material is converted from liquid to solid by formation of chemical bonds between pre-cursor molecules upon exposure to light. Powder Bed Fusion includes processes where plastic or metal particles are fused by heating with a laser. Material and binder jetting respectively jet end material or binder material from a nozzle to trace out 3D parts in space (material jetting) or in a powder material (binder jetting). Sheet lamination includes processes that add layers of material by a cutting process, followed by a layer adhesion process to stack 2D layers into a 3D geometry. Material extrusion techniques operate through selective extrusion of a material, often by heating of a thermoplastic, to trace out a 3D geometry. Finally, Directed Energy Deposition refers to processes where a filament of material, generally a metal, is selectively positioned by delivery of a large energy dose to convert the material. Processes in each of these categories contribute to the flexibility of additive manufacturing today.

To date, we have seen additive methods transform a number of manufacturing processes, in applications areas including, but not limited to patient-specific medical devices (*5*,*6*), bioprinting (*7*), optical components (*8*,*9*), apparel (*10*), microfluidic devices (*11*), aerospace engine components (*12*), assembly fixtures (*13*), tooling for conventional manufacturing methods (*14*) and "Do-it-yourself 3D printing" (*15*). Increasingly, AM is used for the production of end-use and multicomponent parts (*16*).

1.1 Capabilities of Additive Manufacturing

1.1.1 Benefits of AM

Additive manufacturing brings a number of fabrication advantages compared to more conventional subtractive methods such as CNC machining and material conservative processes such as injection molding. With AM, parts can often be

rapidly generated from CAD files in hours. Tooling is eliminated in most additive processes, which leads to considerable time savings as well as major cost savings. Custom tooling, such as that required in an injection molding process, can often take days or weeks to produce and requires capital-intensive machining operations. Labor costs can also be reduced by using additive techniques as machine operation is simplified. For these reasons, AM has become very popular for rapid prototyping of new designs. While many additively manufactured parts still fail to meet the mechanical requirements of end use parts, this is an active area of research and development.

In addition to speed and cost benefits, AM brings interesting benefits in the types of things that can be manufactured. AM has in some cases served to change the way that parts are designed (*17*), as manufacturing constraints become relaxed and new geometries become possible. As one example, AM can allow parts that were previously manufactured in a series of machining operations (for example, cutting, welding, drilling) to be printed in a single step. Moreover, parts can be completely redesigned for additive manufacturing. For example, AM enables the manufacture of complex lattice structures that can give rise to previously unattained properties. These include properties such as increased strength-to-weight and negative Poisson's ratio (*18*,*19*).

As alluded to at the outset, many AM methods also provide a reduction in material use and waste as typically material is placed selectively, only where needed, in the final part in contrast to machining methods which cut away material that often becomes waste. AM can also contribute to sustainability of manufacturing operations by distributing digital design and manufacturing and reducing the need for transport or parts.

1.1.2 Drawbacks of AM

Briefly, it should also be mentioned that there do exist areas where AM presents drawbacks relative to more conventional manufacturing operations. For example, for long production runs of plastic parts, it is still typically more economical to use an injection molding process compared to an AM process. While the upfront cost of custom tooling is high, the per-part cost in injection molding is much lower than for AM. This arises in part due to the typically higher cost of materials in AM materials resulting from high-energy requirements in creating stock material. Powders for sintering operations, for example, must be remelted twice and then sintered in an energy-intensive laser process. Additionally, additively manufactured parts still face quality challenges arising from the printing process itself. In sintered parts, porosity can lead to weaker mechanical properties. Similarly, the layered nature of most printing processes often gives rise to mechanical anisotropy in printed parts. This thesis will present a route to addressing some of these challenges

1.2 Dimensionality of Printing Operations

As introduced at the start, it is logical to categorize the broad range of current AM technologies existing today by the underlying physics through which they operate. The underlying physics can lead to certain advantages and limitations of each process. In this thesis, however, to introduce the major prominent AM technologies developed to date, we choose to categorize by a different means. Rather than binning based on the physical principles of printing, we chose to do so instead by the geometric dimensionality (defined through this chapter) of the unit printing operation of the AM process.

3D printing, again considered synonymous with the term additive manufacturing, looks to produce three-dimensional parts from digital designs. The term "***3D*** printing" itself implies this dimensionality. We argue, however, that this description of dimensionality more accurately represents the final part itself, rather than the physics of printing. The reason for categorization by dimensionality of printing operation rather than process physics serves to motivate the core contribution of this thesis – an increase in the dimensionality and complexity of unit printing operations in 3D printing.

1.3 Current Methods: 0D Point-by-Point

The vast majority of AM technologies developed to date operate with a similar dimensionality to some of the early developments in 3D printing technology where the three-dimensional geometry is traced out point-by-point. The process begins with design of 3D part geometry, represented in a digital file. Typically, the digital file is sliced to create a set of 2D "layers" which will be used to form the 3D part. Intermediate steps to select orientation of the part in the build volume and to add support structures to aid in printing may also occur and will be touched on more closely in later chapters.

1.3.1 Inkjet Printing

To more clearly illustrate the concept of unit printing dimensionality, we examine the physics of a process from which it seems the term "3D printing" has arisen. The process, inkjet printing, operates based on similar physics to "2D" inkjet printing used to deposit inks onto paper, and falls under the ASTM category of *material jetting*. In this process, a liquid material is deposited from a small nozzle and rapidly solidified by UV light upon exiting the nozzle. Material solidification occurs by a process called photopolymerization where a liquid polymer becomes solid upon exposure to light. This photopolymerization process is described extensively in Chapter 2, and utilized throughout this thesis. The inkjet 3D printing process typically begins by printing the first layer of the sliced 3D file. To perform printing, the nozzle is translated in the lateral (x and y as depicted in Figure 1-2) dimensions and material is deposited and solidified point-by-point to trace out the 2D layer. While this layer itself is three-dimensional, we describe it as effectively two-dimensional as the spatial extent in the vertical dimension (z) is typically

orders of magnitude smaller than the x and y extent of the object. Similarly, while droplets of material jetted from the nozzle are three-dimensional, we categorize inkjet printing as a having a 0D (point) unit printing operation. Each discrete unit volume, or "voxel," of the 3D part geometry must be traced out sequentially.

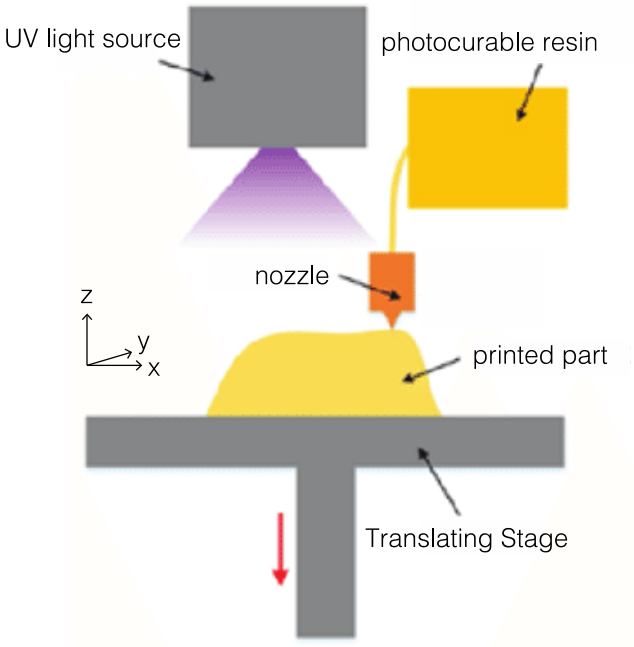

Figure 1-2 Schematic of the inkjet printing process. Liquid photopolymer material is jetted from a nozzle and rapidly photocured. The 3D geometry is traced out point-by-point, layer-by-layer. Figure adapted from (*20*)

1.3.2 Stereolithography (SLA)

While the term "printing" likely comes from the introduction of 3D inkjet printing, the widely regarded invention of additive manufacturing can be credited to Charles Hull, founder of 3D Systems. Hull's invention originates from his 1984 patent entitled "Apparatus for production of three-dimensional objects by stereolithography" (*3*). The term stereolithography (SLA) is still used today to describe processes similar to the original invention (e.g. (*21*,*22*)). Like inkjet printing, this process operates based on the physics of photopolymerization. Other process physics differ, however, causing it today to fall under the ASTM category of *vat photopolymerization*. In a stereolithography system, there is no nozzle to deposit material. Instead, an entire 3D volume, or vat, is filled with a convertible liquid material. Similar to the inkjet process, the 3D geometry is still traced out point-by-point, and layer-by-layer. However, in the case of SLA, the pointwise tracing involves x, y translation of a focused laser beam, often controlled by a mirror and galvanometer. The focused beam triggers the photopolymerization reaction locally. After printing of the first layer, typically a base stage is translated in the z dimension to allow for printing of subsequent layers. This z translation is also performed in the

inkjet process, as well in as a majority of AM technologies that utilize point-by-point (0D unit operation) printing.

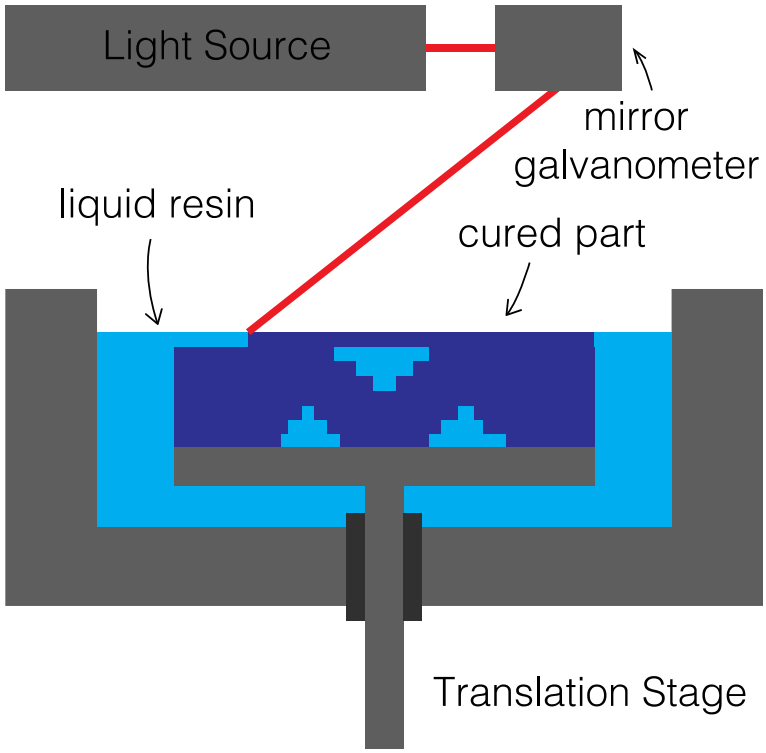

Figure 1-3 Schematic of a typical stereolithography (SLA) printing system. A light source (typically a laser) is focused to a point at the surface of a resin volume. Material is cured at this in voxels, point by point, to trace a layer. A translation stage moves the printed part down to expose the next layer of material

1.3.3 Selective Laser Sintering

A third major category of print technology which utilizes pointwise scanning is described by the term Selective Laser Sintering (SLS) (*23*). SLS is a *powder bed fusion* process as categorized by the ASTM standard. As alluded to in the category naming, this process begins with a bed of fine power particles. The particles can be plastic or metal, and in some cases ceramic. Note that when metals are used, the process typically falls under a slight modified naming: Direct Metal Laser Sintering (DMLS). In all cases, a focused laser beam is used, similar to the stereolithography process described in Section 1.3.2. In the case of SLS, however, the laser is utilized to heat and fuse the powder particles to build up the solid structure. Like the SLA process, the laser is scanned in x and y to trace out 2D layers. Again, between printing of subsequent of 2D layers, the z stage is translated and powder is typically replenished by a roller or sweeping blade. A schematic of this process, adapted from (*24*), is shown in Figure 1-4.

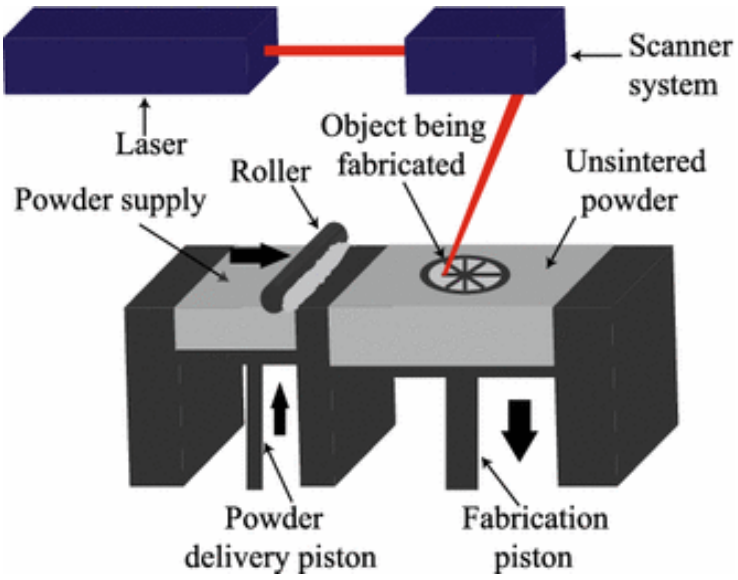

Figure 1-4 From (*24*). Schematic of a typical Selective Laser Sintering (SLS) powder bed process. A laser joins powder particles by sintering and trances out 3D geometries point-by-point. A roller is used to introduce fresh powder to the build volume between sintering of subsequent layers.

1.3.4 Fused Filament Fabrication (FFF)

Another common set of technologies which print parts point-by-point are those which fall under the term Fused Filament Fabrication (FFF). This term is used to refer to additive manufacturing methods that operate based on selective deposition of a thermoplastic material. The solid polymer material is heated above its melting temperature and extruded through a nozzle. The material rapidly cools following extrusion to return to a solid form. This process is one of the most ubiquitous 3D printing technologies in industry today and is more often referred to by its trademarked name "Fused Deposition Modeling" and the acronym FDM (*25*). This trademark is held by Stratasys, whose founder S. Scott Crump is credited with invention of the technology through his 1989 patent entitled "Apparatus and method for creating three-dimensional objects" (*26*). Today, when hearing the term "3D printing," many people envision the low-cost desktop FDM machines that were popularized during the "RepRap" movement of the mid 2000's. FFF/FDM falls under the ASTM category of *material extrusion*.

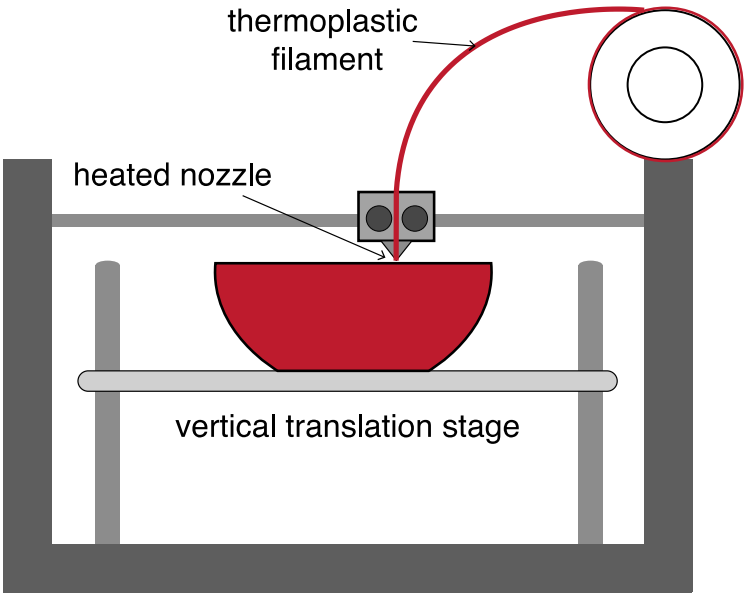

Figure 1-5 Schematic of a fused filament fabrication (FFF) or fused deposition modeling (FDM) process. A thermoplastic filament is fed through a heated nozzle to selectively deposit material point-by-point. A stage moves the printing part down to allow for printing of subsequent layers.

1.3.5 Direct Ink Writing

A second technique that falls under *material extrusion* involves a nozzle-based process similar to FFF. This process is commonly referred to by the name "direct ink writing" (DIW) (*27*,*28*). Again, in a DIW process, material is extruded through a nozzle which traces out the 3D geometry point-by-point. The core difference from FFF is that in a DIW process, the extruded material is not heated. Instead, the material is forced through the nozzle by an applied pressure only. The process relies on a shear thinning behavior of the material, where viscosity decreases at increased shear rates. The ability to print with thermosetting materials brings an advantage compared to FFF. However, challenges exist in developing materials with appropriate rheological properties.

1.3.6 Layerless Pointwise Printing

It should be pointed out briefly that some pointwise methods are able to trace out geometries following three-dimensional tool paths rather than scanning layer-by-layer. One example are multi-photon direct-write technologies (*29*–*33*). These are similar to the SLA process, but used to achieve finer resolution by exploiting non-linear absorption of multiple photons simultaneously. In this process, the focused beam can be used to trace a geometry below the surface of a liquid resin. Another approach which can achieve layerless pointwise printing involves extrusion into self-healing gels (*34*). Finally, Directed Energy Deposition metal printing techniques also utilize layerless pointwise printing.

1.4 Current Methods: 1D Line-at-Once

While many additive manufacturing technologies, including the aforementioned in Section 1.3, build up 3D parts point-by-point through repetition of a unit printing operation which is effectively zero-dimensional, there is a set of technologies which increase the unit dimensionality by one. These systems print a line of material (much thinner in 2 of the 3 dimensions) in a single step.

1.4.1 Multi-Jet Material Jetting

One example of a "line-at-once" printing technology is a process very similar to inkjet printing. Instead of jetting material point-by-point through a single nozzle, multi-jet material jetting technologies utilize a set of nozzles, typically arranged in a linear fashion. This serves to increase throughput in printing of layers and also enables printing of multiple materials in a single build. Stratasys's "PolyJet" technology underlies a line of popular commercial 3D printing systems that are able to print with a range of materials properties and colors within a single part.

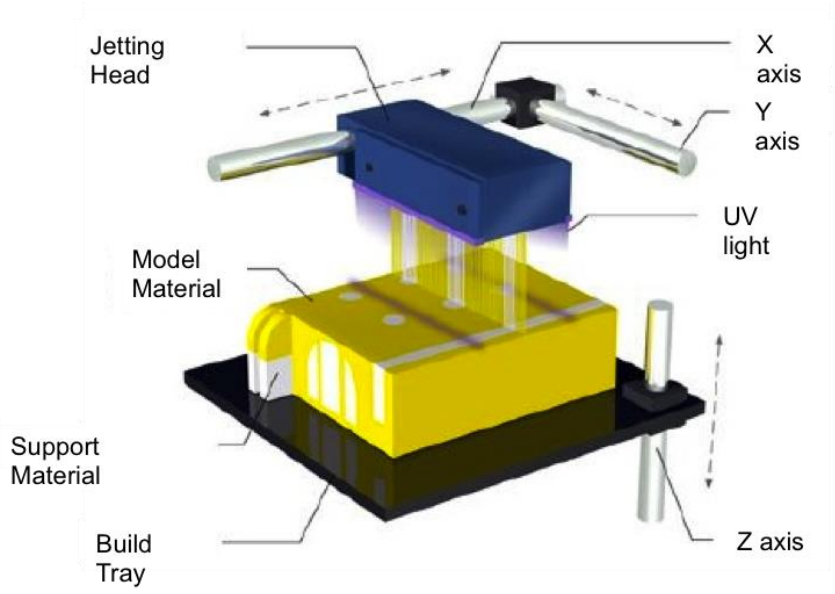

Figure 1-6 Schematic of the Stratasys Polyjet technology which utilizes material jetting from an array of nozzles to build up 3D parts line-by-line. Image adapted from stratasys.com

1.4.2 Binder Jetting

The unit printing operation deployed in binder jetting technologies is quite similar to that in the material jetting process. In the binder jetting case, the jetted material is not the final part material, but rather a binder that is used to join particles of the final material. Like multi-jet material jetting, the binder can be jetted

from multiple nozzles in a line. Hewlett-Packard's Multi-jet Fusion technology is an example of an emerging commercial system that utilizes binder jetting principles.

1.5 Current Methods: 2D Layer-at-Once

To take the next step in increased dimensionality of unit printing operations requires printing of an entire (2D) layer in a single step. This is achieved by a smaller number of technologies, which are mostly optics-based, described in the following sections.

1.5.1 Projection Stereolithography

The most commonly used layer-at-once 3D printing technology can be described by the term projection stereolithography (*35*–*38*). As alluded to in the name, this technology operates using projected optical images. In this thesis, we define a projection as a two-dimensional real image with controlled image intensity. In a projection stereolithography system, projections are typically generated by digital micro-mirror devices which modulate intensity pixel-by-pixel by rapid switching of individual micro mirrors. The process of creating a real image from a digital file in this manner, which also involves additional optics and control, is typically called Digital Light Processing (DLP) and the industry term for the printing technology has come to be DLP printing. DLP is the same technology used in most consumer movie projectors. In the printing process, a 2D image generated by the projector is focused at the surface of a vat of photopolymer material and an entire slice or 2D layer of the polymer is converted in a single step. Aside from the increased dimensionality of the printing operation, the process is very similar to the stereolithography process described in Section 1.3.2 where a base stage is translated linearly between printing of subsequent layers. A schematic of the process is given in Figure 1-7.

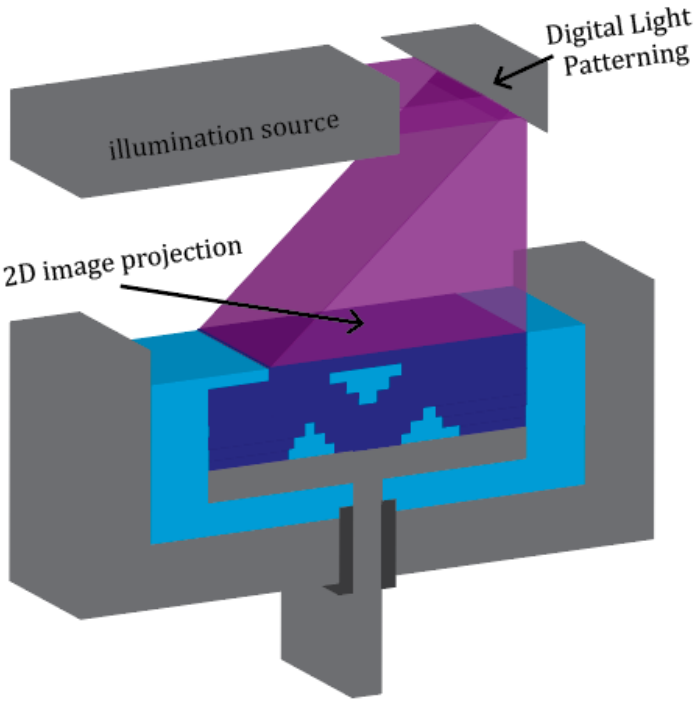

Figure 1-7 Simple schematic of a typical projection stereolithography or DLP printing system. A patterned two-dimensional image is formed, usually by a digital micromirror device or spatial light modulator, and focused to the surface of a photopolymer resin vat to cure a layer the 3D part in a single step. A linear translation stage is used to dip the part into the resin for printing of the next layer.

1.5.2 Continuous Digital Light Printing

At the present, it has become more common in vat photopolymerization technologies to illuminate the resin volume from the bottom and build the 3D part from the bottom-up (*39*,*40*) rather than from the top-down type configuration depicted in Figure 1-3 and Figure 1-7. In some DLP printing technologies, the bottom-up approach is combined with the use of an oxygen-permeable, optically transparent window between the incident illumination and the build volume. Oxygen generally acts to inhibit photopolymerization reactions (*41*,*42*) as explained in Chapter 2. Some DLP techniques have leveraged the inhibiting property of oxygen to generate a "dead zone" where curing is inhibited just above the window in the photopolymer vat. The window is typically made of materials such as PDMS or Teflon. Creation of the dead zone prevents adhesion between the curing part and the window, which makes the bottom up process much faster by eliminating the need for a step to separate the cured layer from the substrate. Pressure from the fluid vat can drive faster replenishment of resin compared to the top down approach. In some cases, this can enable continuous translation of the curing structure (*43*–*45*) to print potentially smoother, more isotropic parts with reduced prominence of layering artifacts. In this thesis, we call this process Continuous Digital Light Printing (CDLP). While the continuous process addresses some of the

drawbacks that arise from printing with discrete layers, the underlying unit printing operation is still effectively two-dimensional, as thin slices of material are added serially.

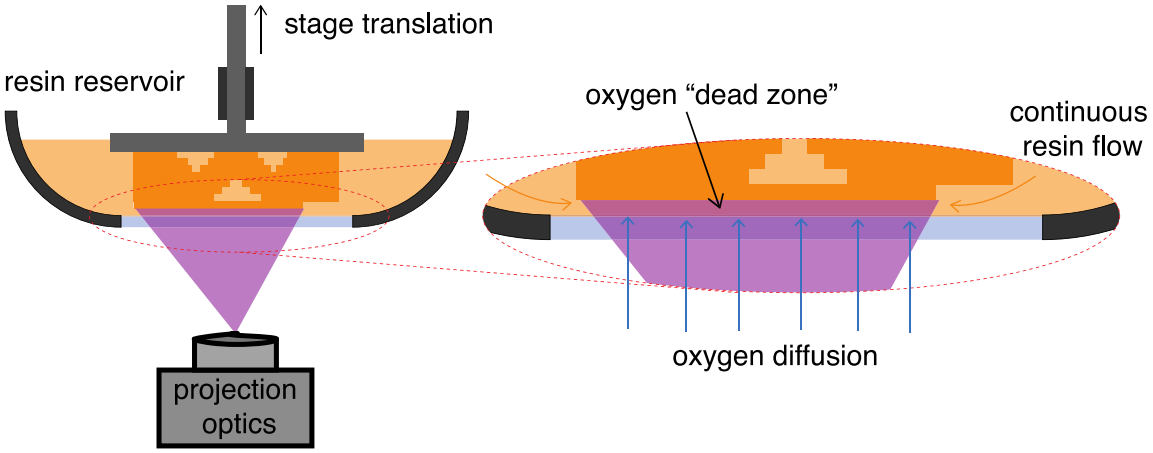

Figure 1-8 System schematic for Continuous Digital Light Printing (CDLP) manufacturing process. Two-dimensional images are projected from the bottom of the build volume through a transparent, oxygen permeable window. Oxygen diffusion through the window creates a dead zone where curing is inhibited. This allows for the part to be raised continuously as new resin flows continuously to refill the dead zone.

1.6 Current Methods: 3D Volume-at-Once

The final step in the evolution of dimensionality of unit operations in 3D printing is to create a system where entire volumes of material are formed in a single step. There do exist a very small range of capabilities in volume-at-once 3D printing. These capabilities at the moment are largely confined to work in interference lithography (*46–48*). Interference lithography follows a similar physics of photopatterning to that utilized in SLA/DLP/CDLP systems but instead generates three-dimensional intensity patterns within a photoresist to cure a 3D part all at once. While the unit printing operation can be said to be three-dimensional, the types of structures that are created are very different from those required in AM. For one, the size scale is much smaller. Feature sizes and structures are at the micron and sub-micron scales. At these scales absorption of light through the volume is tolerable as the depth for which light needs to penetrate is exceedingly small. Additionally, interference-based approaches are highly constrained in the geometries that are possible to produce. Periodic structures with limited complexity are achievable but the geometric customization, a core benefit of AM, is not realized in these systems.

1.7 Contributions of This Thesis

The goal of this thesis was to develop a technology that could make 3D printing truly three-dimensional. This meant to create an apparatus capable of

forming entire 3D objects of customized geometry all at once rather than point-by-point, line-by-line, or layer-by-layer. This was achieved by leveraging knowledge of photopolymer kinetics (Chapter 2) and computational imaging to invent the volumetric printing technologies described in Chapters 3 and 4. The result is a new paradigm in additive manufacturing where parts are printed as a whole. This leads to immediate advantages in print speed, smoother surfaces, and eliminated need or sacrificial support structures. Additional advantages and capabilities are described in Chapter 4 and new avenues of development from this baseline are presented are presented in Chapter 5 along with a comparison to lower-dimensional printing technologies.

Chapter 2 Photopolymer Kinetics

In this Chapter, the foundations and physics of photopolymerization are examined and modeled. This serves to form the basis for the development of new technologies whose experimental printed results are demonstrated in Chapters 3 and 4. In this thesis, the term photopolymerization refers to processes by which solid structures are formed from a liquid or solid precursor polymer material via interaction with incident light energy. The vast majority of the work in this thesis considers functionalized acrylate photopolymers which exhibit similar curing kinetics. The modeling framework presented is developed to be general enough for application to a wide range of photocuring chemistries with appropriate fitting of model parameters.

2.1 Stereolithography Working Curves

A baseline understanding of the interaction between incident optical illumination and resin photochemistry in a stereolithographic processes can be gathered from the derivation of the working curves in stereolithography by Paul Jacobs (*49*,*50*). This work is widely cited as the basis for modeling of curing processes in stereolithography. The first core assumption in Jacobs' model is that light absorption through the photopolymer resin follows the Beer-Lambert exponential attenuation law. Jacobs writes this law in terms of the penetration depth D_p, a resin parameter, as

$$I(x,y,z) = I(x,y,0)e^{-z/D_p} \tag{2.1}$$

Equation 2.1 gives the irradiance of the source at a particular point within a 3D resin volume $I(x,y,z)$ as a function of the irradiance at the surface of the resin at a particular point in the lateral $(x,y,0)$ plane where the laser is scanning. Figure 2-1 shows the coordinate system convention used.

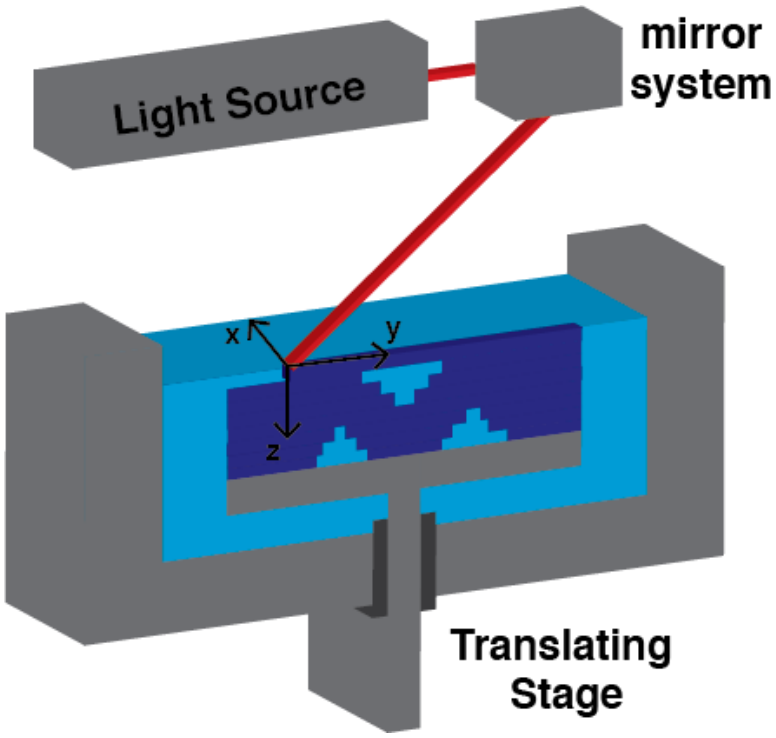

Figure 2-1 Stereolithography coordinate system used to in Jacobs model

For the purpose of illustrating the Jacobs model, and as a convention for the rest of this thesis, the exposure dose E at a particular point within the 3D volume will be defined as the time integral of the irradiance at that location within the 3D volume through the entire curing process and is given by Equation 2.2

$$E(x,y,z) = \int_0^{t_{exp}} I(x,y,z)dt \tag{2.2}$$

Jacobs assumes that a critical energy dose E_{crit} is required at any point within the resin volume for the material to convert from liquid to solid. In Jacobs' stereolithography case, laser intensity is always highest at the surface of the resin and the depth of cure C_d can be written as a function of the exposure dose E, critical dose, and the penetration depth as given in Equation 2.3. This equation forms the basis of the widely used stereolithography "working curves" shown in Figure 2-2.

$$C_d = D_p * \ln\left(\frac{E}{E_{crit}}\right) \tag{2.3}$$

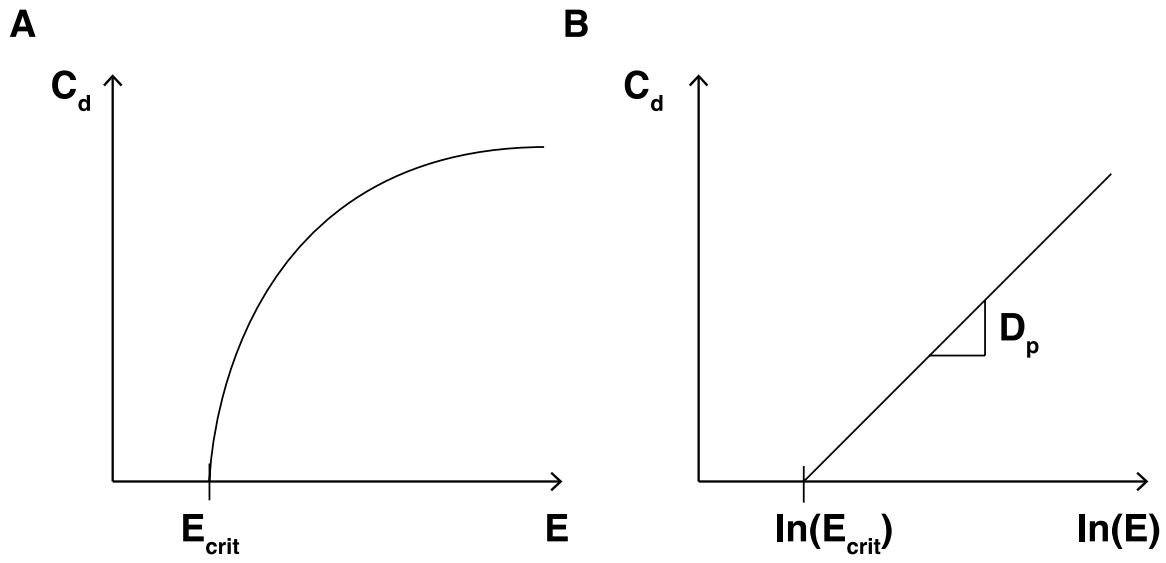

Figure 2-2 (A) An example of a Jacobs stereolithography working curve showing the dependence of the cure depth on the exposure dose delivered to the material. **(B)** The same curve plotted on log-linear axes showing the effect of the penetration depth on cure depth.

2.2 Model Development

Section 2.1 presents the basics of the Jacobs model, which is widely used in stereolithography. While the full model (*50*) does account for Gaussian spreading of the incident laser source, the Jacobs analysis still considers only a single point within the curing layer. When considering simultaneous illumination of multiple features within a printing layer (as in the case of the aforementioned layer-at-once photocuring systems described in Section 1.5) we observe effects of interaction between curing features. This is especially prominent in resin formulations with low viscosities and/or small molecules as molecular diffusion can influence curing dynamics. Additionally, the Jacobs assumption of a critical exposure dose being necessary to convert the material leaves out some physics. In this section, a coupled reaction-diffusion model is implemented to explore the effects of curing a material layer with complex geometry all at once. A 2D simulation is used to consider a single layer but is modified to include a third dimension for the volumetric curing processes considered in Chapters 3 and 4. In this chapter, we consider a hydrogel material with low viscosity as experimental validation for the 2D reaction-diffusion model. The model considers eight chemical species, which make up the photopolymer formulation. The first species include a photoinitiator molecule in one of two states: 1) a stable, unreacted form, and 2) a photoactivated radical form. We consider the acrylate polymer end groups to occupy one of four possible states. Finally, we consider photoinhibitor species. These include both those that can be mixed into the formulation, as well as oxygen, which can be dissolved within the formulation at ambient conditions. A description of each species along with labeling conventions is provided in Table 1.1.

Table 1.1 - Chemical species considered in the computational model along with naming conventions used in this report**.** The letter I represents the initiator molecule. P represents the prepolymer. Q represents an inhibitor molecule or quencher.

Species label	Description
Initiator States	
$\boldsymbol{I}$	Stable photoinitiator. Unreacted.
$\boldsymbol{I_r}$	Radical photoinitiator species
End Group States	
$\boldsymbol{P_0}$	Unreacted prepolymer end group.
$\boldsymbol{P_1}$	Radical prepolymer end group. Formed by reaction with I_r species
$\boldsymbol{P_2}$	Prepolymer end group which has bonded with another end group to form a cross-link
$\boldsymbol{P_3}$	"Dead" prepolymer end group. No crosslink has been formed. No crosslink can be formed at this site. Covers multiple distinct chemical states that have the same effect.
Inhibitor States	
$\boldsymbol{O_2}$	Ambient oxygen. Acts as a radical quencher in reactions with I_r and P_1.
$\boldsymbol{Q}$	Radical quencher or photoinhibitor molecule added to the solution.

2.2.1 Initiation

The first reaction considered in this photopolymerization model is the dissociation or photolysis of the initiator species as depicted in Figure 2-3A, This step involves a reaction between a photon with a particular energy level $h\nu$ ($h =$ Planck's constant, $\nu =$ is the frequency of incident light) and a stable initiator molecule I. The reaction generates a pair of reactive radical initiator species I_r.

$$I + h\nu \rightarrow 2I_r \tag{2.4}$$

The specific chemical products of this reaction are dependent on the particular photoinitiator molecule used and the wavelength of the illuminating source. In some cases, only one reactive radical is formed. In others, the two generated species may not be considered equally reactive. With the photoinitator used in this chapter (Irgacure 2959), the reaction is considered to produce two equally reactive radicals.

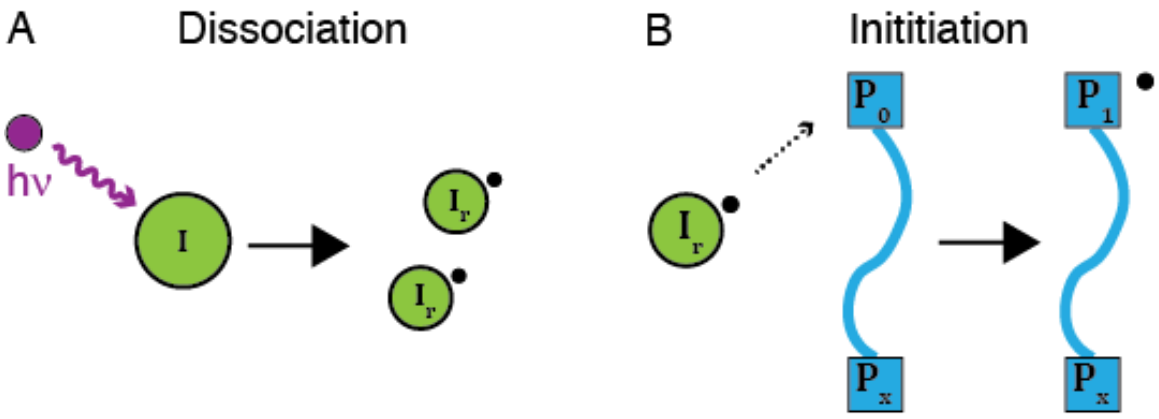

Figure 2-3 Schematic of the initiation phase of photopolymerization for a type 1 photoinitiator. (A) The dissociation step involves absorption of a photon by a stable photoinitiator molecule and cleavage into two radical species. (B) The initiation step where a polymer radical is formed by reaction between a radical initiator molecule and a stable polymer functional group.

The rate at which the dissociation reaction occurs has been modeled previously in literature (*51*,*52*) and is included as given in Equation 2.5.

$$R_D = \frac{\phi\epsilon}{N_A h\nu}[I](x,y,z)I_s(x,y,z) \tag{2.5}$$

In Equation 2.5 ϕ refers to the quantum yield or number of cleavage events per photon absorbed, ϵ is the molar absorptivity of the initiator molecule ($\epsilon = 4$ $M^{-1}cm^{-1}$ for I2959 at 365nm (*52*)), N_A is Avogadro's number, $[I]$ the concentration of the stable initiator and I_S is the local intensity of the illuminating source. Many existing models (e.g. (*52*)) combine the photolysis reaction and primary initiation reaction (described next) into one rate equation. This is often done through the inclusion of a scalar factor which describes the ratio of primary initiation events to photolysis events (e.g. (*53*)). Because this model seeks to describe a spatially varying polymerization and thus mass transport of reactive species, these two reactions are considered separately.

2.2.2 Propagation

Following photolysis, the next important reaction in the photopolymerization process is initiation of the "primary" or "chain-initiating" radical, depicted in Figure 2-3B. This involves a reaction between an initiator radical (I_r) molecule and an unreacted functional group on a prepolymer chain (P_0) and forms a reactive polymer end group radical (P_1).

$$I_r + P_0 \xrightarrow{k_I} P_1 \tag{2.6}$$

$$R_I = k_I[P_0][I_r] \tag{2.7}$$

In the current model, the rate parameter k_I is used to encompass the reactivity between the two particular reacting species.

The next reaction type considered in the photopolymerization is the propagation reaction, depicted in Figure 2-4. In this reaction, an unreactive end group (P_0) reacts with a radical end group (P_1) to form a crosslink and grow the network. In addition to forming a crosslink, this reaction also leaves a reactive site (P_1), which allows for further network growth. This reaction is modeled using the mechanism of Equation 2.8 and rate equation 2.9 where k_p becomes an additional parameter which is dependent on the particular reacting species.

$$P_0 + P_1 \xrightarrow{k_p} P_1 + P_2 \tag{2.8}$$

$$R_P = k_P[P_0][P_1] \tag{2.9}$$

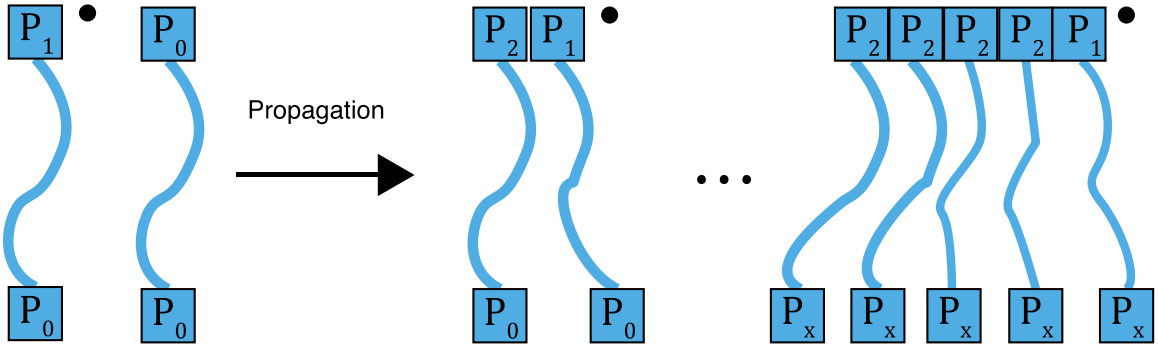

Figure 2-4 Schematic of the propagation reaction. A reactive radical polymer end group $\boldsymbol{P_1}$ reacts with a stable polymer end group $\boldsymbol{P_0}$ to form a crosslink $\boldsymbol{P_2}$ and grow the network.

2.2.3 Termination

The final reaction type in the photopolymerization process is the termination reaction. Termination is used to describe a reaction where one or more end group radicals (P_1) are eliminated but no new radical is generated. The current model considers three distinct types of termination reaction. The first type modeled incorporates chain termination via combination and is depicted in Figure 2-5A. In this case, a pair of P_1 groups react to form a pair of state P_2 groups. The reaction mechanism and rate equation are given in Equations 2.10 and 2.11.

$$P_1 + P_1 \xrightarrow{k_t} P_2 + P_2 \tag{2.10}$$

$$R_t = k_t[P_1][P_1] \tag{2.11}$$

Again, k_t is a parameter that depends on the particular solution composition. It should be noted that a "disproportionation" reaction is also possible, but far less

common and is thus currently not incorporated in the model. In the disproportionation reaction, a pair of P_3 groups would be formed instead.

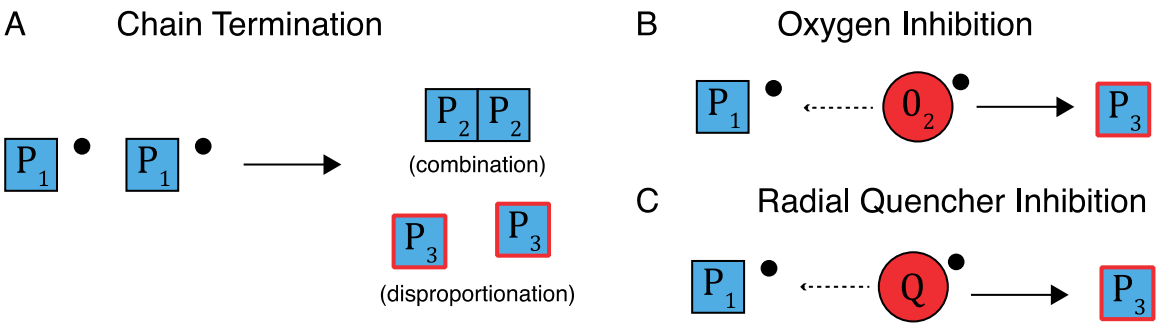

Figure 2-5 Termination and Inhibition reaction schematics. (A) Chain termination. Polymer end group radicals $\boldsymbol{P_1}$ react to end the chain growth process. A combination reaction, where a crosslink is formed, is most likely. Disproportionation, where no crosslink is formed and dead polymer is created, is far less likely. (B) Termination by oxygen inhibition. Oxygen molecules present within the photopolymer formulation react with radical polymer end groups

2.2.4 Inhibition

The second type of termination reaction modeled is a reaction between a radical end group (P_1) and an oxygen molecule (O_2) (Figure 2-5B). This "inhibition" reaction typically results in the formation of a peroxy radical, which is much less reactive than the polymer radical. For modeling purposes, the peroxy radical or any other species formed by this reaction is considered to be a "dead" P_3 polymer end group. As this reaction consumes an oxygen molecule, the oxygen concentration is updated accordingly in the model. Reaction mechanism and rate equation are given in Equations 2.12 and 2.13 respectively.

$$P_1 + O_2 \xrightarrow{k_{tO}} P_3 \tag{2.12}$$

$$R_{tO} = k_{tO}[P_1][O_2] \tag{2.13}$$

It is worth reiterating that the P_3 group generated in this reaction is chemically distinct from the one formed in the disproportionation reaction but is considered equivalent for the purpose of modeling because a polymer end group has reacted but formed no bond and will form no bond with another polymer molecule.

The third type of termination reaction modeled involves the reaction of a P_1 group with an added inhibitor or "quencher" molecule Q (Figure 2-5C). This again forms a "dead" end group P_3.

$$P_1 + Q \xrightarrow{k_{ti}} P_3 \tag{2.14}$$

$$R_{ti} = k_{ti}[P_1][Q] \tag{2.15}$$

2.2.5 Diffusion

In addition to reactions between species that result in pointwise changes in concentration, species are also free to diffuse throughout the medium. The model considers diffusion of the small molecules only (initiator and inhibitor molecules) and considers the prepolymer molecules immobile because the polymer chains are much larger and become decreasingly mobile as they form cross-links. Species diffusion is modeled using Fick's Second law (*54*) with isotropic diffusivity. The expression used for the rate of change in concentration of a given species $[X]$ due to diffusion is

$$\frac{\partial [X](x,y,z)}{\partial t} = D_X \cdot \nabla^2 [X](x,y,z) \tag{2.16}$$

where D_X is the diffusivity of the species in the particular solution. This is also expressed as

$$\frac{\partial [X]}{\partial t} = D_X \cdot \left(\frac{\partial^2 [X]}{\partial x^2} + \frac{\partial^2 [X]}{\partial y^2} + \frac{\partial^2 [X]}{\partial z^2} \right) \tag{2.17}$$

Diffusivity values are estimated using the Stokes-Einstein Relation for a spherical molecule in Stokes flow (*55*),

$$D = \frac{k_B T}{6\pi \mu r_h} \tag{2.18}$$

where k_B is the Boltzmann constant, T is temperature, μ is the viscosity of the solution, and r_h is the hydrodynamic radius of the diffusing species. The hydrodynamic radius of oxygen has been previously calculated as $r_{O_2} = 2.16$Å (*56*). For the hydrogel materials presented in Section 2.4, the viscosity μ of the solution was taken to be the weighted average of the viscosity of water μ_{H_2O} and the viscosity of the polymer PEGDA μ_{PEG}.

$$\mu = \frac{m_{H_2O}}{m_{sol}} \mu_{H_2O} + \frac{m_{PEG}}{m_{sol}} \mu_{PEG} \tag{2.19}$$

2.3 Rate Equations

Following the model described in the Section 2.2, the coupled Reaction-Diffusion equations of the eight species in solution become

$$\frac{d[I]}{dt} = -\frac{\phi \epsilon}{N_A h \nu} [I] \cdot I_s + D_I \cdot \left(\frac{\partial^2 [I]}{\partial x^2} + \frac{\partial^2 [I]}{\partial y^2} + \frac{\partial^2 [I]}{\partial z^2} \right) \tag{2.20}$$

$$\frac{d[I_r]}{dt} = 2 \cdot \frac{\phi\epsilon}{N_A h\nu}[I] \cdot I_s + D_{Ir} \cdot \left(\frac{\partial^2[I_r]}{\partial x^2} + \frac{\partial^2[I_r]}{\partial y^2} + \frac{\partial^2[I_r]}{\partial z^2}\right) \tag{2.21}$$

$$\frac{d[P_0]}{dt} = -k_I[P_0][I_r] - k_p[P_0][P_1] \tag{2.22}$$

$$\frac{d[P_1]}{dt} = k_I[P_0][I_r] - k_t[P_1]^2 + k_{t2}[P_1][T_r] - k_{tO}[P_1][O_2] \tag{2.23}$$

$$\frac{d[P_2]}{dt} = k_p[P_1][P_0] + k_t[P_1]^2 \tag{2.24}$$

$$\frac{d[P_3]}{dt} = k_{t2}[P_1][T_r] + k_{tO}[P_1][O_2] \tag{2.25}$$

$$\frac{d[O_2]}{dt} = -k_{tO}[P_1][O_2] + D_{O_2} \cdot \left(\frac{\partial^2[O_2]}{\partial x^2} + \frac{\partial^2[O_2]}{\partial y^2} + \frac{\partial^2[O_2]}{\partial z^2}\right) \tag{2.26}$$

$$\frac{d[T_r]}{dt} = -k_{t2}[P_1][T_r] \tag{2.27}$$

These equations govern the local concentrations of all species at all points within the domain at all times during the photopolymerization process. In order to solve these equations the domain is first discretized in three dimensions. The reaction terms are computed point-wise. The second derivative diffusion terms are calculated by a finite difference approximation described in Section 2.3.1. Integration of the time derivative is computed using an explicit Forward Euler time stepping method using the relation given in Equation 2.28.

$$[X](t + \Delta t) = [X](t) + \Delta t \cdot \frac{d[X]}{dt}(t) \tag{2.28}$$

2.3.1 Finite Difference Solver

The finite difference solver used is based on a central difference approximation (shown for Δx in Equation 2.29. Relations for y and z follow similarly)

$$D_X \frac{\partial[X]}{\partial x} \approx D_X(x) \frac{[X]\left(x + \frac{\Delta x}{2}, y, z\right) - [X]\left(x - \frac{\Delta x}{2}, y, z\right)}{\Delta x} \tag{2.29}$$

Taking D as a constant and applying the central difference approximation again for the second derivative we get

$$\frac{\partial}{\partial x}\left(\underbrace{D_X \frac{\partial[X]}{\partial x}}_{F_x}\right) \approx \frac{F_x\left(x + \frac{\Delta x}{2}, y, z\right) - F_x\left(x - \frac{\Delta x}{2}, y, z\right)}{\Delta x} \tag{2.30}$$

By combining Equations 2.29 and 2.30, assuming isotropic diffusivity, and proceeding similarly in y and z we arrive at the finite difference approximation for the diffusion term: Equation 2.31.

$$\begin{aligned} & D_X \cdot \nabla^2[X](x,y,z) \\ & = D_X \left(\frac{[X](x+\Delta x) + 2[X](x) + [X](x-\Delta x)}{\Delta x^2} \right. \\ & + \frac{[X](y+\Delta y) + 2[X](y) + [X](y-\Delta y)}{\Delta y^2} \\ & \left. + \frac{[X](z+\Delta z) + 2[X](z) + [X](z-\Delta z)}{\Delta z^2} \right) \end{aligned} \tag{2.31}$$

In the simulations presented in this chapter, a periodic boundary condition is used at the edges of the domain in x and y. This is done because the design of the shadow mask described in Section 3.3 is periodic in x and y. The experimental calibration of the model uses a two-dimensional simulation, thus z is not considered and no boundary condition is necessary.

2.4 Materials

The model presented can be applied in the general case of patterned photopolymerization provided that the appropriate numerical values for model parameters are input. In the present chapter, this model was used to model observations from experiments using Poly(ethylene-glycol) Diacrylate at $M_n = 700\ Da$ with photoinitator Irgacure 2959 mixed as a hydrogel in $\sim$70% water. The same modeling framework can be used to model the behavior of the acrylate materials used in Chapters 3 and 4. The PEGDA molecule contains a poly(ethylene-glycol) (PEG) backbone with 2 acrylate groups on each chain as depicted in Figure 2-6. The acrylate groups are considered to act independently in the model. That is, the state of the acrylate group on one end of the chain is not affected by the state of the group on the other end. The Irgacure 2959 molecule is shown in Figure 2-7. In the model, the stable initiator molecule is considered to cleave into two equivalent species. This is an approximation as, in reality, the molecule cleaves into two distinct species as shown in Figure 2-7B.

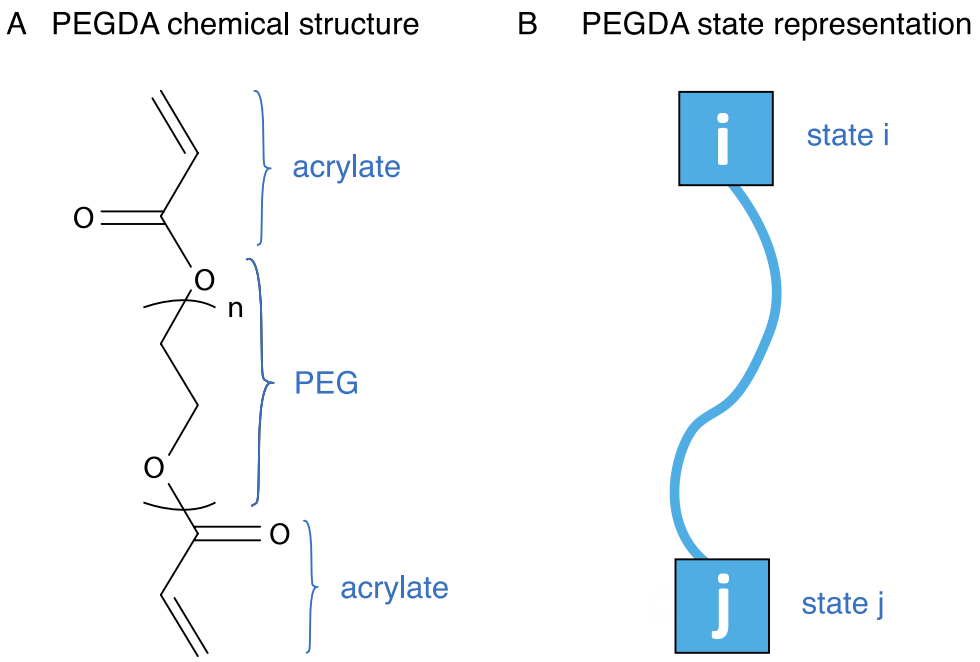

Figure 2-6 (A) Molecular structure of PEDGA, the polymer molecule used for experimental validation of the photopolymer kinetics model. (B) The corresponding state representation of the PEGDA molecule as used in the model.

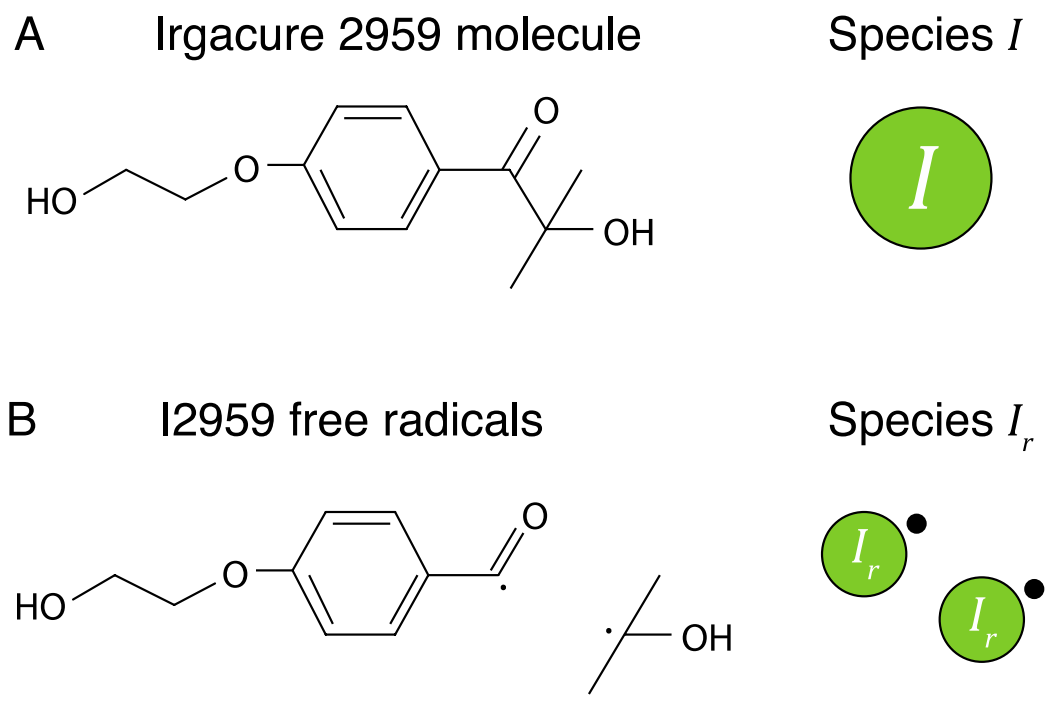

Figure 2-7 (A) Chemical structure of Irgacure 2959, the photoinitiator molecule used in model validation. **(B)** Chemical structure of I2959 cleaved radical species. Species nomenclature given for both.

2.5 Experimental Calibration

An experimental apparatus was developed to calibrate and validate simulation predictions. This apparatus is shown in Figure 2-8. Thin hydrogel samples were contained between glass microscope slides with thickness controlled by a spacer placed at the edges of the slides. For most trials, a single or multiple stacked glass coverslips with thickness 170 μm each were used as spacers. Scotch tape with thickness 62.5 μm (as listed by the manufacturer) was also used alone or in combination with cover slips to set the desired thicknesses. A shadow mask was placed in contact with the bottom slide to modulate light in the pattern desired in the gel. The mask was printed with black ink on one side of a transparency. The layout of the mask is described in Section 2.5.1 and shown in Figure 2-9. The solution was illuminated with a UV LED source (Thorlabs M365LP1) at 365 nm central wavelength. Exposure time was controlled by a switchable optical beam shutter (Thorlabs SH1). The intensity of the source was set at 100 $mWcm^2$ unless otherwise noted.

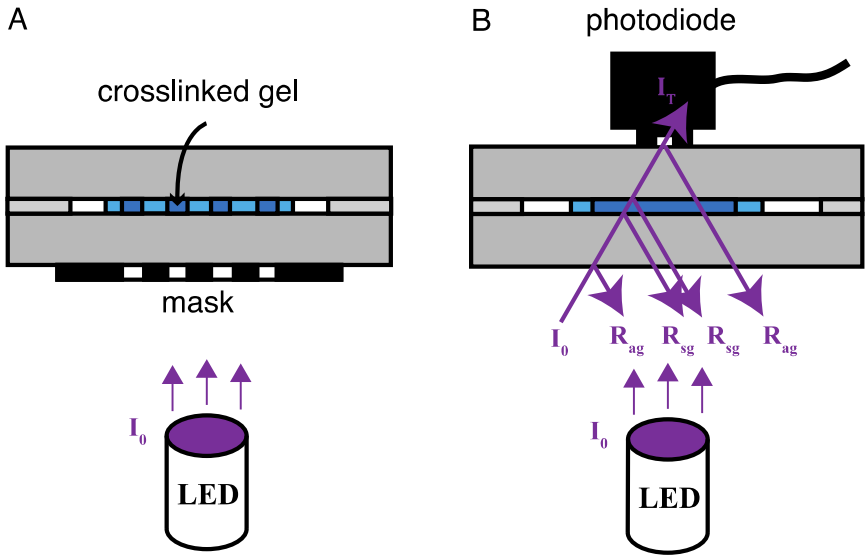

Figure 2-8 (A) Apparatus used for experimental validation. Solution was pipetted onto bottom glass microscope slide to form a droplet. Spacers were placed on the edges of the slide. The top slide was gently placed to even the height of the droplet and set the thickness of the sample. (B) Hydrogel transmission calibration setup showing interfaces where a step change in refractive index leads to reflection (used in Section 2.5.2).

2.5.1 Calibration Mask

A single period of the shadow mask pattern was used to experimentally validate the model is shown in Figure 2-9. The mask was designed to examine the effect of pattern density on the formation of cross-linked features. Pattern density is defined as the ratio of transparent area to opaque area in a given region of the mask.

The mask design consists of four columns of varying pattern density (~0%, ~20%, ~40%, ~80%). The ~0% column contains isolated square features with side lengths of 30 μm, 50 μm, and 100 μm. A feature with each of these side lengths is embedded in each column of varying pattern density. The mask is periodic in both directions and contains the same pattern replicated on all sides.

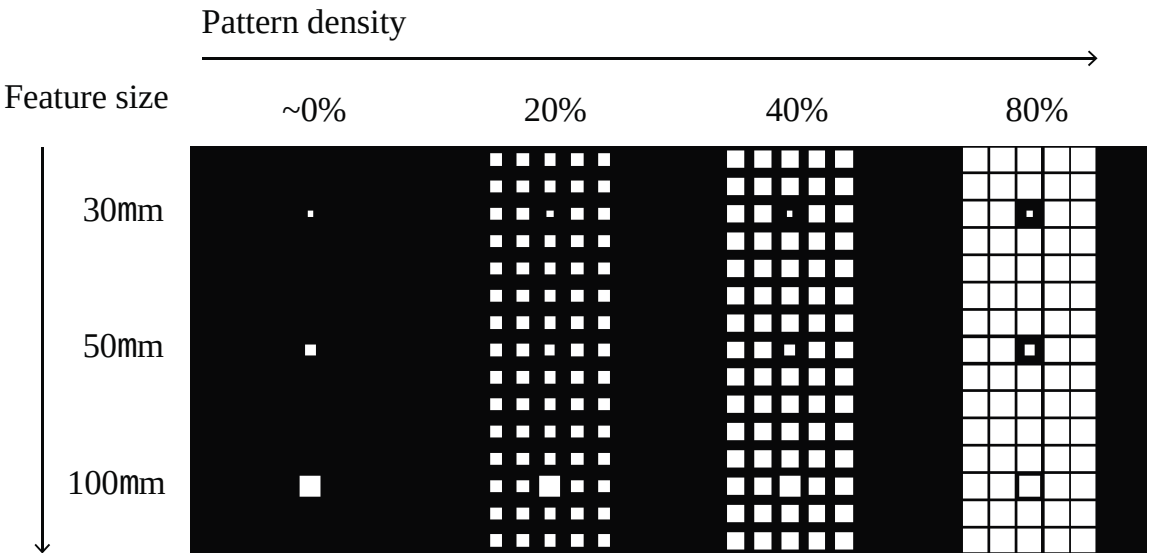

Figure 2-9 Layout of the mask used for model calibration. Features of side length 30 μm, 50 μm, and 100 μm are immersed in columns with pattern densities of 0%, 20%, 40%, and 80%.

2.5.2 Transmission Model

Determination of the degree of crosslinking as a function of position is a challenging process that makes direct experimental validation difficult. For acrylate polymers, spectroscopic techniques can potentially be used to measure carbon-carbon double bond concentrations. This bond is cleaved as the polymer crosslinks. In this work, in order to compare the degree of cure predicted by the model to that observed experimentally, a theoretical analysis of optical transmission was performed. The conversion ratio C, in this case the ratio of the concentration of acrylate–acrylate bonds to the initial concentration of unconverted acrylate groups, can be computed from the model as given in Equation 2.32.

$$C(x,y,z) = \frac{[P_2](x,y,z)}{[P_0]_{t=0}} \tag{2.32}$$

The model assumes that the refractive index of the material varies linearly with the conversion ratio (*41*). Using this relationship, the analysis considers transmissions and reflections at interfaces of changing refractive index between the air, the glass microscope slides, and the curing solution as shown in Figure 2-8B. Transmission coefficients are computed using the Fresnel Equation 2.33 (*57*). The analysis also

considers optical absorption according to the Beer–Lambert exponential law (Equation 2.34).

$$T = 1 - R = 1 - \left(\frac{n_2 - n_1}{n_2 + n_1}\right)^2 \tag{2.33}$$

$$I(z) = I_0 e^{-z/D_p} \tag{2.34}$$

The penetration depth D_P and refractive index of the solution were calibrated by measuring transmission through a bulk curing solution with no mask as illustrated in Figure 2-8B. These values both depend on the conversion ratio. The thickness of the curing solution was varied in order to provide a data set for fitting. The expression for the transmitted intensity I_T in terms of source intensity I_0 becomes Equation 2.35. Both the transmission coefficient T_{sg} and the penetration depth depend on the local conversion ratio.

$$I_T(x, y) = I_0 T_{ag}^2 T_{sg}^2(x, y) e^{-z/D_p} \tag{2.35}$$

Using Equation 2.35, the model was adapted to output the simulated transmitted intensity through the cured sample. These simulations were compared to transmissive white light bright-field microscope images. An example of this comparison at a range of exposure times is shown in Figure 2-10. Regions of higher conversion appear darker.

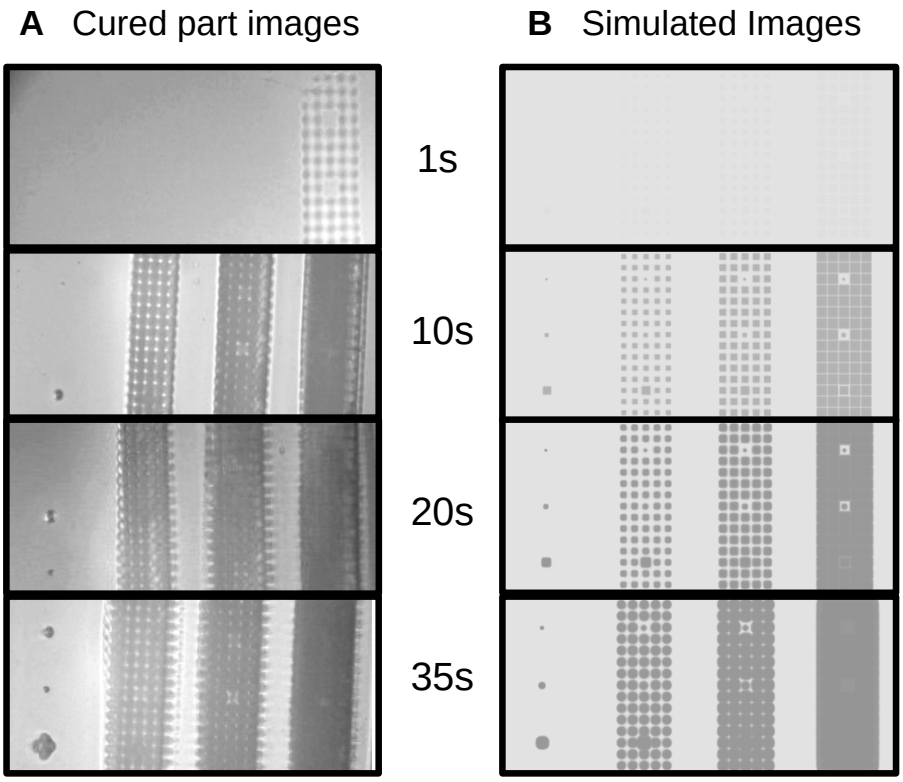

Figure 2-10 Experimentally observed polymerization vs. simulated polymerization for a hydrogel solution of 30% w/v PEGDA and 3% w/v I2959 in PBS buffer. Exposure times are listed on the left. Intensity is 100 mW/cm^2.

2.5.3 Effects of Pattern Density

The model is able to capture observed geometric trends from experiments. In Figure 2-10 we see that the regions of high pattern density form more quickly. The column of 80% density forms first, followed by the three other columns in order of decreasing pattern density. We also observe this phenomenon in the row of isolated features as the largest (100 μm) feature is the first to form. This effect can be explained through radical inhibition. Because of the high reactivity of oxygen with radicals (both initiator I_r and polymer P_1) there is an inhibition period where almost no polymerization occurs. This period lasts until almost all of the inhibitor molecules in a given area have been consumed by radicals. Once the inhibitor molecules have been consumed, the propagation reaction becomes dominant and covalent bonds between polymer chains are quickly formed. In areas of low areal density of illumination, inhibitor molecules from the surrounding unexposed area quickly diffuse into the illuminated area while radicals diffuse out. This increases the necessary exposure dose to overcome inhibition and increases the duration of the inhibition period in those regions. After a given feature has formed to meet the geometry of its illuminated area, it begins to blur and expand to the surrounding area. Features become more blurred (covering a larger area than that defined on the mask) when using the hydrogel with PBS buffer compared to if a pure polymer with

no buffer, such as the pure PEGDA shown in Figure 2-11, is used. This effect can be observed by comparison of Figure 2-10 to Figure 2-11. It can be explained through diffusion of radicals to areas outside where the radicals were generated. This effect is more pronounced in the lower viscosity hydrogels compared to the pure polymer as predicted by lower diffusivities according to the Stokes-Einstein relation (Equation 2.18).

For any given feature in the mask, at a fixed solution composition and intensity, it appears that there exists an optimal exposure time which will cure the feature to its desired geometry. However, this optimal exposure time varies between features as a function of the local pattern density. Considering the hydrogel for example (Figure 2-10A), when features in the 80% dense column have reached their optimal exposure time, features in the 20% dense column often are still in the inhibition period. When the isolated features in the ~0% dense column reach their optimal exposure dose, features in the 80% dense column have blended together. Again, this effect is more pronounced in the hydrogel compared to the pure polymer.

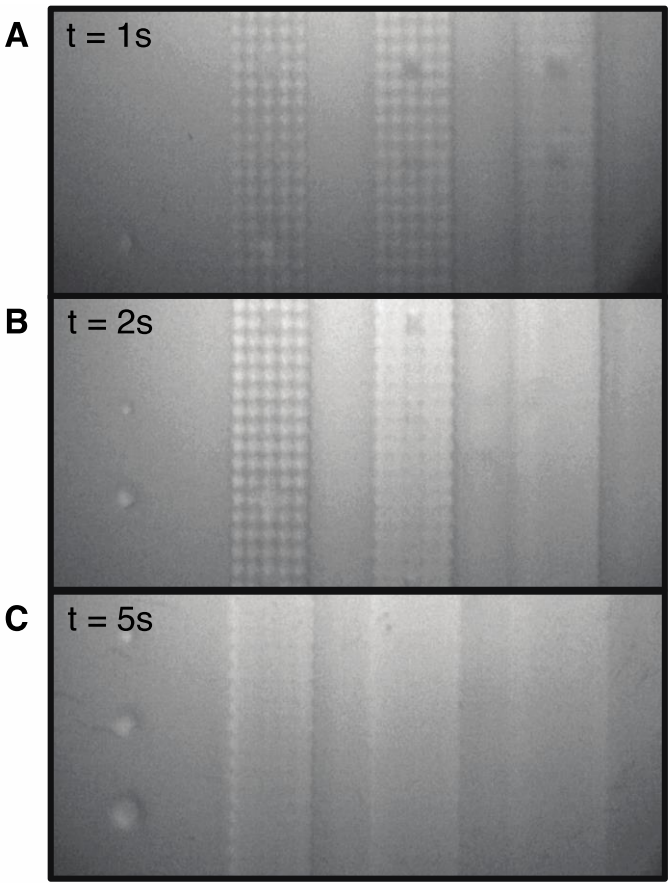

Figure 2-11 Images of cured non-hydrogel resin using a pure polymer (97% w/v PEGDA) with 3% w/v I2959 at an intensity of 100 mW/cm^2. Note these images were taken using a reflective imaging system and thus bright regions correspond to higher degrees of conversion.

We believe the dominant effect causing blurring to be diffusion of radicals from illuminated regions to regions surrounding illuminated features. While it is possible that there is some optical spreading of the illumination in the current setup, this is accounted for by modeling of propagation through 1 mm of glass. This is accomplished using a Fresnel propagation model for near-field diffraction (*58*). Thus, diffraction is simulated by convolving the complex electric field at the transparency mask with a point-spread function $h(x, y, z)$ (given in Equation 2.36): a quadratic approximation to a spherical wave emanating from a point source:

$$h(x, y, z) = \frac{n * e^{2\pi n z/\lambda}}{i\lambda z} e^{i 2\pi n/\lambda (x^2 + y^2)} \tag{2.36}$$

In this case λ is the free-space wavelength of the source (365 nm for the experiments included) and n is the refractive index of the propagation medium (~1.55 for a glass microscope slide).

The effect of pattern density on the ability to generate fine (10-100μm) features in PEGDA hydrogel materials is clear. Going forward, in order to pattern geometries with varying degree of pattern density in these materials, it may be necessary to perform a form of proximity correction (*59*) on the target geometry. This is done frequently in semiconductor lithography and existing algorithms could potentially be leveraged and applied to hydrogel patterning. Additionally, when using photopolymer precursor materials with higher viscosity in the liquid form, diffusivities of all species can be reduced according the Stokes-Einstein relation of Equation 2.18. This is done in Chapter 4 when a photopolymer precursor material of viscosity 5000cP is utilized.

Chapter 3 Multi-Beam Volumetric Printing

The previous chapter has presented a framework for modeling photopolymer kinetics in response to incident optical illumination as occurs in a number of existing AM processes. With a photopolymer kinetics model developed and tested, the next phase of this thesis presents the design and implementation of a manufacturing system to produce 3D parts volumetrically. This section focuses on design and delivery of optical light fields to a photopolymer volume, which may follow the kinetics described in the previous chapter. To address this challenge of generating and delivering patterned 3D intensity fields, an optical system was designed and built initially to generate 3D intensity fields from a coherent laser source and spatial control of its phase. Credit to Maxim Shusteff from LLNL for the initial construction of the system shown in **Figure 3-1**. The premise behind construction of this system was to develop a means for generating controlled 3D intensity distributions within a photopolymer volume to cure a 3D part. This approach follows from a technique which achieved serial patterning of 3D structures using holographically-controlled fields (*60*–*62*). The goal was to leverage similar hardware and devise a method to generate custom 3D intensity fields within the volume. The phase control approach is described in Section 3.4. A second approach leveraging intensity superposition from similar system hardware is described in Section 3.5 and Section 3.6.

3.1 System Configuration

The design of a holographic patterning system centered on the use of a laser illumination source and spatial control of the phase of the laser illumination. In particular, the holographic light patterning system utilized a 532 nm continuous wave (CW) laser (Verdi V6, Coherent, USA. Max Power = 6 W), and a phase-only liquid crystal on silicon (LCOS) spatial light modulator (SLM) (*63*) (obtained from Holoeye GmbH, Germany). The initial system schematic is shown in Figure 3-1. In this system, the laser source is expanded and spatially filtered and sent through a set of 4f image relaying systems. Each 4f system consists of a set of two lenses separated by the sum of twice the focal length of each lens and serves to magnify the size of the image by the ratio of the focal lengths of the two lenses. A 2f Fourier Transform lens system relays the patterned phase image to the target plane. These systems are further described in sections 3.1.1 and 3.1.2.

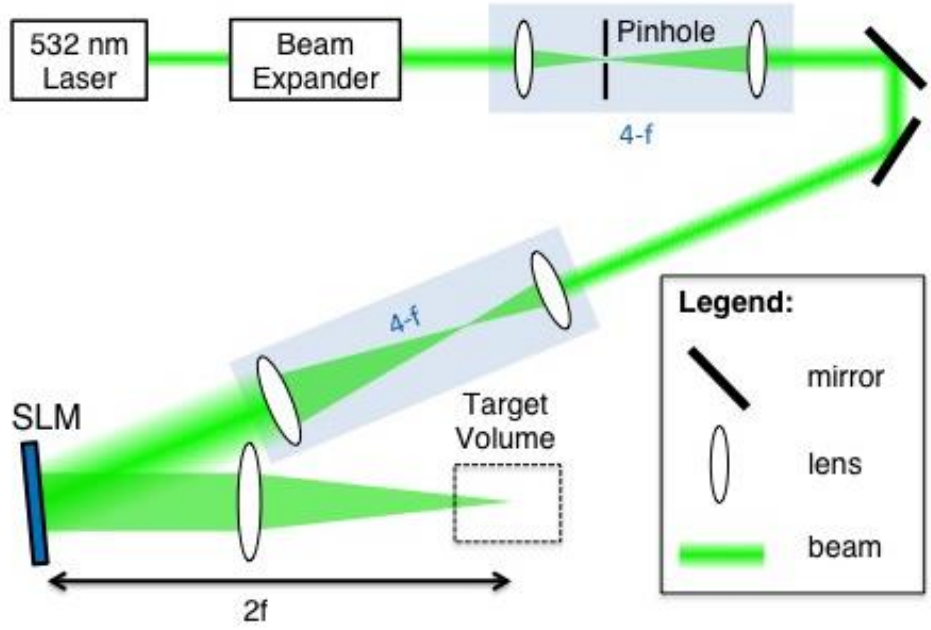

Figure 3-1 Holographic lithography initial system layout. A 532 nm wavelength laser beam is conditioned and impinges upon a phase-only spatial light modulator (SLM). The SLM is coded to deliver a 3D intensity field to the target volume as described in Section 3.2.

3.1.1 2F Fourier Transform Lens

The 2f lens system used between the SLM and the photopolymer target volume performs a Fourier Transform of the optical field at the SLM. To understand the Fourier transforming property of the 2f system we can start from the equation for a thin lens phase transformation (*64*) given in terms of spatial coordinates x and y and the lens focal length f in Equation 3.1:

$$t_l(x,y) = exp\left[-j\frac{k}{2f}(x^2+y^2)\right] \tag{3.1}$$

Here t_l represents the transmission function of the lens and $k = 2\pi/\lambda$ is the wavenumber, describing the photon energy and wavelength of the incident illumination. The parameter λ is the optical wavelength. The spatial coordinates x and y describe the plane normal to the incident image direction and focusing direction z. The effect of a lens in a 2f system can be derived by first considering an input field $g(x,y)$ at a distance z in front of the lens (*65*). Then, by applying a free space propagation kernel for a distance z, applying a lens transformation according to Equation 3.1, and finally applying a second propagation computation the field at the image plane can be computed. Following the coordinate system convention adopted in Figure 3-2, the resulting field at the image plane $g_f(x'',y'')$ is given as:

$$g_f(x'',y'') = exp\left[i\pi\frac{x''^2+y''^2}{\lambda f}\left(1-\frac{z}{f}\right)\right]G\left(\frac{x''}{\lambda f},\frac{y''}{\lambda f}\right) \tag{3.2}$$

where the function G is the 2D Fourier transform of the function g. The field at the image (x'', y'') plane of the system appears as a scaled version of the Fourier Transform of the field at the object (x, y) plane. When the object is placed at a distance $z = f$ from the lens as in the 2f system of Figure 3-1 and schematic Figure 3-2, the output of the 2f system is the exact Fourier transform of the input field where the spatial frequencies of g appear at the image plane at locations dictated by the spatial coordinates x'' and y''.

$$g_f(x'', y'') = G(u, v) = G\left(\frac{x''}{\lambda f}, \frac{y''}{\lambda f}\right) \tag{3.3}$$

The spatial frequencies u and v of the input field function g at the object plane appear at locations $x''/\lambda f$ and $y''/\lambda f$ at the image plane. The holographic hardware system implementation depicted in Figure 3-1 utilizes such a $2f$ lens system to deliver computed images from the SLM to the target plane/volume. This process is described in further detail in Section 3.2.

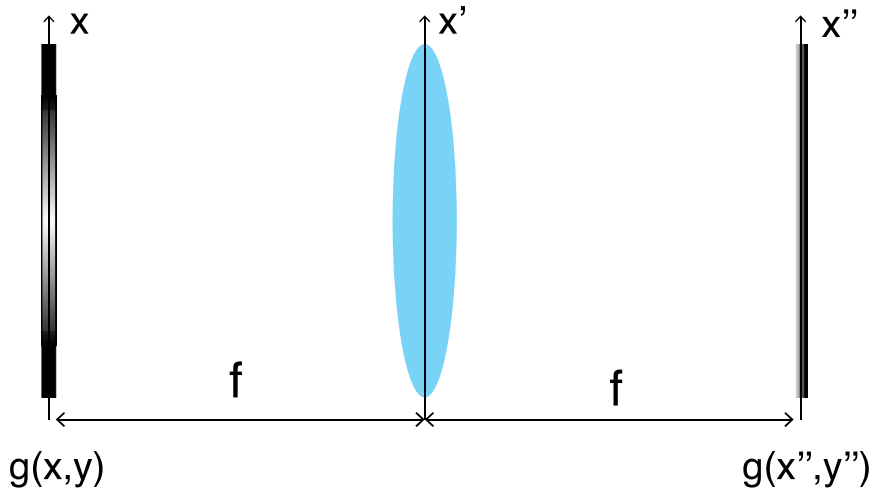

Figure 3-2 A 2f lens system schematic showing coordinate system conventions described in Section 3.1.1. *x* and *y* describe the lateral coordinates orthogonal to the lens at the image plane while (x',y') and (x'',y'') respectively describe lateral coordinates at the lens and image planes. z is the beam propagation direction, along the focal direction of the lens.

3.1.2 4f Imaging System

The 4f systems used in the holographic light patterning system (Figure 3-1) represent a cascade of a pair of 2f lens systems, with each lens having a different focal length, denoted here as f_1 for the first lens in the beam path and f_2 for the second. As described in Section 3.1.1, the first lens in the 4f system will perform a

Fourier transforming operation on the object plane field as in Equation 3.3. The field $g''(x'', y'')$ at the central, or Fourier plane, of the 4f system becomes the Fourier transform of the object plane field $g(x, y)$:

$$g''(x'', y'') = G(u, v) = G\left(\frac{x''}{\lambda f_1}, \frac{y''}{\lambda f_1}\right) \tag{3.4}$$

where again u and v are the spatial frequencies of x and y respectively. The second lens of the 4f system acts as an additional 2f system and performs a Fourier Transforming operation on the field at the (x'', y'') plane. In this operation, the spatial frequencies of g'' appear scaled by the focal length of the second lens f_2. The application of the second Fourier transform operation gives the field at the image plane which follows the relation given in Equation 3.5:

$$g'(x', y') = G(u'', v'') \tag{3.5}$$

Here the quantities u'' and v'' represent the spatial frequencies of the field g'' at the Fourier plane of the 4f system. The function g' describing the field at the image plane of the 4f system becomes:

$$g'(x', y') = g\left(-\frac{f_2}{f_1}x, -\frac{f_2}{f_1}y\right) \tag{3.6}$$

The relation of Equation 3.6 shows that the output of the 4f system—the image plane field g'—appears as a scaled version of the input—the object plane field g.

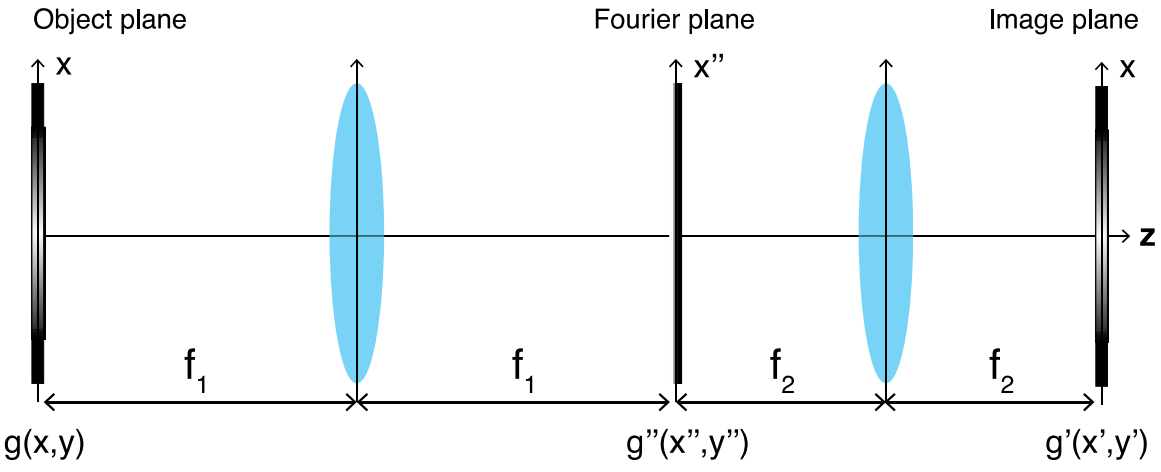

Figure 3-3 A schematic of a two-lens, 4f system which performs a magnifying operation on the object plane field.

The 4f system performs a magnification operation on the incident field at the image plane with at magnification factor M of

$$M = \frac{f_2}{f_1} \tag{3.7}$$

3.2 Holographic Image Computation

In this Section, we describe the calculation and generation of holographic images for patterning of 3D volumes. These images are generated through modulation of the incident laser illumination by the SLM. The Holoeye SLM (PLUTO-VIS) used in this thesis modulates the phase of the incident laser illumination pixel-by-pixel in a 1080 × 1920 (HD) array of square pixels of size 8 μm × 8 μm. Each pixel delays the phase of the incident laser illumination locally with a delay programmable between 0 and 2π radians over 8-bit (256 levels) grayscale values. The encoded SLM image is then delivered to the target volume through a 2f lens system (described in Section 3.1.1). The lens is placed at one focal distance from the SLM while the target volume is positioned at one focal length's distance on the opposite side so as to impose a 2D Fourier transform between the SLM and target plane.

3.2.1 2D Gerchberg-Saxton Algorithm

The phase pattern encoded onto the SLM is derived from the target image intensity. The computation performed to generate the phase map on the SLM utilizes the iterative Gerchberg-Saxton (G-S) algorithm. This algorithm follows an iterative propagation and back-propagation via the Fourier Transform while imposing constraints of constant phase at the SLM plane and target amplitude distribution at the image plane. The algorithm is described in detail in (*66*).

3.2.2 Image Positioning

By leveraging the 2D Gerchberg-Saxton algorithm, we demonstrate the ability to produce a ***two***-dimensional image at the focal plane of the image relaying system. The task to perform single-shot 3D lithography, however, requires generation of a ***three***-dimensional intensity distribution to be sent to the resin volume. As discussed in Chapter 1, the vast majority of serial vat photopolymerization technologies build up parts either point-by-point or layer-by-layer. In either case, the first step in the printing process is to slice the digital 3D model into a set of parallel 2D slices. In layer-at-once fabrication techniques, each 2D slice is printed in a single step. In the point-at-once case, the 2D slice is traced point-by-point before printing the next layer. In this work, we first attempt to apply this slicing concept to volumetric (volume-at-once) fabrication. A volume-at-once fabrication technique should print multiple slices, or ideally all slices, in a single step. To achieve this by holographic light patterning and photopolymerization then requires generation of patterned optical images for multiple slices simultaneously. One route to address this requirement is to simultaneously generate a series of patterned 2D images at multiple locations in space. In this work, this was carried out

by using the Gerchberg-Saxton image generation algorithm to produce a set of 2D images focused to different parallel planes in the propagation direction. As discussed, the presented G-S algorithm is used to produce a single 2D image focused at a single plane only. Generation of images in additional locations requires repositioning. In this work, the repositioning of additional images is performed computationally through addition of computed phase profiles to the SLM.

One necessary positional shift to the generated image involves a shift in the optical propagation direction or a shift in the focal distance from the SLM plane. In order to shift the focal plane of a particular 2D slice image, a phase function was added to the computed-generated hologram (CGH) programmed onto the SLM. This was achieved by adding a spherical lens phase pattern to each computed CGH. The lens phase can be computed as

$$\phi_s = 2\pi \frac{\Delta f}{\lambda(f - \Delta f)^2} r^2 \tag{3.8}$$

Where f is the focal length of the Fourier Transform lens in the physical $2f$ system, Δf is the z distance between the modified focal plane and the focal plane of the Fourier Transform lens, λ is the illumination wavelength, and r is the distance from the center of the SLM. To compute the spherical lens phase shift for a particular pixel on the SLM, $\Delta\phi_{s\,i,j}$, Equation 3.8 becomes

$$\Delta\phi_{s\,i,j} = 2\pi \frac{\Delta f}{\lambda(f - \Delta f)^2} \left(x_i\delta + y_j\delta\right)^2 \tag{3.9}$$

Where δ is the spatial pixel size and x_i, y_i are the number of pixels from the center in the horizontal and vertical directions respectively for pixel $p_{i,j}$. By adding a lens phase to the CGH, the focused image was translated in space by a distance Δf.

It is also possible to add a linear phase that shifts the location of the focused image laterally (in x and y). Adding a linear phase can aid in shifting the image away from high power diffraction orders as described in Section 3.3. Linear phases were computed from (*67*) as given in Equation 3.10 where the parameter β is defined by Equation 3.11.

$$\phi_l = (x \sin\beta + y \cos\beta) \tan\theta \tag{3.10}$$

$$\beta = \sin^{-1}\left(\frac{x}{\sqrt{x^2 + y^2}}\right) \tag{3.11}$$

In Equations 3.10 and 3.11, x represents the lateral dimension of the image shift. A second shift can be applied in the y direction to fully position the image in the lateral plane. The angle θ gives the angular shift from the Fourier lens and the total image shift Δl in the single lateral dimension x becomes

$$\Delta l = f \tan\theta \tag{3.12}$$

The pixel-by-pixel phase shift value $\phi_{l\,i,j}$ was then computed in terms of the desired lateral shift Δl and the focal length of the Fourier lens f as

$$\phi_{l\,i,j} = \left(\frac{{x_i}^2}{\sqrt{{x_i}^2 + {y_j}^2}} + y_j \cos\beta \right) \frac{\Delta l}{f} \tag{3.13}$$

To generate the optical pattern for a single slice of a 3D geometry, we start by computing a CGH from the Gerchberg-Saxton algorithm to define the patterned 2D image. Printing of a single slices requires generation and positioning of the target image. To generate this intensity profile, a diffractive optical element (DOE) was constructed. Each DOE consisted of a phase map containing information for 1) generating a 2D image, 2) positioning it axially (in the optical propagation z direction), and 3) positioning it laterally in the (x, y) plane. This was carried out by summation of 3 phase profiles, respectively 1) the CGH, 2) a computed lens phase profile, and 3) a linear phase profile, potentially containing both x and y components. This summation is illustrated in Figure 3-4.

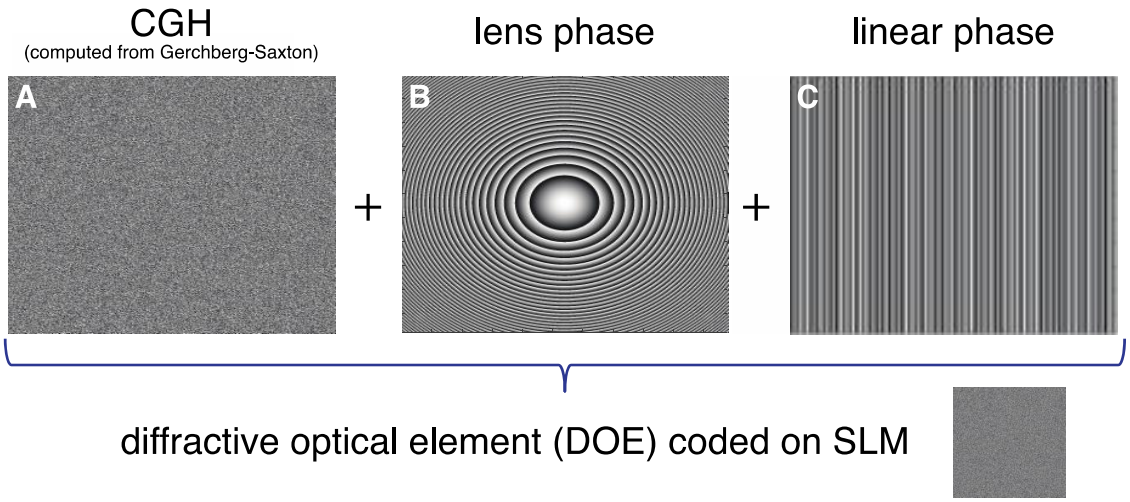

Figure 3-4 A diffractive optical element (DOE) which creates a 2D image and positions it in 3D space is computed by (A) generating a CGH via the Gerchberg-Saxton algorithm, (B) adding a lens phase to shift the image spatially in *z*, and (C) adding linear phases to shift the image in *x* and *y*.

3.3 Zero-Order Mode Elimination

The use of LCOS SLM phase control of images does bring one prominent drawback, which arises from the effect of undiffracted light contributing energy to the zero order mode. This results in an undesired bright intensity spike in the center of the target plane image. In early testing of the holographic light patterning system of Figure 3-1, the prominence of this effect was readily observed. An example is given in Figure 3-5A. In this image, a paper card is placed at the target plane and the

intensity pattern at that plane reflects off the card and is imaged with a camera. Here we clearly see visible the features of the Lawrence Livermore National Lab logo and also the presence of the additional high power bright spot in the center. The power present in the zero order mode was measured to be a large percentage (between ~50-70% depending on the geometry of the target image) of the laser power incident on the SLM. When applying the system to curing of photopolymers, such misdistributed power will lead to undesired curing.

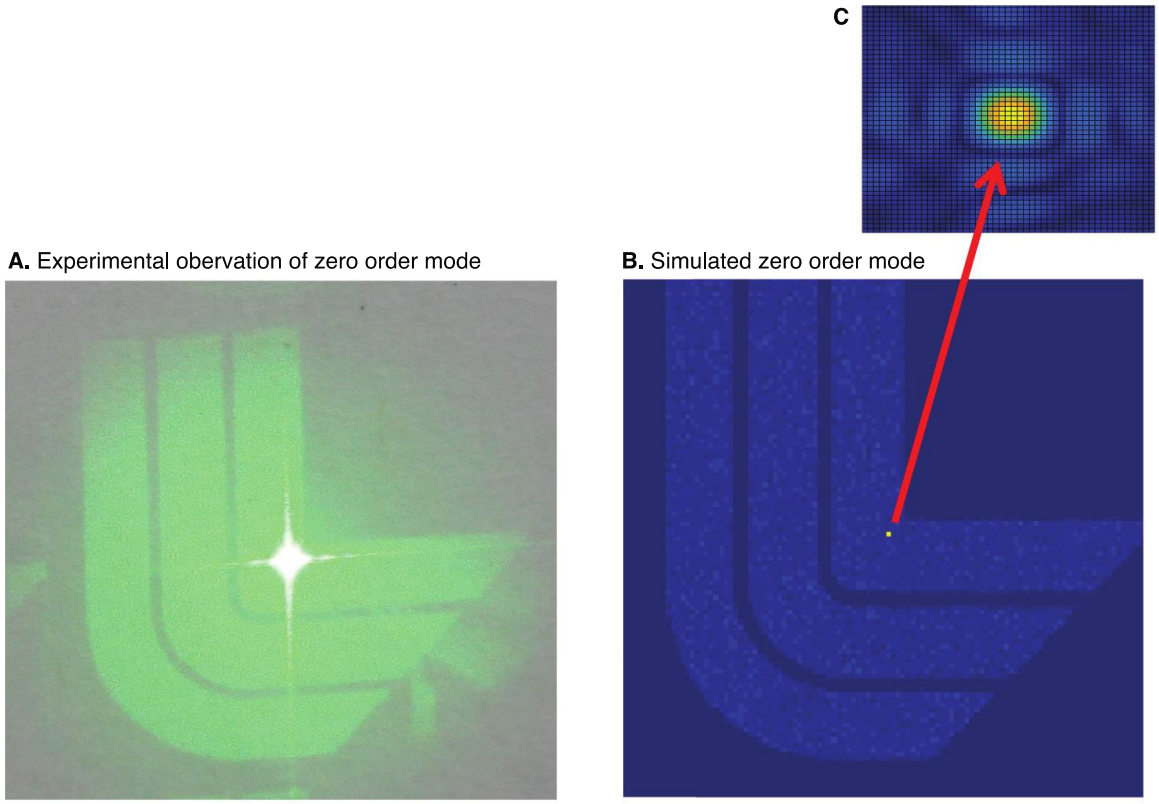

Figure 3-5 (A) Observed undesired zero order mode bright spot in the center of the target plane image. (B) A simulation of cross talk between SLM pixels captures this effect. (C) A zoomed in view of the simulated zero order mode contribution.

This is a well-documented phenomenon that can be understood from a simple model of the SLM surface. Figure 3-6 shows a schematic for the model used to capture this effect. In this model, two effects contribute to the appearance of the zero order mode. First, a small fraction (~0.5%) of the incident light on the SLM surface is considered to reflect directly, before passing through the liquid crystal and receiving phase modulation. The parameter A_r captures this fraction and an intensity profile of constant phase with intensity $I = A_r * I_0$ reflects directly off the SLM. Additionally, an SLM pixel fill factor of less than unity is considered along with a transition region of phase between adjacent pixels. In the simulated image shown in Figure 3-5B and C a linear interpolation is considered for the phase in the "dead space" region between pixels.

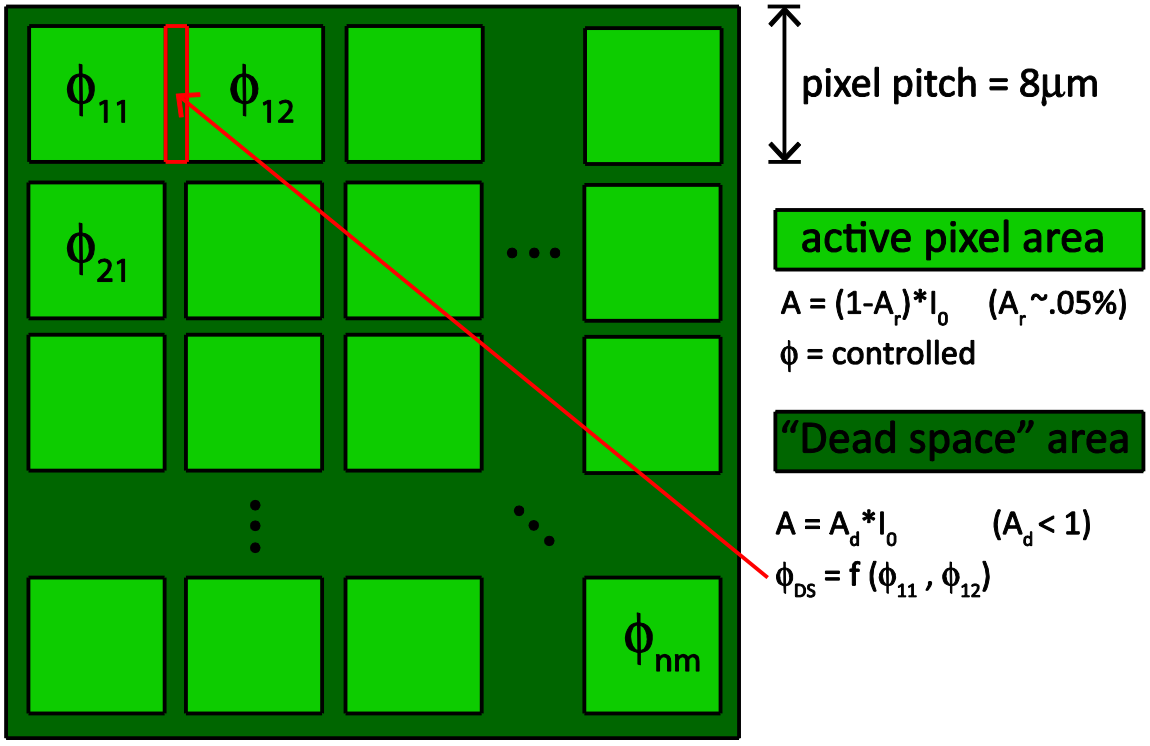

Figure 3-6 – model of the SLM display. Reflection from the front surface is considered in addition to "dead space" between pixels where the phase value depends on the values in adjacent pixels.

Prior work has sought to redistribute power and suppress the intensity of the zero order mode (*68–71*). In this work, we eliminate the effect of the zero order by placing a physical barrier at the target image plane. With this barrier in place, the unwanted high intensity is reflected away from the build volume and the remaining portion of the image propagates through. The original image is recovered at a plane beyond the original target plane, herein referred to as the "hologram plane" by adding a lens phase to shift the focal point of the target image. The focused image at the hologram plane is then relayed to the target volume by an additional 4f system.

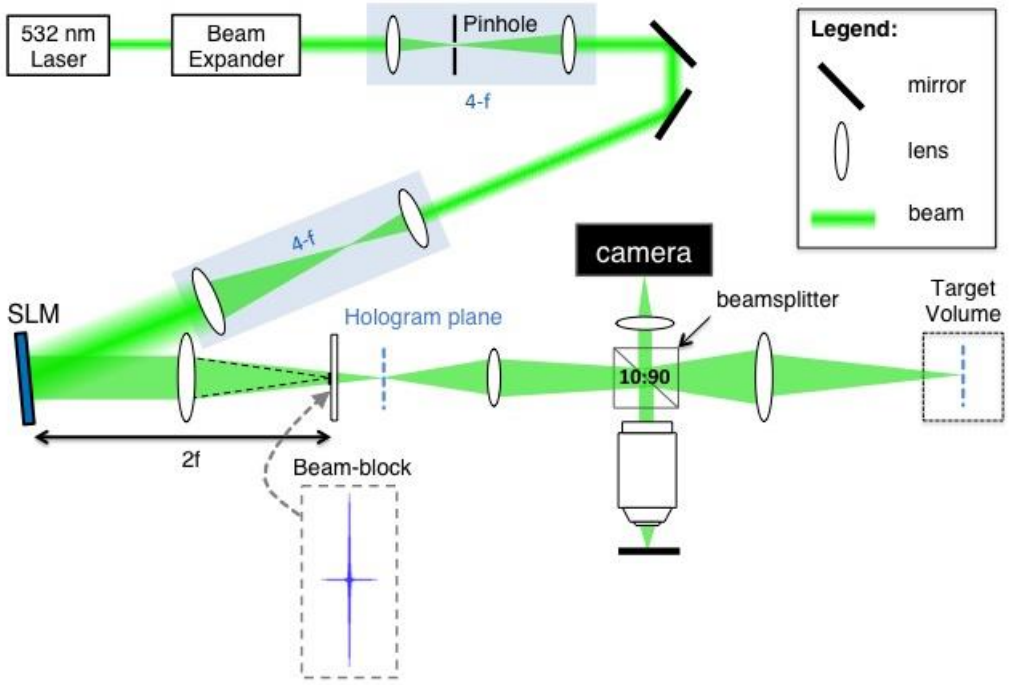

Figure 3-7 Modified holographic lithography system configuration. Beam block added to suppress zero order mode intensity in final image. Camera system added to image hologram quality.

Note that the effect of the zero order mode can also be eliminated by a change in the core hardware. This could be done, for example, by using amplitude modulation, rather than phase modulation and operating in a 4f system image plane rather than a 2f system in the Fourier plane. This can be achieved through the use of a digital micromirror device (DMD) rather than a reflective LCOS display. A DMD operates by flickering a pixelated array of micromirrors at rates of up to tens of thousands of frames per second. When the pixel is in the "on" state, the corresponding micromirror directs light towards the image. In the "off" state, light is directed away. In the CAL system of Chapter 4 as well as the precursor sequential exposure system of Section 3.11, a DLP projection system which controls amplitude rather than phase is utilized. The central bright point is not observed in this optical system.

3.4 3D Hologram Generation

This section describes a method to generate a three-dimensional holographic intensity pattern aimed at use for curing of a photosensitive resin. An attempt was made to use generation of multiple DOEs to create a 3D intensity profile for volumetric curing. Printing of multiple layers simultaneously requires generation of multiple DOEs. DOEs were computed for multiple slices and combined into a single final DOE which contained information for all slices. The final DOE was generated by random selection of the phase value from one of the merging DOEs for each pixel in the final DOE.

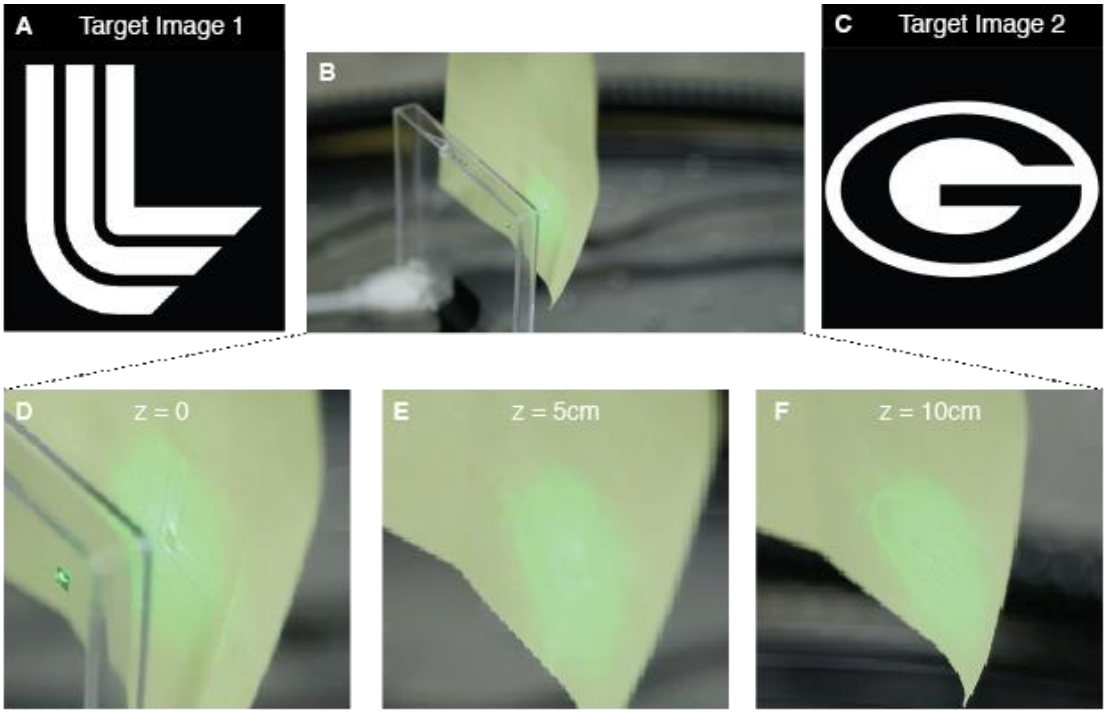

Figure 3-8 3D intensity output from a single DOE containing two target images for two separate slices in the 3D volume. (A) Target image used for the first slice at z=0. (B) Image of paper sheet used to view intensity output in the build volume. (C) Target image for a second slice at z = 10cm. (D-F) Images of the intensity output from a reflection from a paper sheet at various positions along the propagation z direction.

Figure 3-8 shows an example of multiple slice intensity generation from a single DOE. Two target images were used, as illustrated in Figure 3-8A and Figure 3-8C and were set to be separated in the axial (z) direction by a distance of $\Delta z = 10\ cm$. As evidenced in Figure 3-8D and Figure 3-8F, the two target images show up fairly clearly at the desired planes. The area in between shows a transition between the two target images as demonstrated from the mid-plane intensity shown in Figure 3-8E.

3.4.1 Holography Limitations

Some work has been done to generate complex three-dimensional images from a single SLM (*72*,*73*), but the results exhibit poor axial resolution. This results from a limitation on available hardware. The SLM pixel size (about $\sim$2–4 μm in the smallest available cases) sets the angle of the first diffraction order and thus the numerical aperture of the optical patterning system. As evidenced from Figure 3-8, this presents difficulty in creating 3D patterns with fine features in the beam propagation direction. While Figure 3-8 demonstrates patterned optical images at multiple planes, this pattern is impractical for printing due to the 10 cm distance between slices. Patterning of slices in closer proximity degrades the clarity and image contrast of each image.

3.5 Two-Beam Superposition

In order to address the limitations and poor resolution in the *z* dimension in holographic patterning from a single phase SLM, the system was reconfigured to allow light access to the photoresin from multiple orthogonal directions. By superposition of intensity fields from orthogonal angles, the range of 3D intensity fields that can be generated is expanded. The first modification to the volumetric printing system involved addition of a single mirror to direct light into the resin volume from an angle orthogonal to the initial propagation direction. A schematic of the system modification is shown in Figure 3-9A and an image of the system is given in Figure 3-9B.

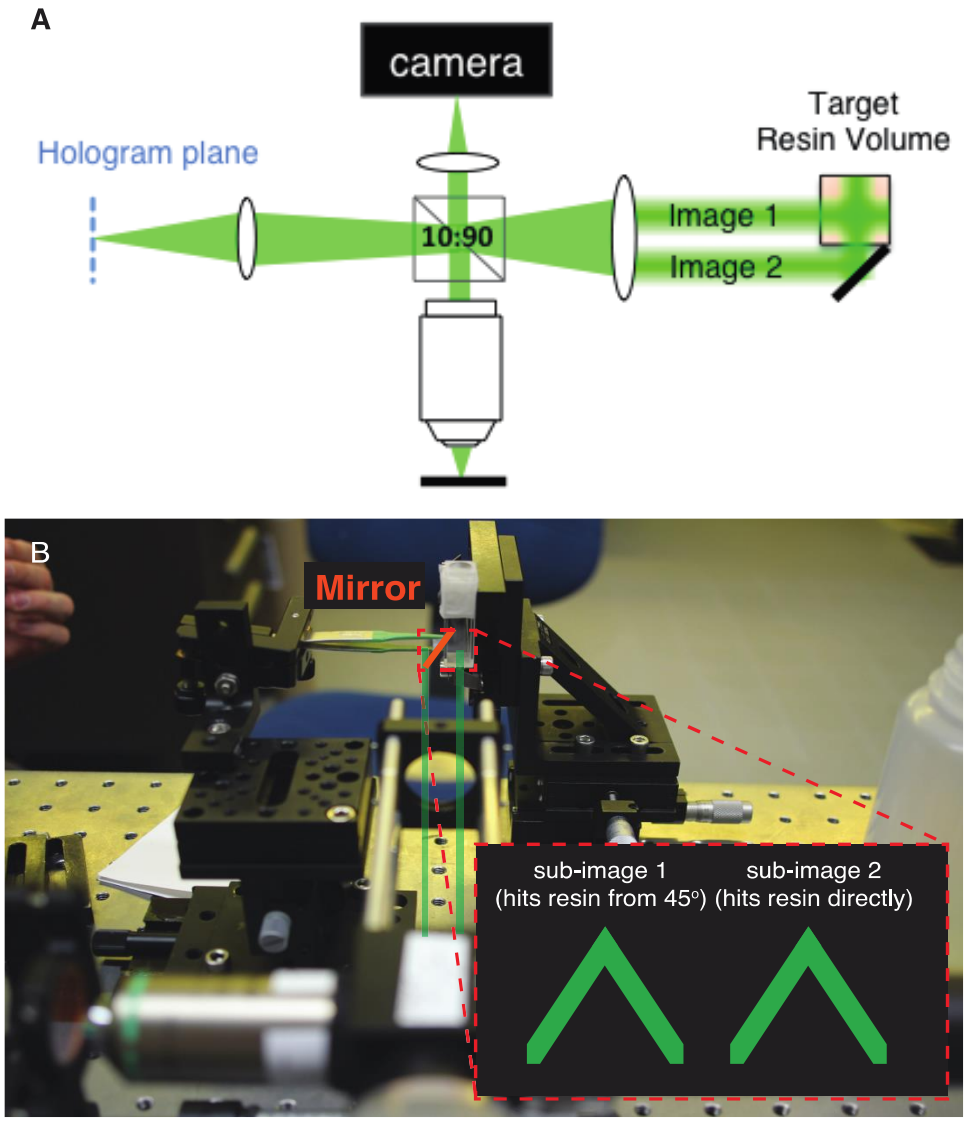

Figure 3-9 Two-beam superposition volumetric printing system. (A) Schematic and (B) system image.

In the new system, the target image was set to contain two sub-images. The first sub-image was set to come to focus at the center of the resin volume and entered the target volume from the original beam propagation direction. A second sub-image was designed to be reflected by the mirror and enter from an orthogonal direction. The second image, which has a longer optical path length to the center of the target volume, was generated by a DOE with a lens phase with longer focal length compared to the first image. This allows the second image to focus at the center of the target volume. Each of these two images propagates through the 3D target volume, and the 3D intensity profile inside the target volume becomes the superposition of the two propagating images. In a simple case, each sub-image contains binary information, with each pixel bright or dark. Figure 3-9 represents such a case, where each sub-image contains an inverted triangle with finite thickness. In this case, where intensity is not modulated within the projected image, the 3D intensity profile has maxima where the two projected images intersect in 3D space, with twice the intensity delivered to regions of intersection compared with outside regions where no intersection occurs. Using superposition of the propagated sub-images in Figure 3-9, a 3D geometry is formed at the intersection. Figure 3-10A and B depict each sub-image propagated through the volume. Figure 3-10C shows the regions in 3D where the two propagated sub-images intersect. The regions in C contain twice the intensity compared to the regions in A and B. Note that this optical propagation model assumes collimation of the sub-images, a reasonable assumption when the focal length of the Fourier lens is much longer than the spatial extent of the target volume.

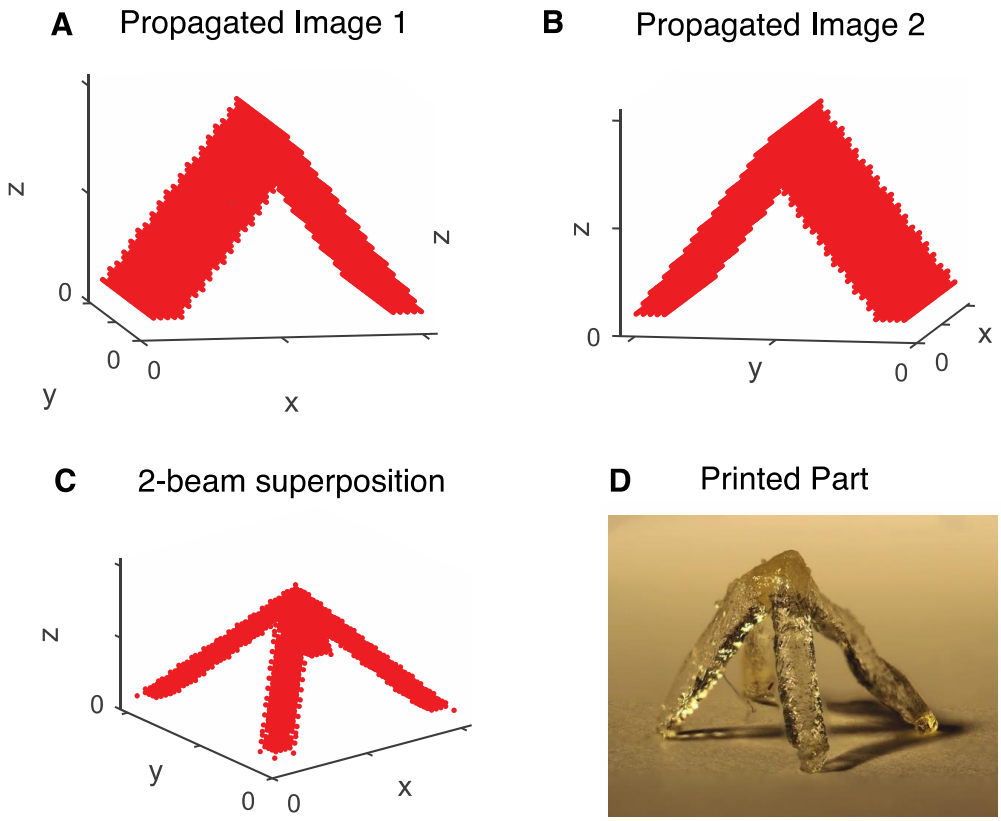

Figure 3-10 (A) Visualization of image 1 propagating through the *y* direction to create a 3D intensity profile and (B) image 2 propagating through orthogonal direction *x* to form a second 3D intensity profile. (C) The Superposition of images 1 and 2 in 3D space. Plotted regions correspond to points where images 1 and 2 intersect. (D) The printed part after exposure and rinsing.

When the 3D intensity profile of Figure 3-10 is projected into the resin volume, illumination exposure can be controlled such that regions that receive twice the sub-image intensity form a solid part, as depicted in of Figure 3-10D, and regions which receive contribution from just a single image do not form. This possibility is enabled by the oxygen inhibition phenomenon described in Chapter 2. Oxygen inhibition provides an energy threshold, below which minimal photocrosslinking occurs.

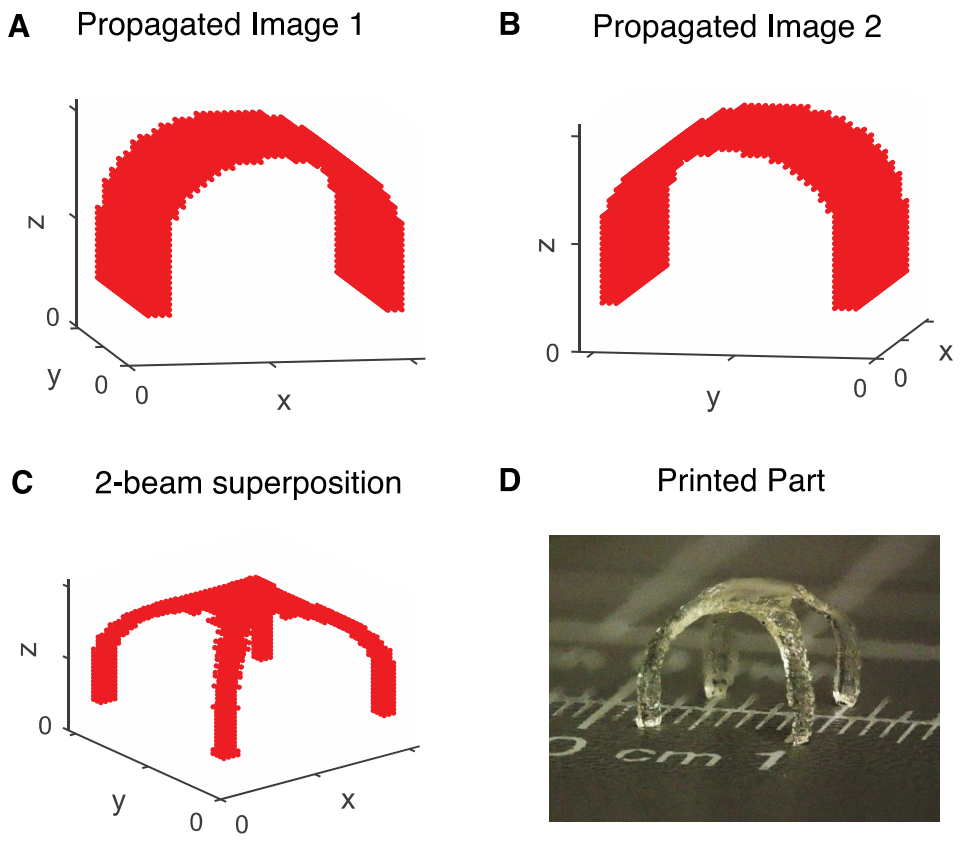

Figure 3-11 Another example of a geometry formed by the intersection of 2 beams. (A) Visualization of image 1 propagating through the y direction to create a 3D intensity profile and (B) image 2 propagating through orthogonal direction *x* to form a second 3D intensity profile. (C) The Superposition of images 1 and 2 in 3D space. Plotted regions correspond to points where images 1 and 2 intersect. (D) The printed part after exposure and rinsing.

With the two-beam superposition principle, it is possible to print a range of useful geometries. Figure 3-11 is an example of an interesting geometry that is difficult to print using conventional serial AM techniques. This geometry contains curved surfaces which would exhibit layering or "stair-stepping" artifacts when printed by conventional methods. With the volumetric approach, the curved geometry is formed in a single step, in seconds, with no layers.

Figure 3-12 shows additional examples of 3D parts that can be formed using the two-beam superposition approach to give a sense of the geometric complexity achievable. The geometries of Figure 3-12A and B have been demonstrated in practice. Figure 3-12D represents the first geometry presented thus far that is formed from two sub-images that are not identical and serves to preview additional geometric possibilities.

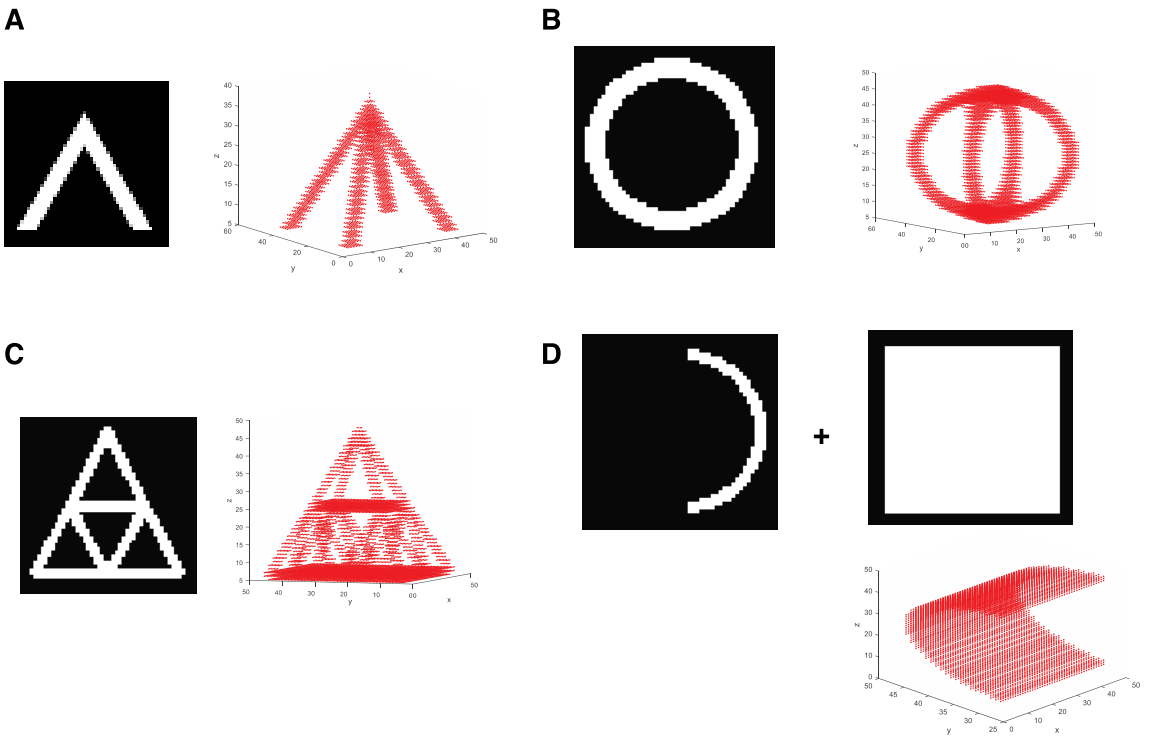

Figure 3-12 Examples of geometries that can be formed by superposition of two collimated optical beams. While these geometries display some complexity, the space of printable geometries is highly limited.

While the presented results are exciting in that they demonstrate ultrafast printing of 3D geometries volumetrically, the space of printable geometries that can be generated from superposition of two collimated optical beams is limited.

3.6 Three-Beam Superposition

To further extend the space of printable geometries in volumetric printing by superposition of patterned optical beams, the next logical step taken was to again modify the physical system, this time to allow for simultaneous exposure from an additional angle, totaling three orthogonal angles. The system of Figure 3-9 was reconfigured by building in a second mirror as shown in Figure 3-13 to allow for simultaneous exposure from a third beam.

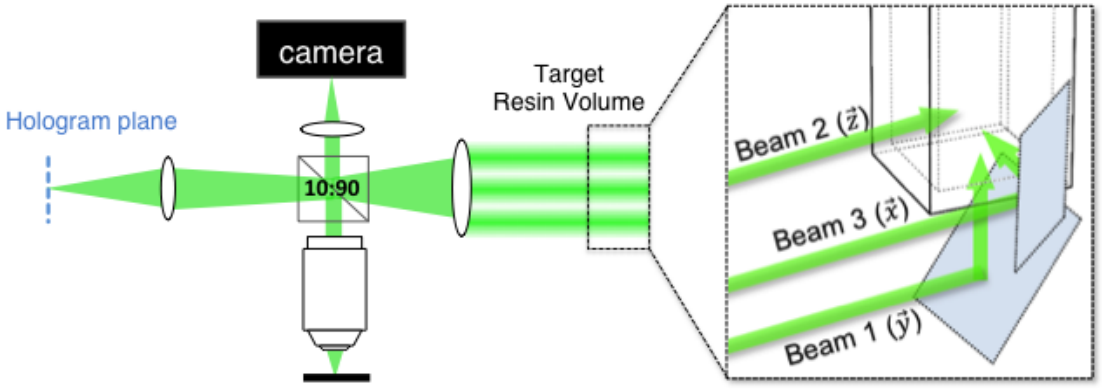

Figure 3-13 System modifications for three beam superposition. Holographic image is split into three sub-images that enter the build volume from orthogonal angles.

In the three-beam superposition system, regions within the target volume where all three images intersect receive three times the intensity present in a single image. Other regions in the volume receive zero, one, or two times the intensity in each individual image. Figure 3-14C shows an example of a type of structure that can be printed from superposition of three beams that is not possible from the superposition of only two beams and Figure 3-15 shows the printed structure itself. The three-beam superposition system necessitates an ability of the resin to resolve 3:2 optical contrast. That is, regions where three beams intersect must become sufficiently stiff during curing for the printed part to hold its shape before regions with intersection of two beams begin to form.

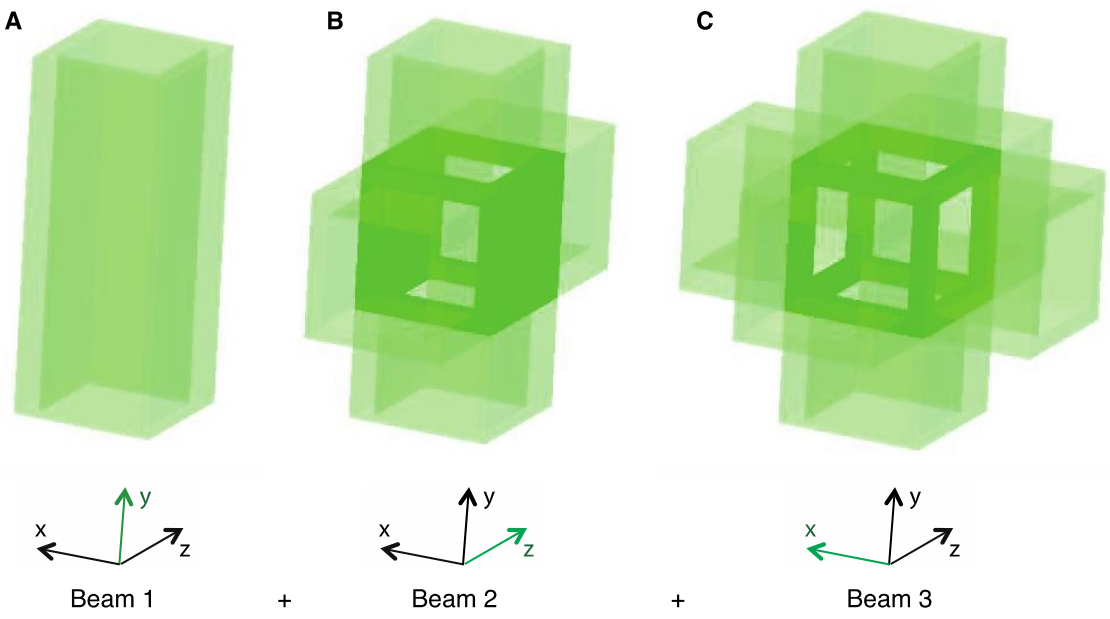

Figure 3-14 Example of three beams, each patterned with a square image, intersecting within the build volume. (A) A single square projection propagates in the vertical (*y*) direction. (B) A second

projection enters from the *z* direction. Regions where the two projections intersect are highlighted in dark green. (C) The third projection enters from the *x* direction. Here, only regions where all thee beams intersect are highlighted in dark green.

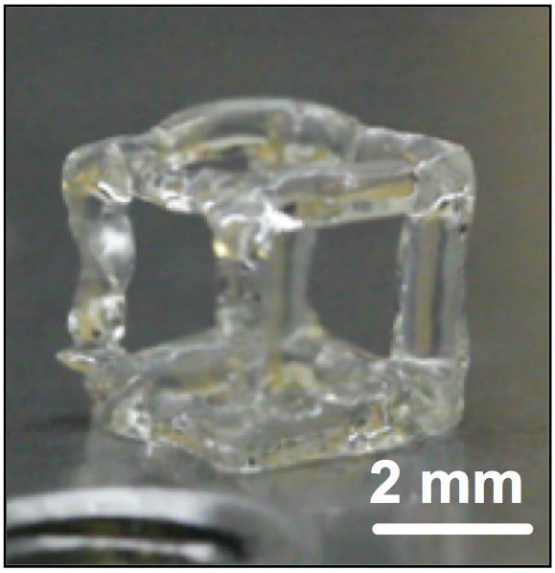

Figure 3-15 Cube structure printed by three-beam superposition of square images and the intensity superposition shown in Figure 3-14.

Figure 3-16B presents another example of a geometry with added complexity compared to what is achievable with two sub-images. The sub-images from the sides come in the form of a triangle while the bottom image helps to form the bottom of the pyramid. This geometry is generated using the system of Figure 3-13.

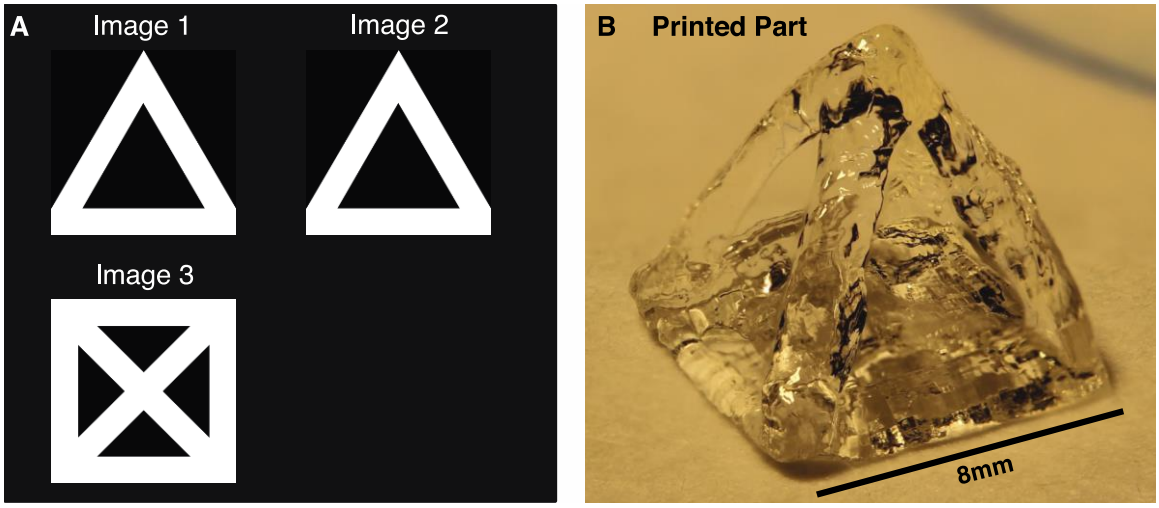

Figure 3-16 An example of a part printed using three-beam superposition with variation in the image projected from orthogonal directions. A) Projected images from front, right, and bottom. The bottom image (Image 3) contains a different geometry from images 1 and 2. B) The 3D part printed from the images in A.

3.6.1 Lattice Structure

Figure 3-17 represents an example of a useful geometry that can be formed from three constant intensity sub-images. This figure presents a lattice geometry, which is expected to exhibit high strength to weight. A 2 × 2 lattice cube print is demonstrated. However, this principle could be readily extended to print a similar with mush greater repetition of the unit cube cell. The spatial extent of such a lattice would be limited only by the number of pixels in the SLM.

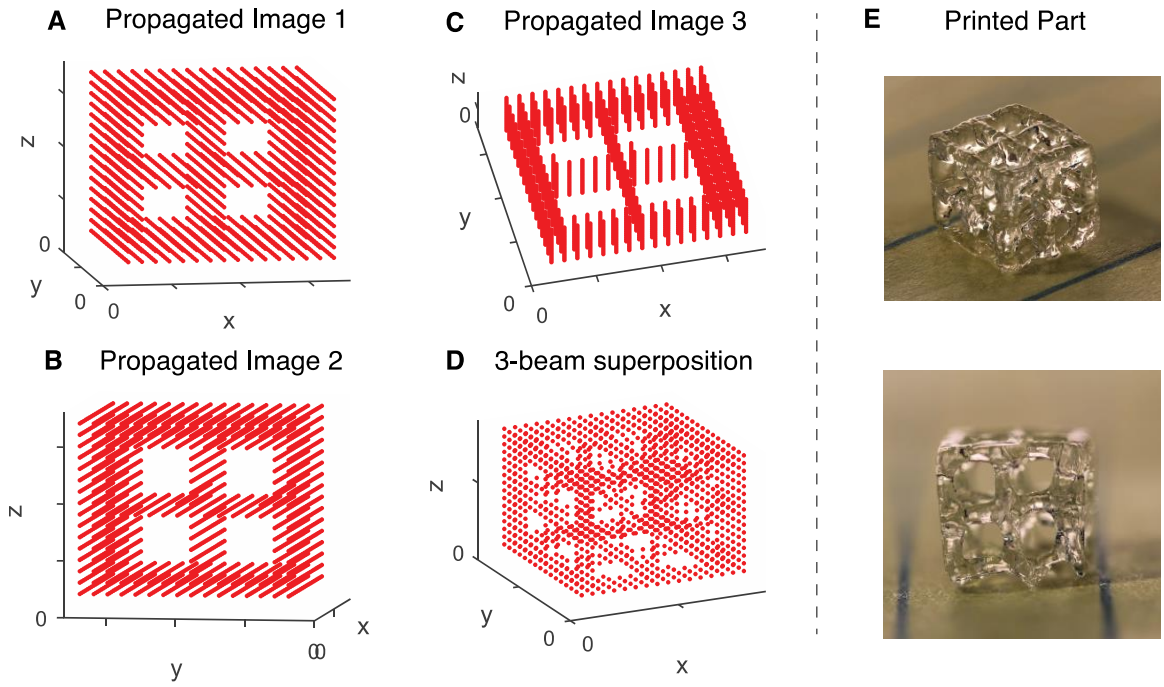

Figure 3-17 A lattice structure formed by the superposition of three beams. (A-C) Beams 1-3 propagating in the *x*, *y*, and *z* directions respectively. (D) 3D superposition of the three patterned collimated images. (E) A 3D lattice structure printed by superposition of the three beams.

3.6.2 Laser Speckle Effects

Here we add a quick note that the use of a coherent laser in this system, which necessary for generating holographic images, presents an adverse effect with respect to the surface quality of printed parts. Laser speckle (*74*) causes some parts to exhibit surface roughness. Figure 3-18A shows this effect. Here a thin, effectively 2D sample held between glass microscope slides (following a similar procedure to that used in Chapter 2) is illuminated with a static laser, CGH-generated pattern and then rinsed with a solvent. In the microscope image of Figure 3-18A, the effect of laser speckle on the printed photopolymer is evident. To mitigate this effect, static images are instead generated as a set of CGHs sequentially displayed at ~60 Hz, where each CGH is generated with a random initial phase. This serves to smooth out the speckle effect in the resin response as evidence by the image in Figure 3-18B.

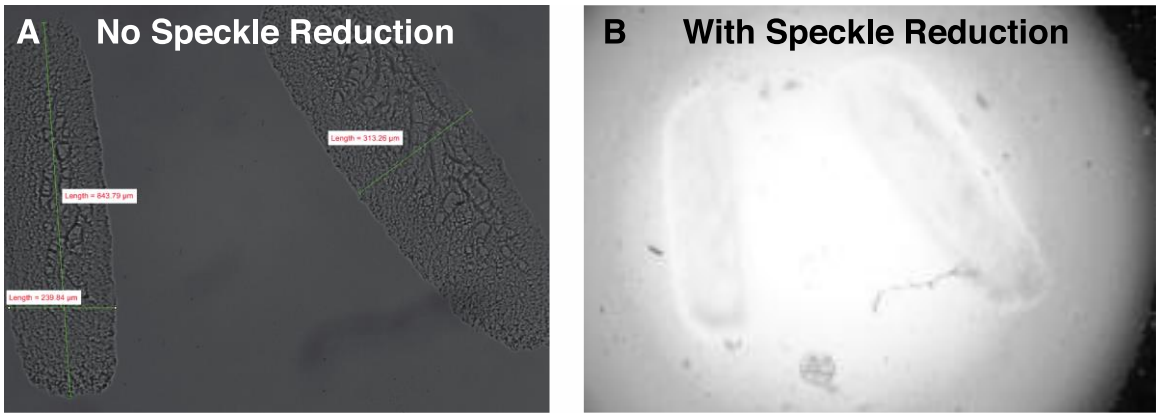

Figure 3-18 A thin 2D geometry printed to demonstrate the effect of laser speckle on resin curing. (A) Laser speckle induces inhomogeneities in the recording material. B) Speckle inhomogeneities appear to be removed by hologram averaging.

The effect of laser speckle could be fully eliminated by the used of amplitude, rather than phase, modulation in the optical system. Again, this is done in the Computed Axial Lithography system of Chapter 4.

3.7 Resin Response

In this chapter thus far, we have considered only optical patterning and generation of three-dimensional intensity fields with no consideration of the resin response to the incident illumination. Resin response in two-dimensions has been thoroughly characterized in Chapter 2. This section considers the resin response when adding the third dimension.

3.7.1 Resin Components

The printed results presented so far, and throughout this chapter unless noted otherwise are produced from a photopolymer composed of a single pre-polymer and photoinitiator molecule. The pre-polymer used is again Poly(ethylene glycol) diacrylate (PEGDA). In this chapter, a shorter-chain version of PEGDA, with average molecular weight equal to 250 Da is used. The photoinitator is Irgacure 784, selected for its ability to absorb at the illuminating wavelength of 532 nm.

3.7.2 Resin Absorption

In sections 3.5 and 3.6, a superposition of intensity fields is described which generate intensity maxima to overcome an inhibition threshold only in select regions, where beams from all (two or three) incident directions intersect. In practice, the liquid resin material used to form the printed part does interact with light and affect the 3D intensity profile. The most important effect to consider is optical absorption. As each beam and sub-image propagates through the resin material, light is absorbed and the intensity profile of the propagating sub-image is attenuated. Attenuation along the propagation direction changes the intensity

profile and thus affects the thresholding behavior of the resin. To minimize this effect, photoinitator concentrations in the 3D volumetric system were carefully designed to give reasonable attenuation values at the illuminating wavelength. To set the photoinitiator concentration, absorbance values for the photoinitiator and resin were measured using UV-VIS spectrophotometry. Absorbance as measured by the UV-VIS spectrophotometer is defined as given in Equation 3.14 where A_λ is the absorbance at a particular wavelength of illumination, T_λ is the transmittance at that wavelength and Φ_λ is the photon flux at the same wavelength. The subscripts *i* and *t* refer to, respectively, the incident flux on the material volume and the transmitted flux.

$$A_\lambda = \log_{10}\left(\frac{\Phi_{\lambda,i}}{\Phi_{\lambda,t}}\right) = -\log_{10}(T_\lambda) \tag{3.14}$$

Measurements were taken from a rectangular cuvette volume with path length l of 10 mm. From this measurement, the molar absorptivity ϵ of the photoinitiator was extracted, according to Eqn. 3.15 where [PI] is the molar concentration of the photoinitiator in solution and l is the optical path length through the cuvette:

$$A(\lambda) = \epsilon(\lambda) * [PI] * l. \tag{3.15}$$

From the Beer–Lambert law, the incident intensity at a depth z into the material volume was modeled as a function of the surface intensity I_0 according to Equation 3.16.

$$I(z) = I_0 e^{-2.3\epsilon[PI]l} \tag{3.16}$$

The exponential attenuation of Equation 3.16 acts in each direction of illumination (*x*, *y*, and *z*). Figure 3-19 gives an example of what the intensity profile on the face of a cube structure (such as the one shown in Figure 3-14 and Figure 3-15) looks like for an arbitrary value of *A*. Intensity is non-uniform but can still provide sufficient contrast to print the desired structure. By illuminating with a source wavelength off the absorption peaks (532 nm), [PI] can be high enough to provide enough photoinitiator to complete curing while also providing the low required absorption.

In addition to absorption, a second effect also occurs during the curing process that can affect the curing behavior. As the photopolymer crosslinks, the refractive index increases. Changes in refractive index can perturb the incident illumination pattern. Fortunately, oxygen inhibition also helps address this effect as the geometry can be defined through localized depletion of oxygen before the material crosslinks and the optical properties change.

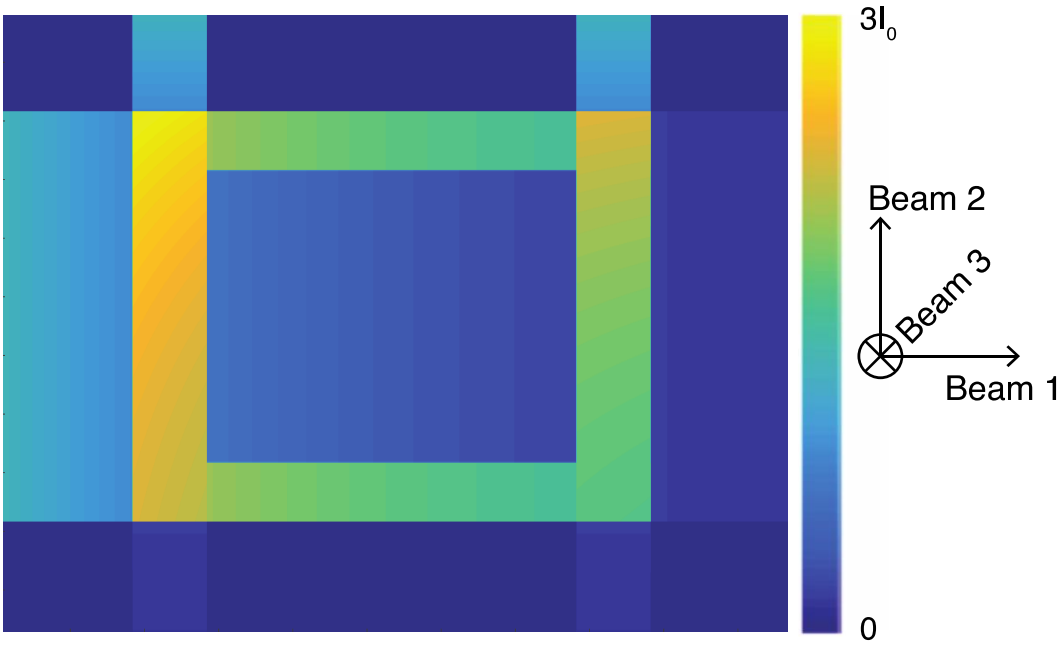

Figure 3-19 Example of the intensity distribution on a cube face after accounting for attenuation. The maximum possible value within the face is $3I_0$. Uniformity depends on the resin absorption parameter or penetration depth. Resins with lower absorption give better uniformity.

3.8 Limitations of Multi-Beam Superposition

Just as the single beam holographic approach presents significant limitations the addressable 3D geometries that can be formed, so too does multi-beam simultaneous superposition. Only relatively simple geometries that can be formed from intersection of three orthogonal views can be formed. A core benefit of additive manufacturing is the ability to generate custom geometry on demand. While results from multi-beam superposition present an exciting proof-of-concept for volume-at-once 3D printing, an important next step is to continue to further expand the space of printable geometries toward full customization.

3.9 Multi-Exposure Volumetric Printing

One potential route to expanding the geometric flexibility of three-beam superposition could include rapid switching of the patterned-intensity sub-images at time scales much shorter than that of the photocuring reaction, similar to that performed in the speckle reduction effort in Section 3.6.2. A three-dimensional geometry could be formed from a merging of 3D sub geometries. An attempt was made to perform this method on a bowl shape geometry as seen in Figure 3-20A. Each set of sub-images was designed to print a slice of the hemisphere. In order for the material to be able to record multiple exposures in this manner, it is necessary for the resin to reset between exposures. With the PEGDA/I784 resin used, the timescale of oxygen diffusion to reset the resin memory is far too long for practical

printing. This becomes evident when reconsidering the Stokes-Einstein relation of Equation 2.18. In order for the resin to reset, there must be sufficient oxygen diffusion back into the previously exposed areas between exposures. To get a sense of the timescale of oxygen diffusion in the resin we may consider the diffusion time as computed in Equation 3.17 at relevant length scales.

$$t_{diff} = {x^2}/{D} \tag{3.17}$$

In the demonstration of Figure 3-20, the side length of the rectangular volume is $1cm$. If we consider diffusion of oxygen across half the side length ($x = 5mm$) (from the boundary to the center), with a viscosity of $12cP$ measured for PEGDA 250, the diffusion time comes out as $t_{diff} = 8.19\ hours$. This is much longer than the desired timescale of printing which is on the order of seconds. The density increase of the cured part causes slices of the shell to sink long before the resin resets. If slices are printed in quick succession, the resin does not reset and unwanted curing occurs as seen in Figure 3-20B.

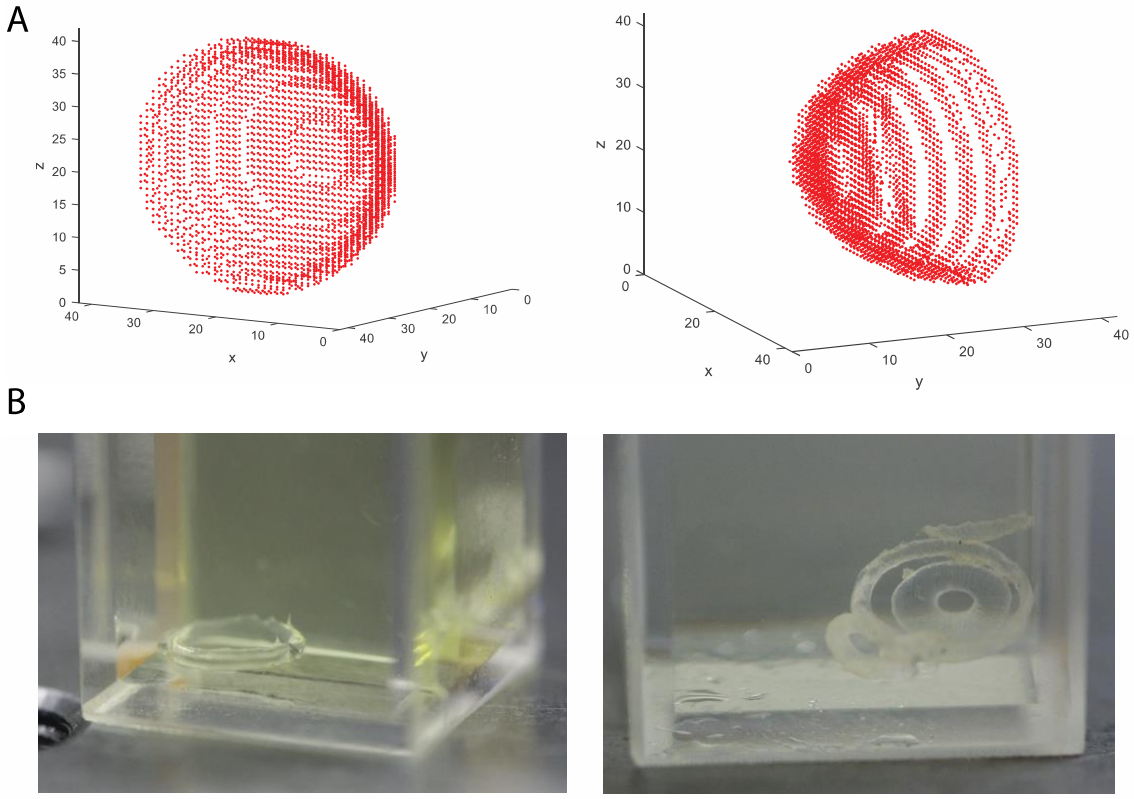

Figure 3-20 Multi-exposure volumetric printing attempt. (A) A sphere geometry is formed from a set of sub-volumes, each generated by three-beam superposition. (B) Exposures fail due to sinking of cured parts before resin reset or due to unwanted extra curing.

3.10 Multi-Wavelength Volumetric Exposure

In another effort to expand the geometric versatility of the multi-beam exposure printing approach, the possibility of using a two-wavelength exposure scheme was also explored. The principle behind this exposure scheme was to use one wavelength to initiate polymerization and a second wavelength to prevent polymerization. A second laser with 450 nm wavelength was built into the system (initially to expand the range of usable photoinitiators). An example of an illumination pattern to be used in a two-wavelength scheme is given in Figure 3-21.

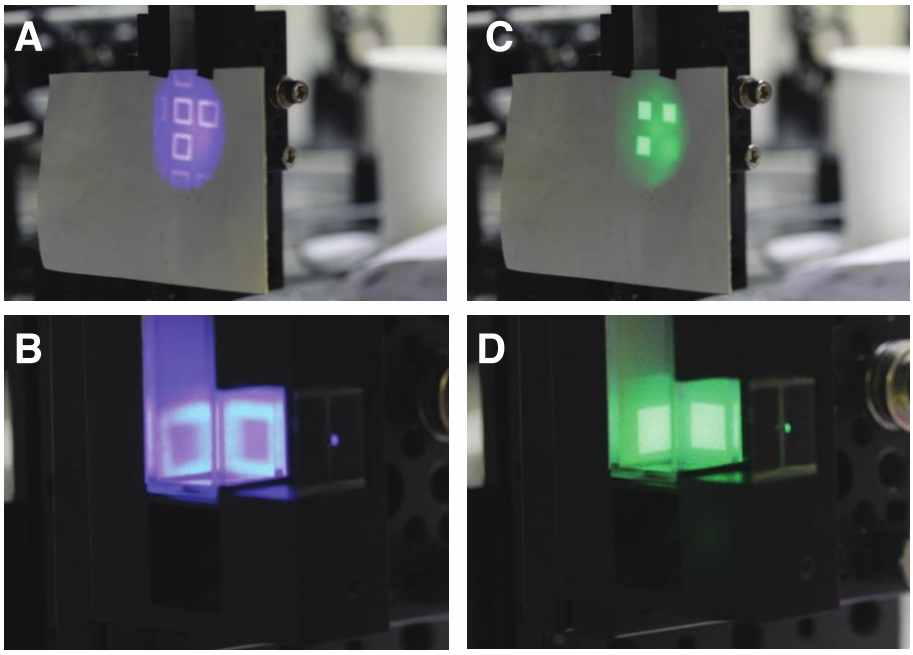

Figure 3-21 Example two-wavelength initiation/inhibition pattern. A-B: blue light initiates polymerization on the edges of a cube. C-D: green light acts as an inhibiting wavelength to prevent overcure and increase contrast in the chemical response.

There are at least two potential approaches that could leverage multi-wavelength illumination toward volumetric curing. The first is the process of Stimulated Emission Depletion (STED), a technique originally developed in microscopy (*75*–*77*), and also used in some lithography applications (*78*,*79*). In this process, an excited radical photoinitiator species can be de-excited through stimulated emission of a photon. This process, however, requires exceedingly high intensity from pulsed laser sources, making it impractical for macroscale 3D printing. A second possibility is the process of photoinhibition (*80*,*81*). In this process, a second light-activated species is added to the resin. This species, when activated, acts as an inhibitor to the photopolymerization reaction, much in the same way that oxygen does. This is much more practical at the available optical powers. However, even with controlled inhibition, the space of printable geometries remains too constrained. A different approach is used instead.

3.11 Sequential Exposure Printing

The solution arrived at in this thesis to expand the space of printable geometries in volumetric fabrication to arbitrary was to increase the number of optical images and angles utilized. However, with the current hardware design concept, a limit exists on the number of images that can be projected simultaneously. As the number of projected images increases, an increasing number of mirrors or sources are required. As the number of projections gets beyond 10 to 100 or more, major hardware innovation may be required to be able to deliver all projections simultaneously.

In order to address the challenge of delivering more projections, a new apparatus was constructed to employ a time-multiplexed version of multi-beam superposition. The new system delivers a single projected patterned 2D image toward a cylindrical resin volume on a rotating stage. The relative angle between the projected image and the resin volume is set by the stage. To test the validity of time-multiplexed multi-beam superposition, a first experiment involved a simple geometry, similar to one used in the two-beam system. The geometry used is shown in Figure 3-22B. The inverted triangle geometry was projected from four different orthogonal angles sequentially, as illustrated in Figure 3-22C. Projections were delivered at each angle for a total of 2 s and two total exposures were delivered from each angle for a total of 2 full rotations of the vial. This experiment demonstrates the ability to print a three-dimensional part volumetrically from time-multiplexed exposures as evidenced by the printed part shown in Figure 3-22D.

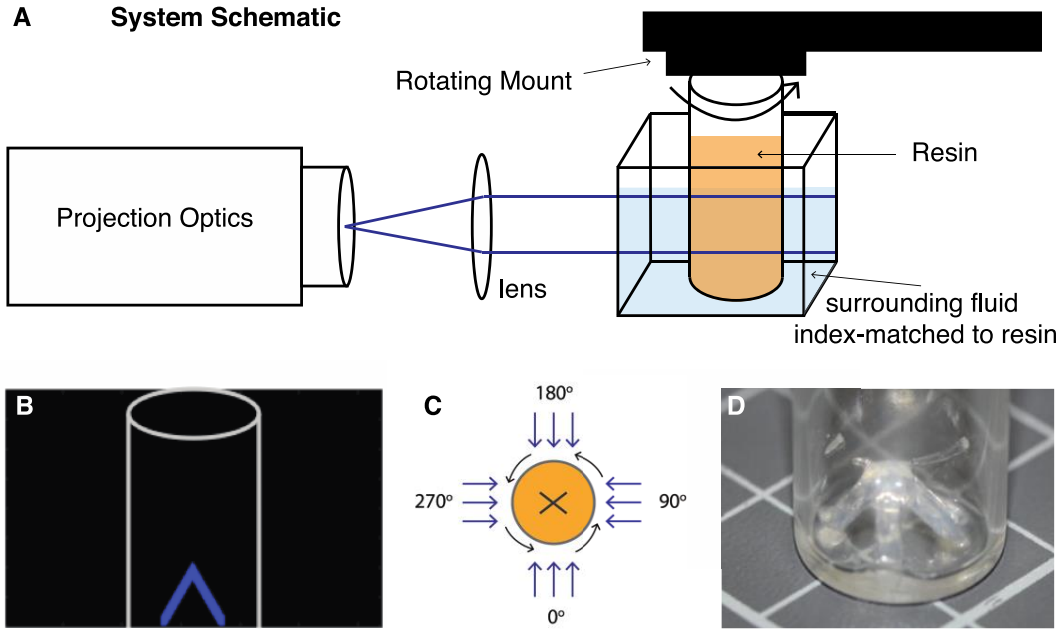

Figure 3-22. Sequential exposure printing demonstration. (A) Schematic of the new system built for sequential exposure. (B) Static image projected from all angles in this experiment. (C) Exposure recipe: expose from four angles sequentially. (D) Final printed 3D part.

Chapter 4 Computed Axial Lithography

As previously stated, the core contribution of this thesis is the conception, development, and implementation of a novel additive 3D patterning technology—Computed Axial Lithography (CAL)—which provides a path to volumetric fabrication of arbitrary geometries. This chapter discusses in detail the development of CAL. CAL follows directly from systems constructed in Chapter 3 and leverages an understanding of photochemistry gained through the development of the models in Chapter 2. The core principle of CAL follows from the illustration in Figure 4-1. Similar to the multi-beam superposition method, a vat of photosensitive resin is contained within an optically transparent container and illuminated with patterned projections from a number of different angles. The CAL concept considers creating a set of $n \gg 3$ projections oriented about a single axis. The process is inspired by the image reconstruction procedures of Computed Tomography (CT), which has become ubiquitous in medical imaging and non-destructive testing (*82*,*83*) but whose core concepts have not been applied to additive fabrication. In the CAL process, light energy is delivered to the material volume as a set of two-dimensional images. Each image projection propagates through the material from a different angle. The superposition of exposures from all angles (Figure 4-1) results in a three-dimensional energy dose sufficient to solidify the material in the desired geometry.

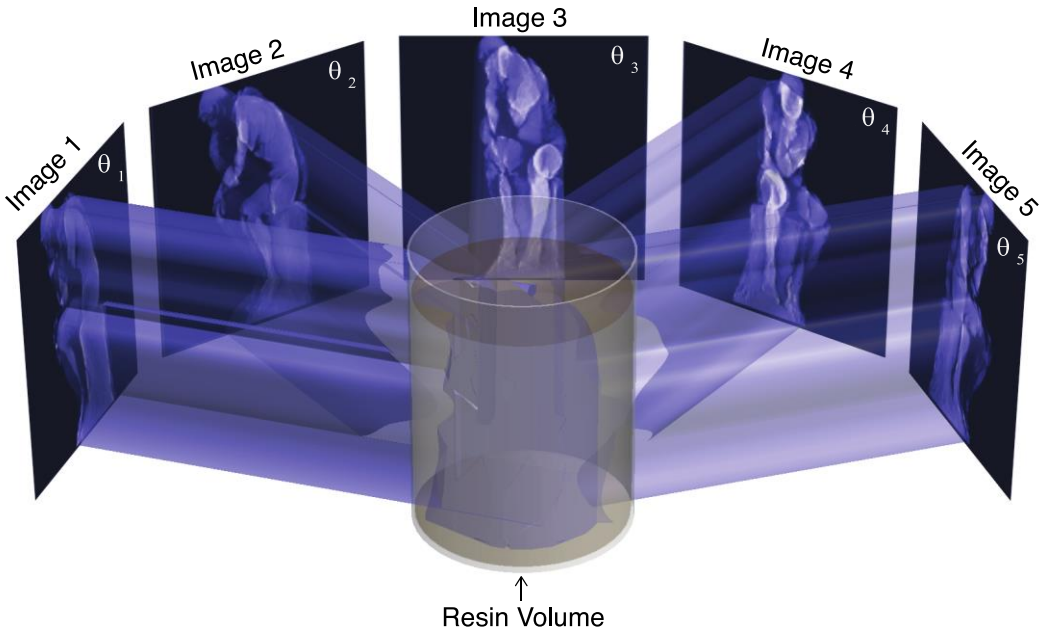

Figure 4-1 The core operating principle of CAL. Patterned 2D images from select angles about a vertical axis are used to construct a 3D exposure dose within a photosensitive material in order to directly print a 3D structure.

As described in Section 3.11, the delivery of $n \gg 3$ images simultaneously presents a major challenge in system design. To date, the hardware implementation of CAL has followed most directly from the initial sequential exposure printing system described in Section 3.11. A more detailed schematic of this system is given

in Figure 4-2. Here a DLP projector outputs a patterned 2D image where intensity is controlled independently in each pixel. The 2D image propagates through the 3D volume from a particular angle. The image is then switched as the material volume rotates to update the relative angle between projection and resin. In the implementation described in this thesis, a movie with frame rate ~25 Hz is played toward a rotating volume with angular velocity in the range ~3°–25°/s. The resin volume is submerged in a clear glass box filled with a fluid with refractive index matched to that of the resin in order to mitigate lensing effects at the curved interface where light hits the resin.

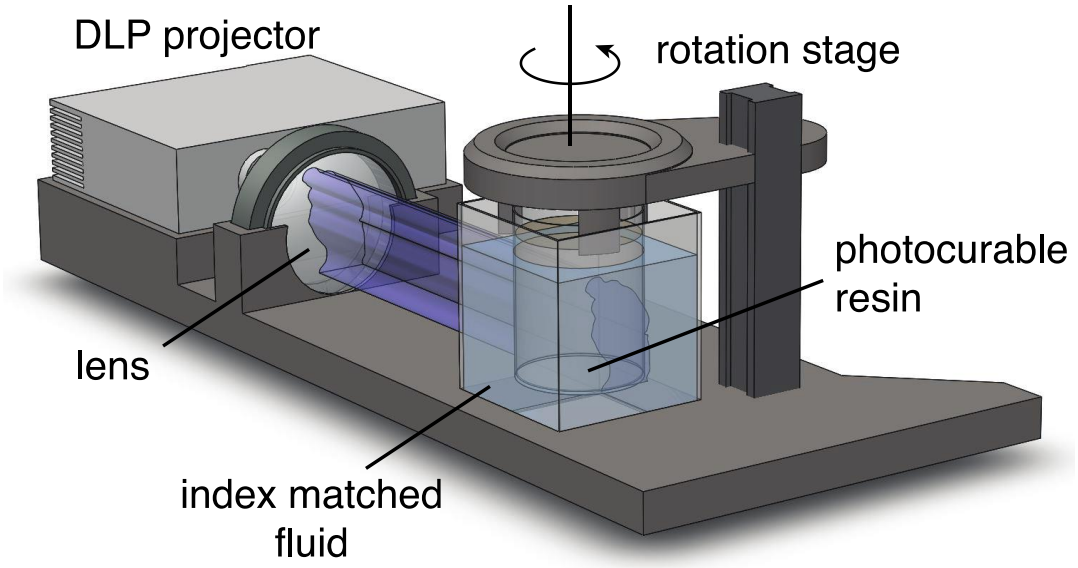

Figure 4-2 Schematic of CAL hardware implementation used in this thesis. A DLP projector creates a two-dimensional image that propagates through a volume of photosensitive resin from many different angles as the resin volume rotates. The material volume is submersed in a fluid with refractive index matched to the resin to mitigate lensing effects.

4.1 Tomography Image Computation

A core element in the implementation of CAL is the development of an algorithm to generate the necessary patterned 2D images of Figure 4-1 starting from a 3D model of the desired 3D geometry to be printed. The development of this algorithm was led by a close collaborator, and the description is thus somewhat condensed in this thesis. Further description of this algorithm is given in (*84*) and (*85*). A major acknowledgement goes to Indrasen Bhattacharya for taking the lead on algorithm development.

The CAL method is designed to expose the transparent resin by projecting 2D images from an array of angles about an azimuthal axis. As mentioned in the chapter introduction, the optical design method for CAL is based on one of the possible reconstruction procedures in computed tomography (CT). Prior art in a similar technique exists in intensity modulated radiation therapy (IMRT) for cancer treatment (*86*). IMRT seeks to produce a 3D variation of radiation dose in a target

volume in the patient's body. Typical practice in this radiotherapy procedure involves the projection of a small number (7–10) of 2D distributions of X-ray pencil beams at a few selected angles. The intensity of the beamlets is chosen to satisfy a set of therapeutic constraints including: sufficient but not excessive dosage in the tumor, low radiation dose in certain critical organs as well as the physical constraint that radiation dose must be positive. This is a challenging inverse problem, for which iterative optimization techniques have yielded success in defining previously impossible dosage distributions, including concave regions such as the prostate gland. Producing dose distributions in a clinically reasonable timeframe while satisfying multiple objectives continues to be an area of active research. From a mathematical perspective, the volumetric fabrication problem has similarities in terms of constraints, but greater freedom in the exact dose distribution because of the non-linear thresholding behavior of the photoresins used.

To describe the optical design algorithm, it is easiest to start by reducing the problem of generating 2D projections to print a 3D geometry to that of generating 1D projections to print a 2D geometry. Consider the 2D geometry to be a slice of the full 3D part as illustrated in Figure 4-3A. This 2D flatland analysis, depicted in Figure 4-3B-D, is then readily extended to the third dimension by concatenating calculated 1D projections for subsequent slices of the 3D part. Note that this technique is still distinctly different from layered printing because neighboring layers form simultaneously rather than sequentially. In the ray-tracing picture used in this algorithm, we consider all the beams for a particular projection angle to be parallel. This is analogous to parallel beam tomography in the medical community. In the CT imaging configuration where a uniform pencil beam at azimuthal angle θ is projected into the 2D imaging volume with optical density given by $R(x, y)$, the collected dose distribution on the 1D camera along the spatial dimension x is given by $P(x, \theta)$:

$$P(x, \theta) = \int R\,(x\cos\theta - u\sin\theta, x\sin\theta + u\cos\theta)du \tag{4.1}$$

Where $(-u\sin\theta, u\cos\theta)$ for parameter u represents a line through the origin in the direction of exposure for the particular angle θ. $P(x, \theta)$ is the well-known Radon transform of the 2D image R. We will refer to $P(x, \theta)$ as the angular projections of the image. From the projection slice theorem, it turns out that the Fourier transform of a projection at angle θ is exactly equal to a 1D sample of the original image's 2D Fourier transform $R(k_x, k_y)$. The 1D sample is taken along a slice $(k\cos\theta\,, k\sin\theta)$ corresponding to the particular angle at which the projection was integrated. This can be expressed as:

$$\int P(x, \theta)e^{-ikx}dx = R(k\cos\theta\,, k\sin\theta) \tag{4.21}$$

This is illustrated in Figure 4-3C-D, where 1D cuts in the projection space image can be compared to similarly shaded central slices in the Fourier domain. Sufficiently

dense sampling in the Fourier domain is required for an accurate CT image reconstruction.

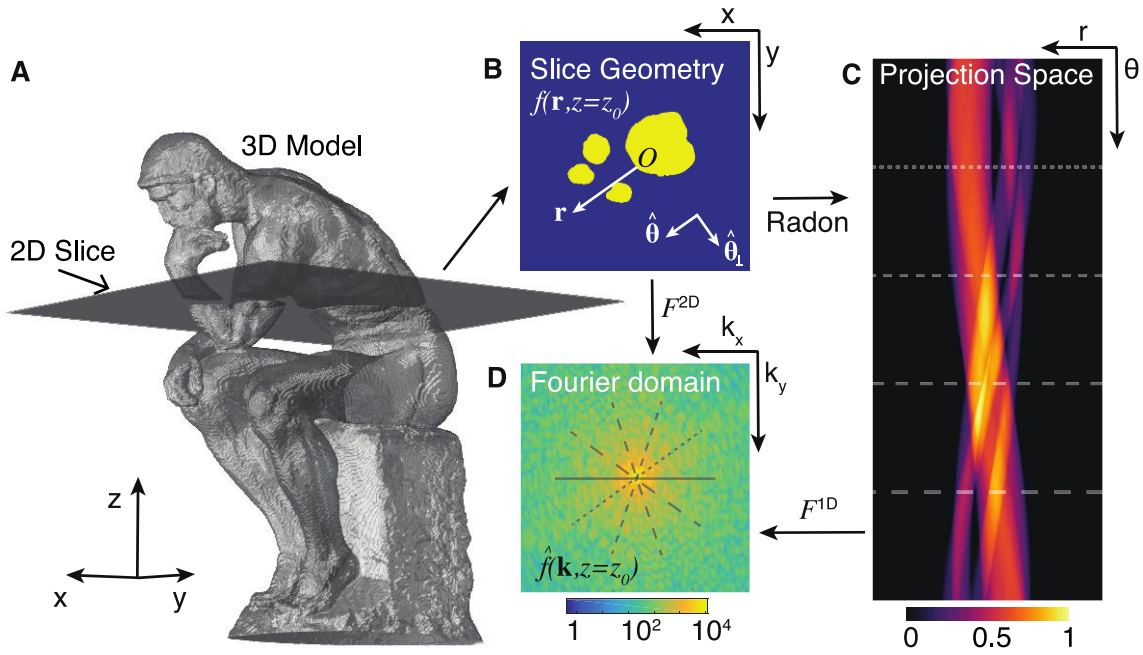

Figure 4-3 Schematic describing the underlying mathematical concepts used in the implementation of the CAL algorithm. (A) A 3D CAD model is sliced into parallel layers. Independent computation takes place on each slice. (B) 2D target geometry of the slices in A. (C) Projection space representation of the slice in B. (D) Fourier domain representation of the slice geometry. A 1D Fourier transform of a horizontal slice in C samples a slice through the center of the Fourier domain.

The reconstruction of the 2D image volume can be understood as an algorithmic time reversal of the CT imaging process. This back-projection algorithm starts with the measured 1D projections and propagates each individual projection backwards while uniformly exposing the target region with this intensity pattern. This is repeated for every angle. From the central slice theorem, this corresponds to building up the sample slice by slice in the Fourier domain. This algorithmic back-projection then motivates a technique to physically back-project the computed Radon transform at each angle and directly construct desired 3D dose volumes. However, directly back-projecting the 2D Radon transform will not produce the correct result. In order to compensate for the inverse radial oversampling inherent in the Fourier slicing approach, a radially increasing ramp filter is applied. We also apply a window to the ramp filter in the Fourier domain, so as to exclude high spatial frequencies beyond the degree of sampling provided by the number of angular samples. IMRT literature suggests an exponential windowing filter for a smooth backprojection filter. This approach leads to the following backprojection filter in the Fourier domain (k, θ):

$$H(k) = |k| e^{-\left(\frac{k}{k_0}\right)^4} \tag{4.3}$$

where k_0 is chosen based on the number of angular samples. This windowed high pass filter is applied on every Fourier slice before back-propagating it to form the image. The spatial domain representation of the filter has negative ripples that often lead to the backprojections being negative even if the projections themselves are positive. This is a challenge since the backprojections are physically constrained to positive values. We address this initially in two ways: 1) by adding a constant offset to all projections to raise the minimum value to zero, or 2) by setting all negative projection values to zero. We then use this set of projections as an initialization step for a constrained optimization procedure.

The goal of the optimization algorithm is to calculate the set of backprojections $P_{opt}(x,\theta)$ that best produces a desired output intensity. We use an iterative optimization procedure based on projected gradient descent. This method is guaranteed to converge for a convex objective and convex constraint set. Neither of these is true in the CAL case due to the thresholding property of the resin and discrete values for the projector input. However, this heuristic performs quite well for some simple geometries, and reasonably well for more complicated ones. One iteration of the optimization loop to generate $P_{n+1}(x,\theta)$ from $P_n(x,\theta)$ given a target image $R(x,y)$ goes as follows (illustrated in Figure 4-4):

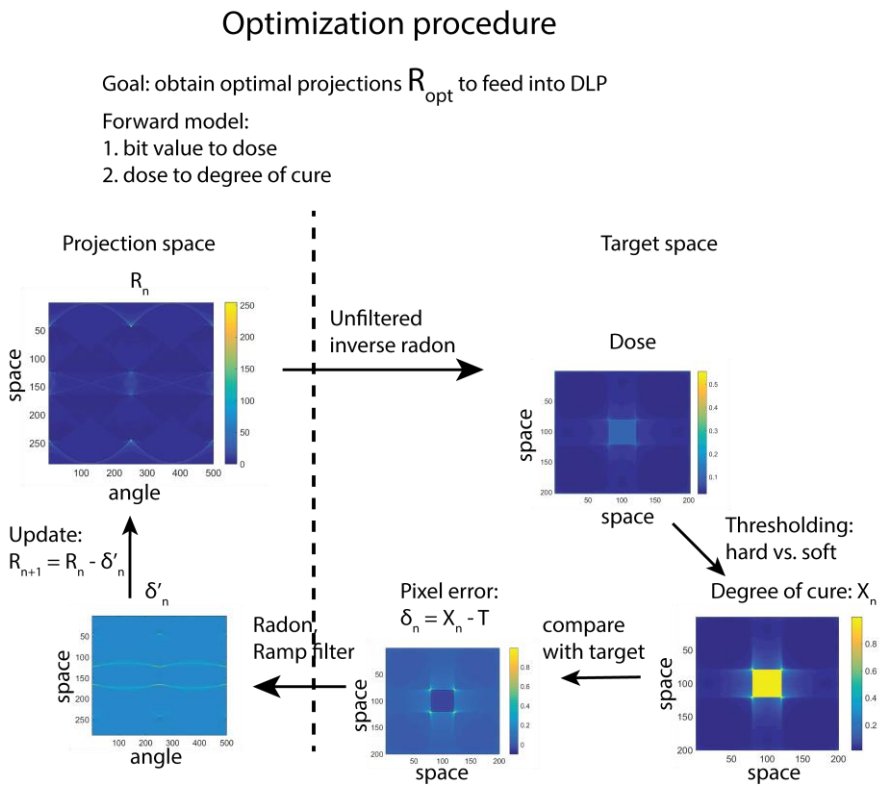

Figure 4-4 Schematic of the optimization procedure used to generate 1D projections from a target 2D 'flatland" geometry.

1) *Projection:* Starting with the 8-bit DLP projections $P_n(x,\theta)$ computationally generate an unthresholded 2D dose distribution of power $D(x,y)$. This requires an

accurate understanding and calibration of the system's forward model. The relationship between specified pixel brightness values and the resulting projected intensity is extracted from measurements taken with a calibrated silicon photodiode as shown in Section 4.2.1. We assume, to start, a Jacobs-type chemical model. In this model, regions which receive more than a critical threshold dose form solid, crosslinked material while those with less than the critical dose remain uncrosslinked and are later developed away. A future implementation will directly solve the photopolymerization rate equations of Chapter 2 integrated over time and space to generate the degree of crosslinking in the forward model.

2) *Thresholding:* Depending on the development recipe, convert the degree of crosslinking to the thresholded image at the nth iteration $R_n(x, y)$. We have experimented with variations of this procedure, to prevent the optimization from being sensitive to a single threshold, and instead have attempted to penalize absolute errors around the threshold as well. In all cases however, $R_n(x, y)$ lies between 0 and 1, representing material fully washed away as opposed to fully present.

3) *Error:* the error in the image is determined by comparing with the target: $\delta_n(x, y) = R_n(x, y) - R(x, y)$. This is transformed into the backprojection domain by performing a Radon transform (integral projection) at every angle, followed by ramp filtering. This leads to the projection domain error $\delta'_n(x, \theta)$.

4) *Update:* An unconstrained new set of projections is computed as: $R_{n+1}(x, \theta) = R_n(x, \theta) - \delta'_n(x, \theta)$. Finally, the computed projection is constrained to positive 8-bit values by first setting negatives to zero, and then quantizing. It can be confirmed that the updated $R_{n+1}(x, \theta)$ is the closest element in the constrained set to the computed unconstrained value and is therefore a projection.

Figure 4-5 gives an example of a set of both the initial computed integral projections (A, C) and the optimized projections (B, C) for the "thinker" geometry of Figure 4-3A.

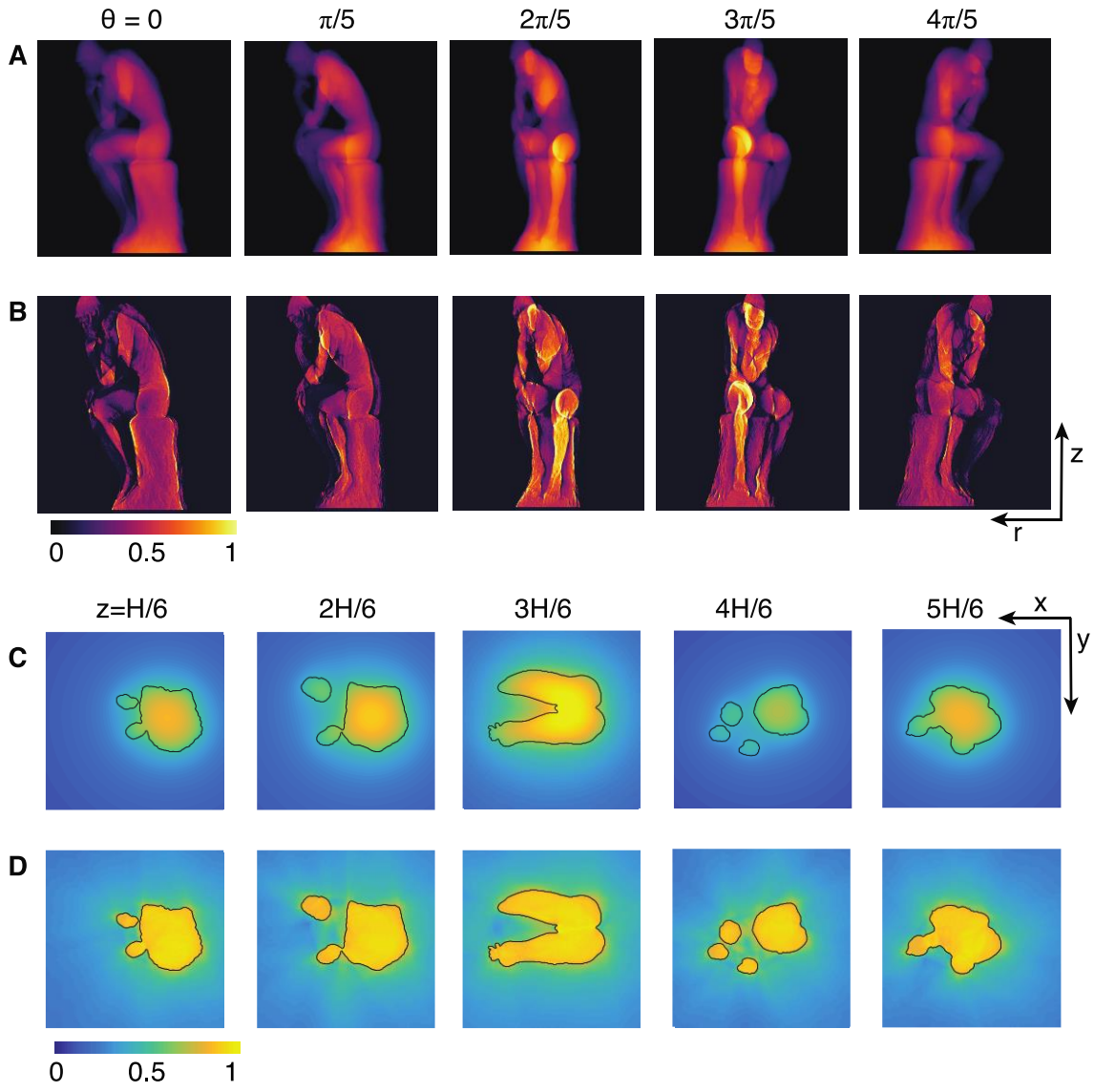

Figure 4-5 (A) Integral projections at example angles. (B) Optimized projections. (C) Cumulative dose from back-projection of integral projection. (D) Optimized cumulative dose.

4.2 System Control and Calibration

4.2.1 Hardware Calibration: Projector

In this Chapter, the projection optics used are an off-the-shelf DLP projector from Optoma, unless otherwise noted (a second CAL prototype system was constructed and used for printing of hydrogels). The model used is Optoma ML570. This projector system follows the WXGA resolution standard with a pixel count of 1280 × 800. The projector was programmed using 8-bit numerical values to control intensity independently in each pixel and in each color channel. Control data was

delivered through an 800 × 1280 × 3 matrix in MATLAB programmed through the Psychtoolbox add-on. In order to directly program intensity values pixel-by-pixel, intensity calibration measurements were recorded to map bit value to output intensity. The measured intensity vs. bit value was calibrated using a silicon photodiode from Thorlabs (Part number s120VC). These measured values are shown in Figure 4-6.

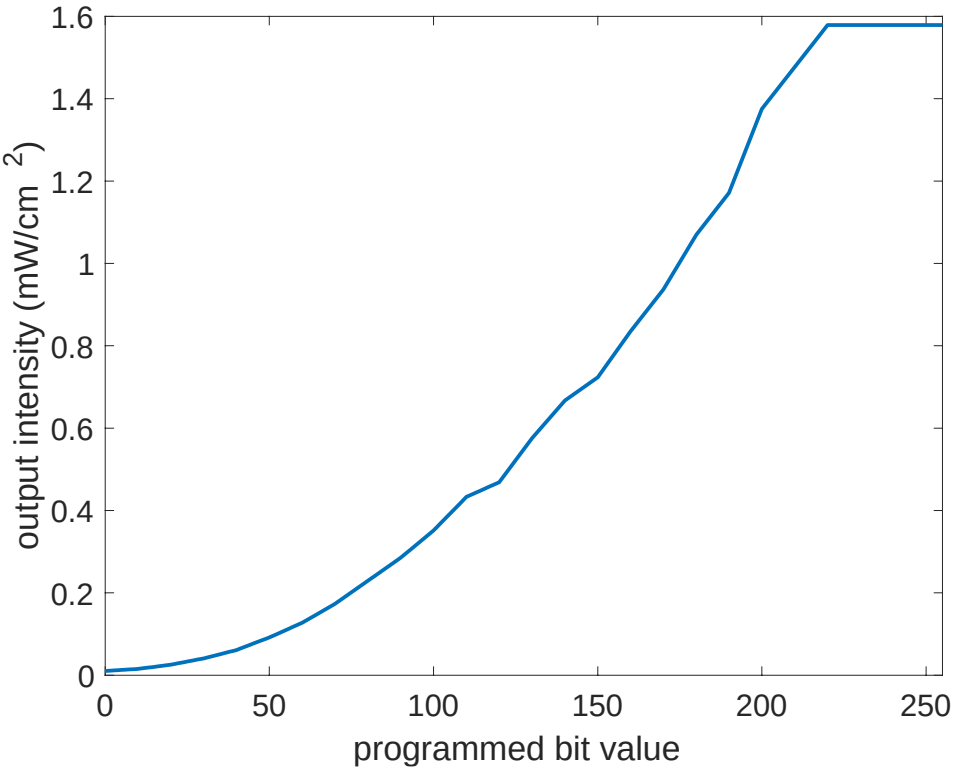

Figure 4-6 Measured intensity vs. bit value input for Optoma projector source.

4.2.2 CAL Resin Formulation

The base materials used for printing via CAL in this thesis were formulated from commercially available acrylate photopolymers and photoinitiators. As in Chapter 3, low values of absorption coefficient α are enabled by judicious selection of the photoinitiator molecule based on its molar absorptivity in the illuminating wavelength band and tuning of its concentration.

The "standard" CAL resin used in this thesis (unless noted otherwise) is a mixture of two acrylate polymer components, each obtained from Sigma Aldrich. Bisphenol A glycerolate (1 glycerol/phenol) diacrylate (BPAGDA) was mixed at 75:25 wt% with poly(ethylene glycol) diacrylate (PEGDA) (average M_n = 250 g/mol). The viscosity of this polymer mixture was measured via cone-and-plate rheometry to have a value of ~5000 cP. A type 2 photoinitiating system consisting of the photoinitiator camphorquinone (CQ) and co-initiator ethyl 4-dimethylaminobenzoate (EDAB) were added to the polymer formulation at 1:1 ratio

by weight. The molar concentration of CQ in the resin formulation was 5.2 mM, selected to achieve an appropriate absorptivity of the resin. CQ and EDAB were also obtained from Sigma Aldrich. A broader range of materials have also been used including photoinitiators phenylbis(2,4,6-trimethylbenzoyl)phosphine oxide (Sigma Aldrich), bis(η5-2,4-cylcopentadien-1-yl)-bis(2,6-difluoro-3-(1H-pyrrol-1-yl)-phenyl) titanium (Irgacure 784, BASF) and the polymer pentaerythritol tetraacrylate (PETA) as well as the hydrogel materials described specifically in Section 4.6.

4.2.3 2D Resin Calibration

A series of calibration tests were performed on the BPGDA/PEGDA/CQ/EDAB resin formulation. As a result of this resin being highly viscous (~5000 cP) and feature sizes being large (> 300 μm), the computational model presented in Chapter 2 predicts that diffusion lengths will be long and that the onset of curing (defined by the oxygen inhibition time) can be assumed to depend linearly on net recorded energy dose. The tests presented in this section serve to validate that assumption over the range of intensity values used. In this test, material-curing behavior was monitored over a range of incident intensity output values and exposure times. A resin calibration system was constructed to allow for rapid testing of a range of parameter values. This system is shown in Figure 4-7A. The projection system was re-oriented to align the optical propagation axis vertically. A thin layer of the resin material was placed on a glass substrate and covered with a silicone layer to prevent adhesion of the cured resin to the top layer. An additional glass layer was used to provide rigidity to the top layer. Glass microscope slides were used as spacers to set the material layer thickness to 300 μm. Images patterned in two dimensions were delivered to the resin material layer.

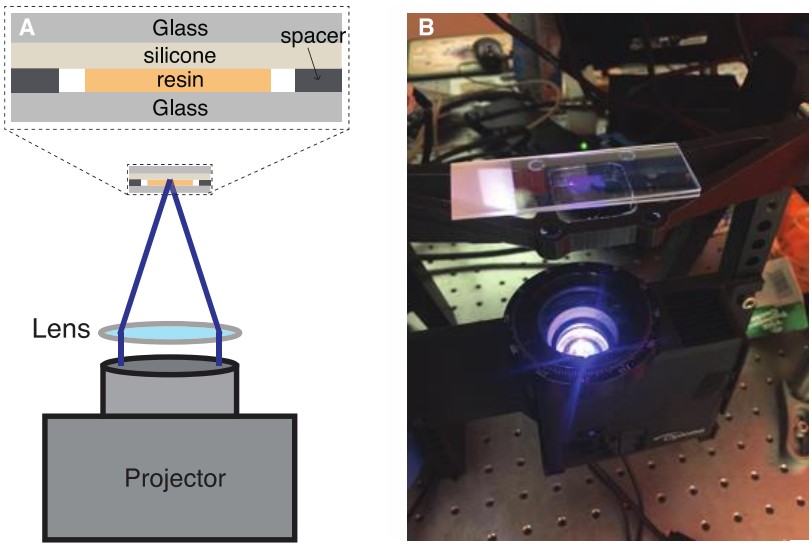

Figure 4-7 Resin calibration system configuration. A) System schematic. B) Image of physical system.

An array of square geometries was used for each projected frame as shown in Figure 4-8A. As time progressed, columns of square features were removed from the projected image so as to deliver a two-dimensional grid of intensity and exposure time values to the resin material. Upon completion of exposure, the top silicone and glass layers were removed and the bottom glass substrate with patterned structures was rinsed in isopropyl alcohol (IPA) to remove uncured resin material. An example image of a rinsed glass substrate is shown in Figure 4-8B.

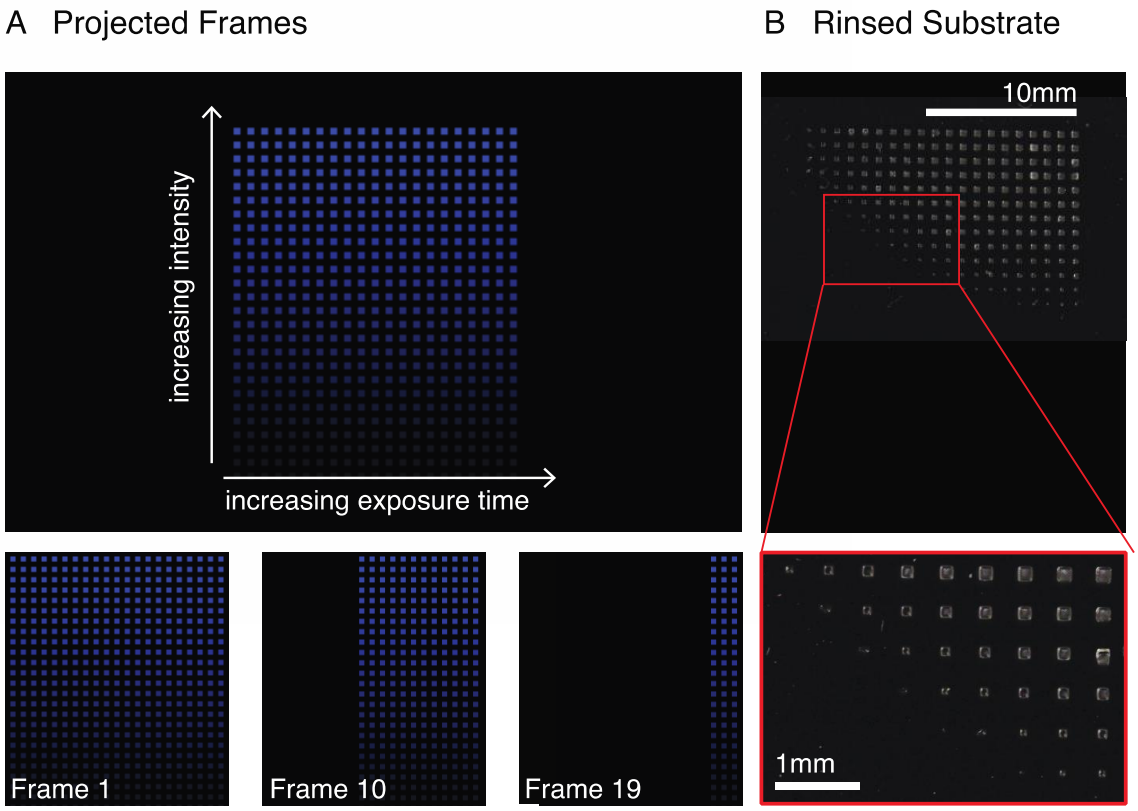

Figure 4-8 2D dose matrix test principle and observed results. (A) Frames projected from the DLP projector. The first frame contains a series of vertical columns of square features. Each subsequent frame removes one column of square features. (B) Image of rinsed glass slide with printed features.

In each experiment, for each row in the two-dimensional grid (corresponding to a distinct value of illumination intensity), a minimum exposure time required for material formation was extracted. This value was selected as the exposure time for the first (lowest exposure time) column where a cured structure exists in the row. Data was compiled from a set of intensity-exposure time grids with ranging critical exposure time values. The resulting critical exposure values are plotted in Figure 4-9. These data agree with the expectation that the oxygen inhibition time varies linearly with incident intensity. Further analysis is presented in Section 4.2.5 after 3D experiments are discussed.

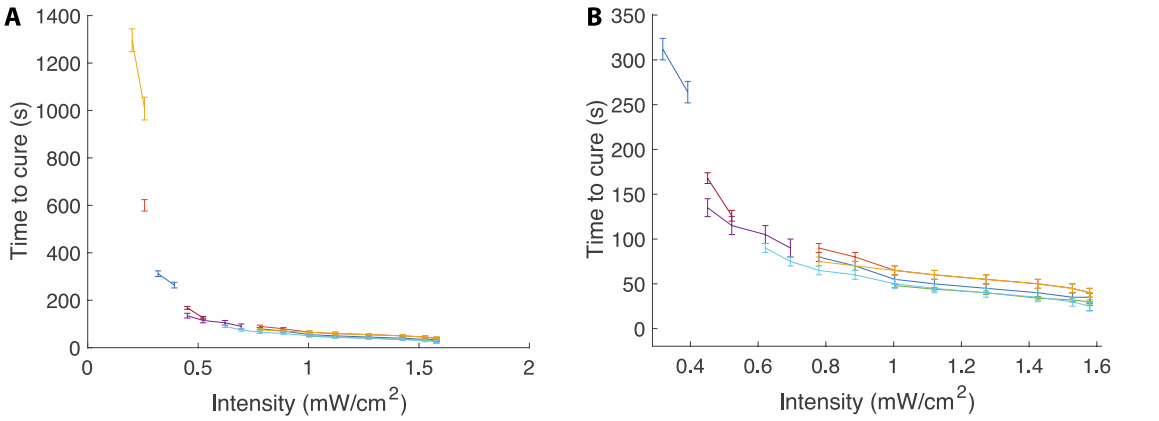

Figure 4-9 2D dose test results from all trials. Extracted time to cure is plotted against illumination intensity. (B) is zoomed in on the data from (A). Each color represents a separate trial.

4.2.4 3D Resin Calibration

To further validate the behavior of the resin in three-dimensions, a second set of experiments was performed. The 3D CAL system hardware of Figure 4-10C was used. A static image, shown in Figure 4-10A, was projected toward the material volume as the volume rotated. The projected image consisted of a vertical array of circular patterns, each with a different programmed value of intensity. A video of the material volume curing was taken through a side window of the apparatus as shown in Figure 4-10B. Each circular image generates a structure on the central axis of the build volume. By monitoring formation of these structures, the exposure time required for the onset of curing, or inhibition time t_{inhb}, was extracted through image processing on the video frames. Figure 4-11 shows the reciprocal of t_{inhb}, or average rate of inhibitor consumption during the inhibition phase, plotted versus incident intensity in each circular image for both 2D and 3D experiments.

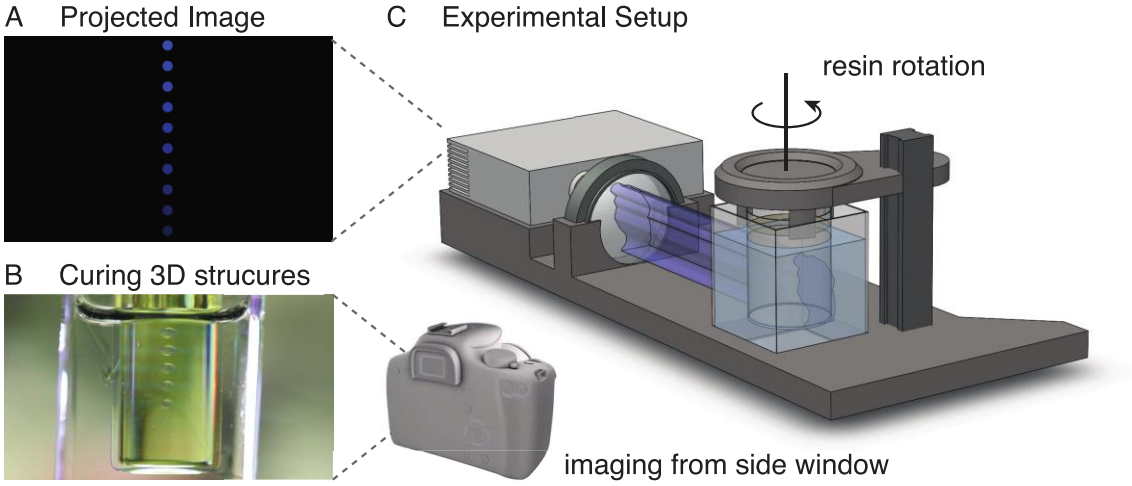

Figure 4-10 3D resin validation experiment setup. Curing 3D structures in (B) are produced from a static image in (A) and rotation of the resin volume through the experimental configuration in (C).

4.2.5 Resin Calibration Results

The results of both 2D and 3D experiments, shown in Figure 4-11, follow a reasonably linear trend for the range of intensities used for curing, albeit with a small implied threshold intensity of ~0.2 mW/cm^2 (in the 3D experiment). This threshold can likely be attributed to the diffusion of oxygen to the center of the vial from its less-exposed periphery, replenishing the inhibiting species effectively indefinitely at extremely low intensities. In any case, these findings approximately validate the assumption of linear recording of exposure dose in the projection computation. Linear regression was performed on 3D data averaged from four trials (three trials for the highest intensity) to produce a best-fit line with $R^2 = 0.9874$, plotted in red in Figure 4-11.

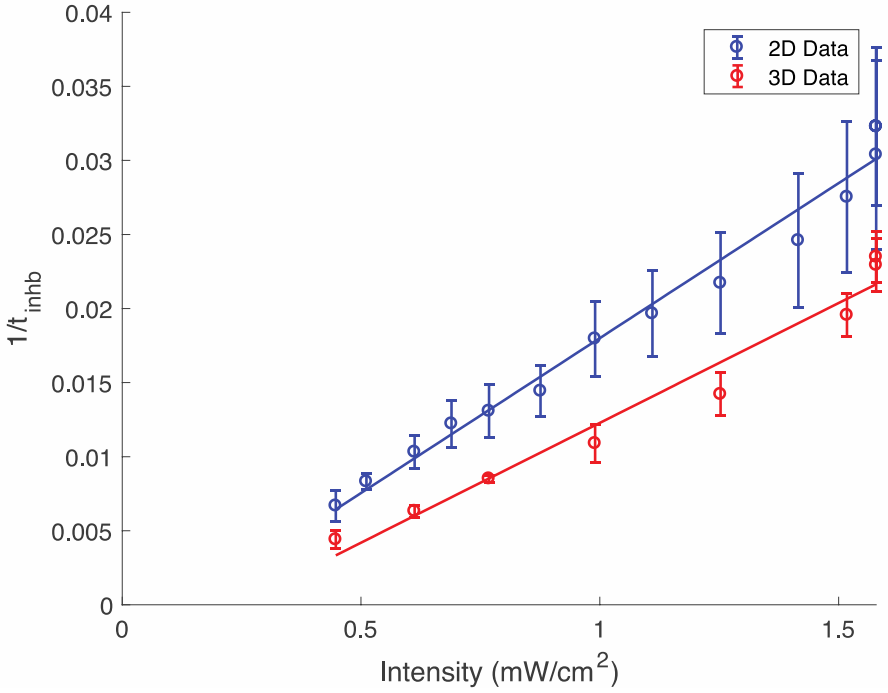

Figure 4-11 Resin response validation. For a range of intensities used from ~0.4–1.6 mW/cm^2, measured inhibition times support the assumption of linear recording of energy dose for both 2D and 3D experiments. The 3D data included are recorded from N=4 trials. Error bars are ± one sample standard deviation.

4.3 2D Hardware Emulation

As an incremental step before applying the optical design algorithm toward 3D CAL printing, a physical validation of the algorithm was performed. For this validation, an experimental apparatus, similar to that used for 2D resin response validation in Figure 4-7, was constructed as depicted in Figure 4-12A. The same DLP projector was used as the optical source to generate the projections and the system was configured such that again a 2D image was incident on a thin layer of resin. In

this system, the resin was left uncovered for ease in removal of uncured material The video output from the projector was set to match the time-evolving intensity map which would be incident upon a cross-section of the 3D volume in the 3D CAL system. Thus, each video frame corresponded to a 1D projection propagated in a single direction dictated by angle of illumination from the algorithm as depicted in Figure 4-12B. As designed by the algorithm, the sum of all video frames gives an image that approximates the target geometry. An example is shown in Figure 4-12C.

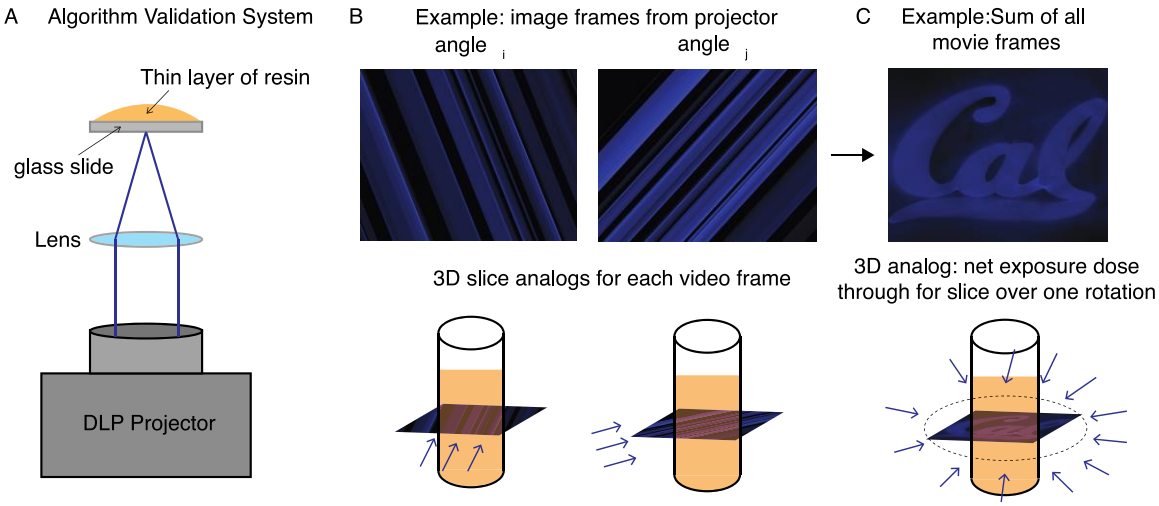

Figure 4-12 (A) Physical system used to validate optical design algorithm. (B) Example movie frames from projected video and representation of analogy to 3D system. Each frame corresponds to the dose passing through the resin from a particular angle $\boldsymbol{\theta}$. (C) Example sum of movie frames from all angles. This dosage distribution is analogous to the net exposure dose seen by a horizontal slice of the 3D volume over one rotation.

The algorithm was tested for a range of geometries. Projections from 500 evenly spaced angles about 360° were computed and used to generate the video frames. The frame rate of the projected movie was set to simulate an angular rotation of 25°/s to match the max rotational speed of the rotating stage used in the 3D CAL system. This setup yielded useful results to validate the algorithm. A set of example prints are shown in Figure 4-13. The four prints shown represent a diverse set of geometries including sharp edges, voids within structures, and smooth, curving geometries.

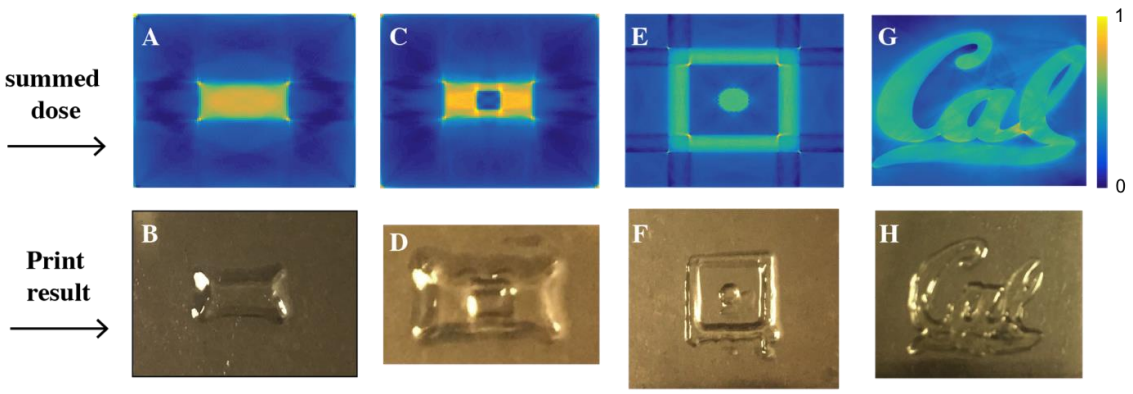

Figure 4-13 Hardware emulation results. For four geometries, the summed dose from all angles and the corresponding print results are shown. (A-B) a geometry with sharp edges. (C-D) a geometry with a void inside of a solid object. (E-F) a geometry with a solid piece inside another solid piece. (G-H) a complex geometry with curved features.

The oxygen inhibition threshold and material response nonlinearity are evident in comparison of the summed dose with the printed result as regions which receive below the critical dose are not printed and are removed in the rinse step. Figure 4-14 shows examples of prints where excess dose is delivered and regions outside of the target geometry are printed (A, C) as well as a print where insufficient dose is delivered and regions within the target are unformed (B, D).

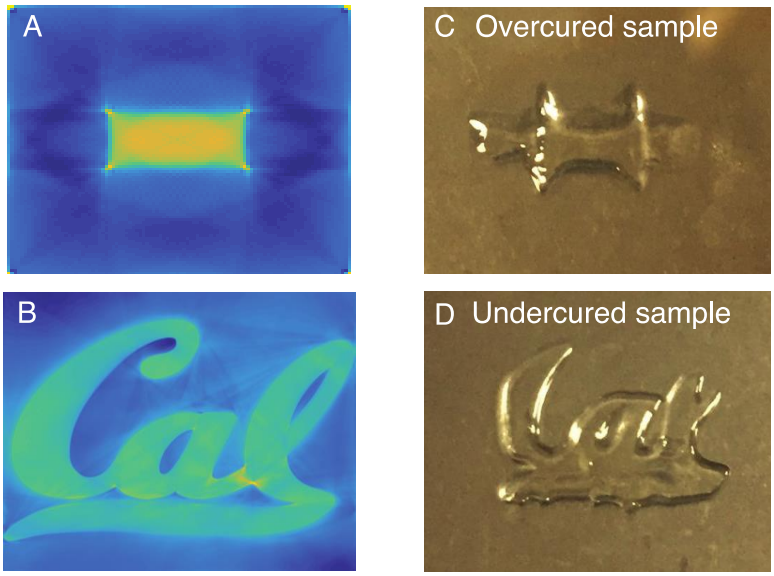

Figure 4-14 Examples of poor results from the hardware emulation. (A-B) Summed dose distribution based on target geometry. (C) An example of an overexposed, and thus overcured sample. Regions outside of the target geometry have formed. D) Example of an underexposed, and thus undercured sample. Some regions within the target geometry have yet to form.

4.4 3D Printing

With validation of the CAL algorithm in two dimensions, the next step in the process of demonstrating the viability of the CAL concept was to apply the computed projections to the 3D exposure and rotation hardware. This section presents the achievement of three-dimensional prints by CAL. The final result, printing of custom three-dimensional geometries, is illustrated in Figure 4-15 along with a view into the build process. The remaining incremental steps to achieve fully three-dimensional prints are described in this section, followed by presentation of a series of printed geometries and the fabrication advantages that they highlight.

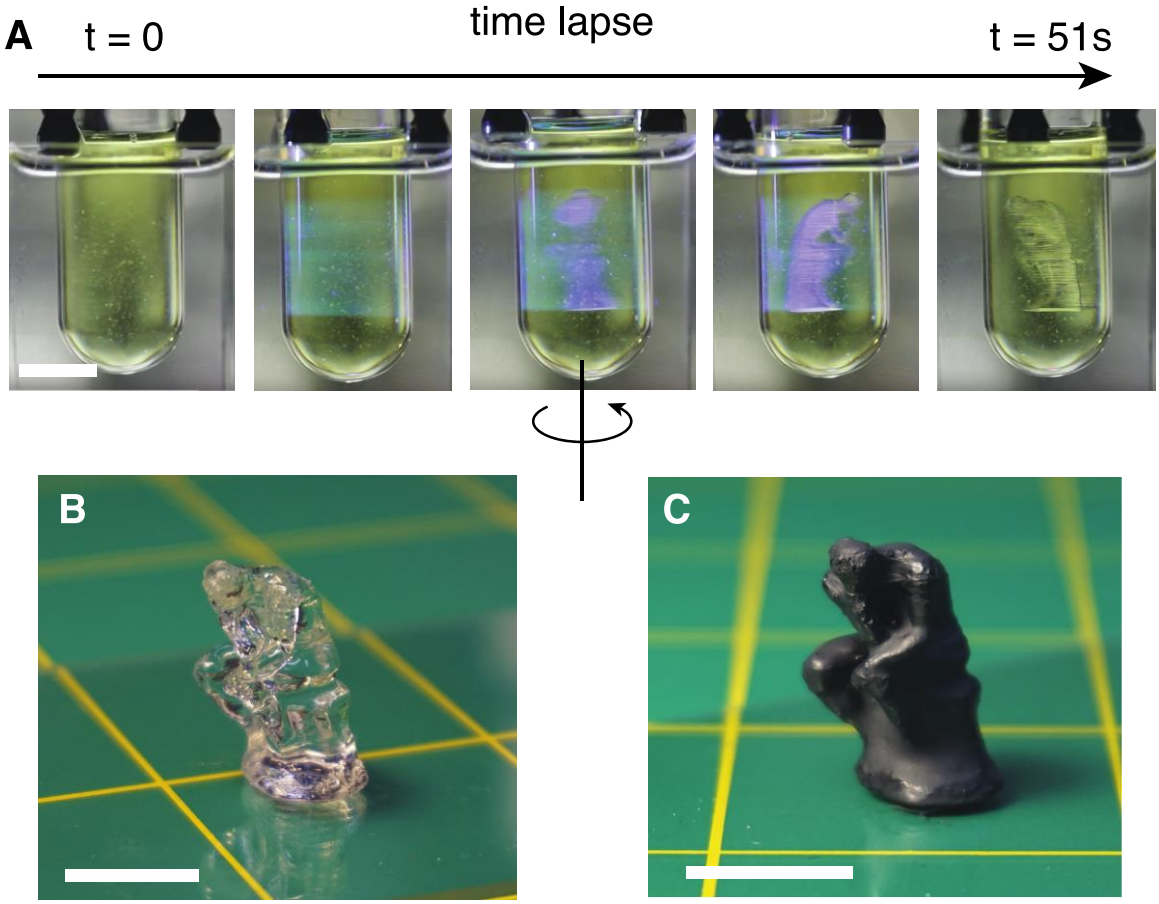

Figure 4-15 Print demonstration of "The Thinker" geometry. (A) A view into the print process. Material forms throughout the geometry together, rather than in layers. (B) The part shown in (A) after rinsing away uncured material. (C) The part from (B) painted for clarity. Scale bars: 1cm. Grid lines: 1 inch.

4.4.1 Constant Cross-Section

The first demonstration of 3D printing via CAL is a logical incremental advance from the 2D hardware emulation. As a first example, parts with uniform vertical cross-section were printed. In these parts, the algorithmic design of the

projections for each vertical slice is the same, making the computation simpler and faster. These results are shown in Figure 4-16. The first geometry, a rectangular prism, demonstrates the potential of CAL to print 3D geometries with abrupt corners. Another geometry, with a semicircle cross-section, demonstrates the ability to simultaneously print curved surfaces, flat surfaces, and corners. Most importantly, successful printing of a hollow cylinder demonstrates the ability to print voids within a solid structure.

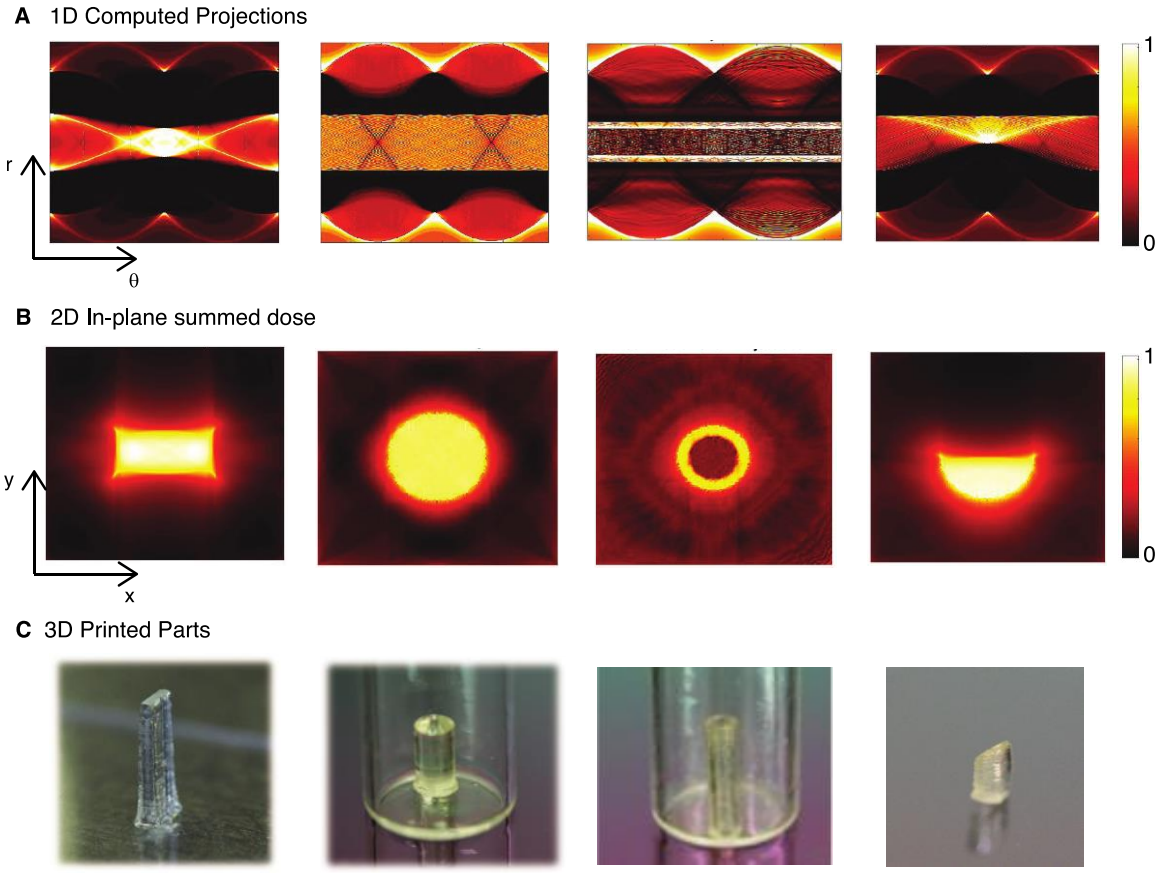

Figure 4-16 3D CAL-printed results with constant cross-section in *z*. Column 1: 1D projections vs. angle for each *z* slice. Column 2: summed intensity distribution from all projections in each *z* slice. Column 3: Images of 3D printed results.

4.4.2 Geometry: Hollow Ball

To generate geometries with increased complexity, 1D projections can be computed separately for each vertical slice of the 3D geometry. **Figure 4-17** gives an example of a geometry where the cross-sectional target varies within the structure. Here, each cross-section manifests as a circular geometry with varying radius through the vertical *z*-coordinate. A fully three-dimensional geometry is demonstrated which again highlights the ability to print a void within an enclosed structure. Here, a hollow sphere is printed and uncured resin in drained though a hole in the bottom. Figure 4-17C shows the same geometry printed in Penta-

erythritol tetra-acrylate (PETA) polymer. This print nicely suggests the ability of CAL to print smooth, layerless geometries.

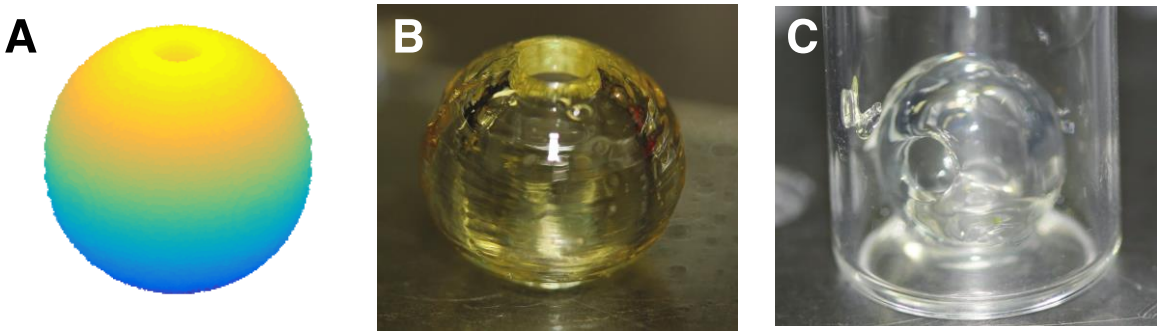

Figure 4-17 (A) Target geometry with varying cross-section through the vertical (*z*) coordinate. Fully 3D parts with internal voids are shown printed in (B) BPAGDA/PEGDA and (C) PETA polymers.

4.4.3 Geometry: Smooth Sphere

The layerless printing capabilities of CAL are better illustrated in the image of a printed solid sphere geometry in Figure 4-18. This image demonstrates a printed part with visibly smooth surface finish. The ability to eliminate layer lines and print with smooth finish could enable custom optical components to be printed more readily. Note that this geometry was printed in a gelatin methacrylate hydrogel material (described in more detail in Section 4.6) rather than the standard BPAGDA/PEGDA resin.

Figure 4-18 Smooth sphere printed in gelatin methacrylate with no layer lines.

4.4.4 Geometry: Ball-in-a-Cage

In stark contrast to layer-based AM methods, CAL requires no support structures even when printing re-entrant and overhanging features or disconnected parts. This capability is achieved through rapid fabrication of the entire geometry concurrently. Figure 4-19 gives an example of a geometry that would require support structures in a layered process. This geometry consists of a ball disconnected to a surrounding cage. Printing of this geometry in any orientation in a layered process would require the use of sacrificial support structures to connect the inner ball with the outer cage. In the CAL process, both pieces form at once and no connecting structure is required.

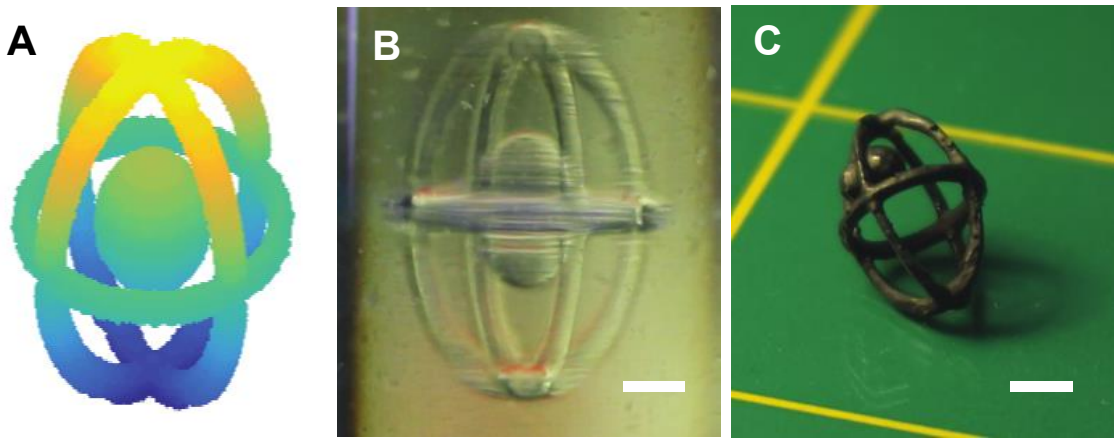

Figure 4-19 Ball-in-a-cage print. (A) The target 3D geometry. (B) Image of the formed geometry inside the resin vial with no support structures. (C) The printed part after being rinsed, removed, and painted.

4.4.5 Geometry: Dental Model

Currently, the dental industry fuels some of the most widespread use cases of 3D printing. Patient-specific dental models must have geometries customized to each individual patient. The customization requirement lends itself naturally to additive manufacturing. Today, AM is used in the production of crowns, night guards, surgical guides, and various other dental devices. Stereolithography and DLP photopolymerization specifically are widely used in the production of patient-specific molds for casting of clear orthodontics. Figure 4-20 demonstrates the ability of CAL to fabricate such custom, patient-specific, orthodontic models.

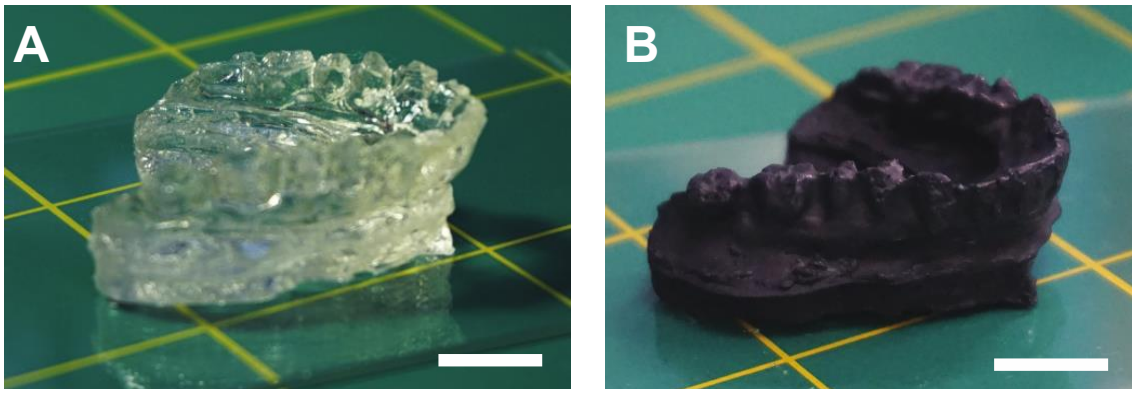

Figure 4-20 Dental model print. (A) Geometry directly after rinsing and removing. (B) The same part painted for clarity.

4.4.6 Additional 3D Results

The printed results shown in this chapter serve to demonstrate the geometric versatility of the CAL technique. A series of additional geometries have also been printed using the CAL process. Figure 4-21 displays an octet truss lattice geometry that can be used to achieve materials with high strength-to-weight ratio (*87*). Figure 4-22 shows additional geometries that further illustrate the geometric freedom.

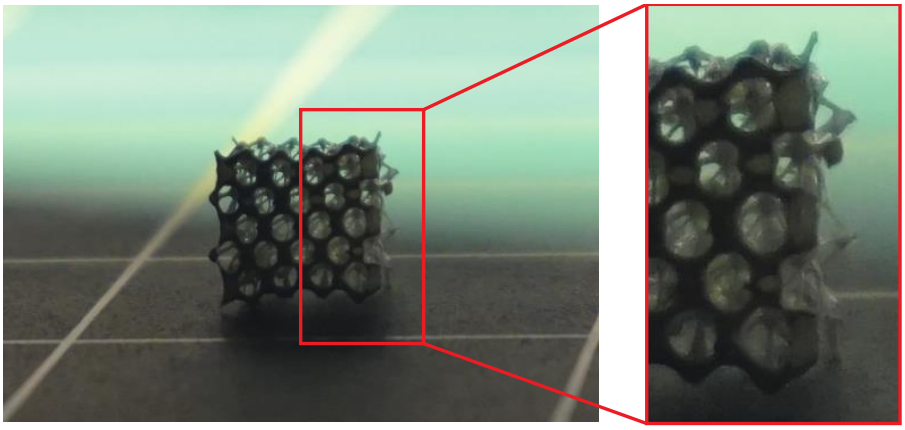

Figure 4-21 Octet truss print. A demonstration of an octet truss lattice geometry printed by CAL. Grid lines are 1 inch.

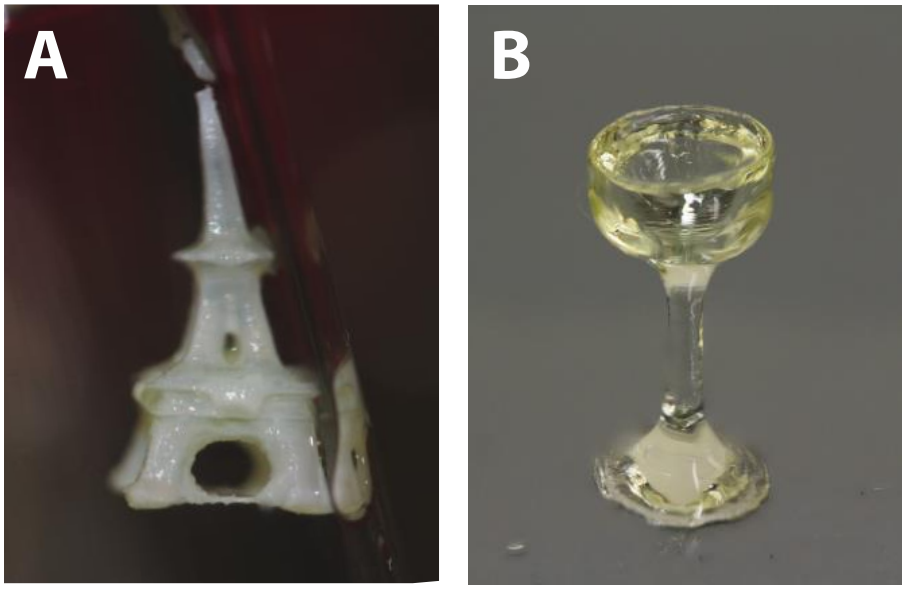

Figure 4-22 Additional parts printed by CAL. (A) An Eiffel Tower geometry and (B) a wine glass.

4.5 Overprinting

The preceding Section 4.4 demonstrates the geometric versatility of CAL as well as some of the fabrication advantages that come with the ability to synthesize arbitrary geometries volumetrically. In addition to aforementioned benefits, volumetric fabrication offers an exciting route toward an entirely new capability in AM. Through superposition of exposures from many angles, the CAL process also enables the capability to pattern complex 3D geometries directly onto pre-existing 3D substrates. The substrate or pre-existing part/assembly can be manufactured by CAL or by an entirely different process or processes. In Figure 4-23, an example is shown of this ability to synthesize a custom geometry onto an existing mass-manufactured part. In this demonstration, a polymer handle is printed directly onto a metal screwdriver shaft. In the demonstration, which is currently at a smaller scale than the standard dimensions of a screwdriver, a needle is used in place of the shaft. The metal needle was fixtured within the print volume, rotating with the resin, and the CAL process was used to print the external structure directly onto it as displayed in Figure 4-23A. A similar capability is widely utilized in high-volume production by the techniques of over***molding*** and insert molding. However, to date, there is currently no equivalent technique available in AM. The process of "over***printing***" enabled by CAL could provide this missing capability.

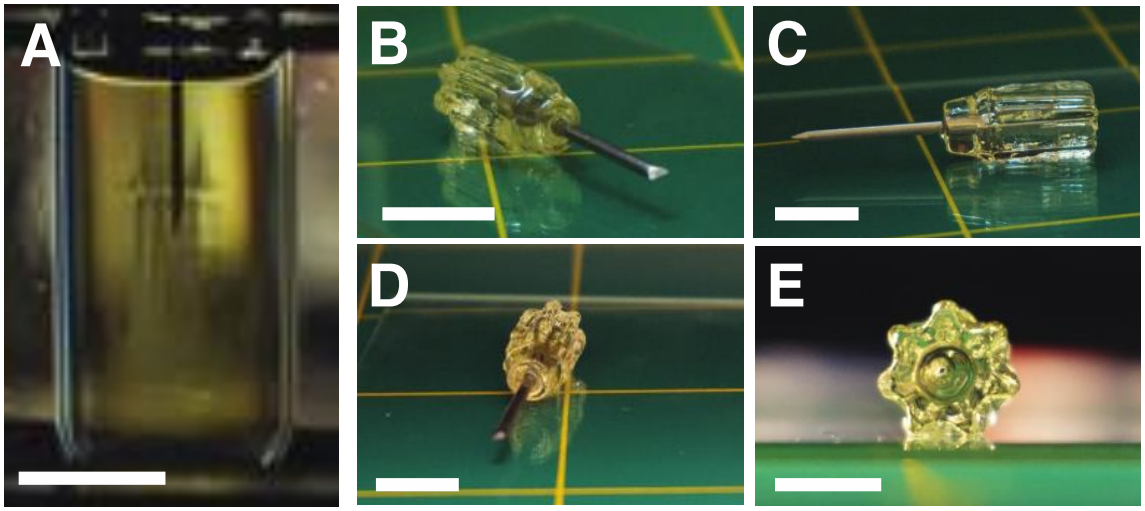

Figure 4-23 Overprinted screwdriver. (A) The screwdriver printed directly onto the needle base within the print volume. (B)-(E) images of the overprinted screwdriver after uncured material has been rinsed. Scale bars are 1cm. Grid lines are 1 in.

For more complex starting substrates, the CAL algorithm should be updated to account for occlusions within the volume. This adds computation steps in modeling occlusions and/or reflections. CAL does, however, provide a direct path toward printing of arbitrary geometries onto substrates with convex cross-section. The Radon transform possesses a 180° shift symmetry that allows for printing with exposure from the half space of angles as demonstrated in Figure 4-24A even when individual projections are occluded as shown in Figure 4-24B.

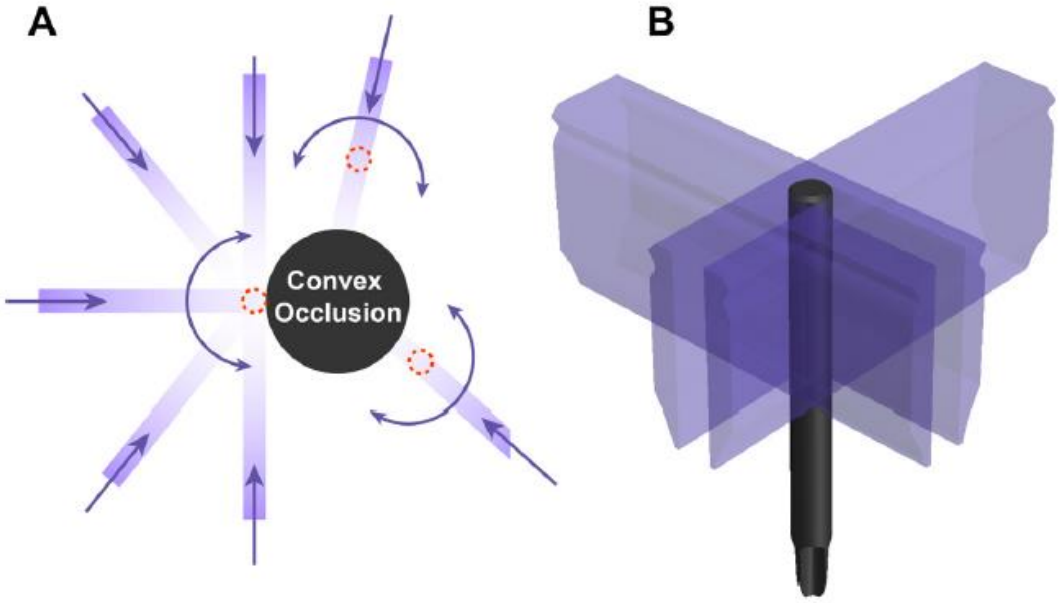

Figure 4-24 (A) By having access from angles from 0° to 180°, arbitrary geometries can be printed on to convex occlusions/substrates. (B) Individual 2D projections are occluded by the immersed object but external geometries can still be printed.

This over-printing process could be used in the future to, for example, encapsulate electronics, improve mechanical properties of orthodontics, or in

general fabricate a customized exterior for an object with a mass-produced skeleton. A second simple example that has been demonstrated is shown in Figure 4-25 where a rose flower geometry is printed onto a stem. In this demonstration the stem is a piece of red metal wire.

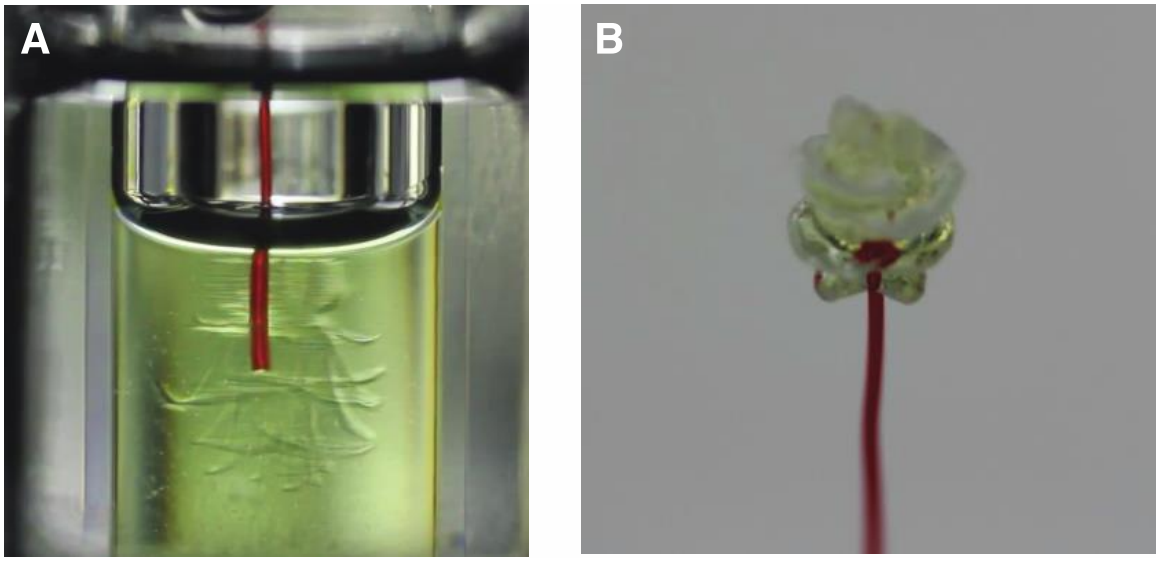

Figure 4-25 Overprinted rose geometry. A rose is printed onto a metal wire stem. Images are shown of the printed rose (A) in the print volume and (B) after solvent rinsing.

4.6 Hydrogel Printing

The unique system architecture employed in the volumetric fabrication process also offers advantages in the types of materials that can be printed and thus the application areas that it can address. CAL can be particularly advantageous when the converted material is of low stiffness, for example in the ~1–10 kPa regime needed for many soft tissue modeling and bioprinting applications (*7*,*88*–*90*). Figure 4-26 and Figure 4-27 demonstrate the application of CAL to patterning of a gelatin methacrylate (GelMA) hydrogel material. This material would present difficulty in printing with a serial vat photopolymerization process due to forces exerted on the soft part during the build. These forces can arise from the hydrodynamic forces induced by resin flow into the build area as well as gravity. The compliance of this material is evident from the ease in deformation from squeezing in Figure 4-26 and under gravity in Figure 4-27.

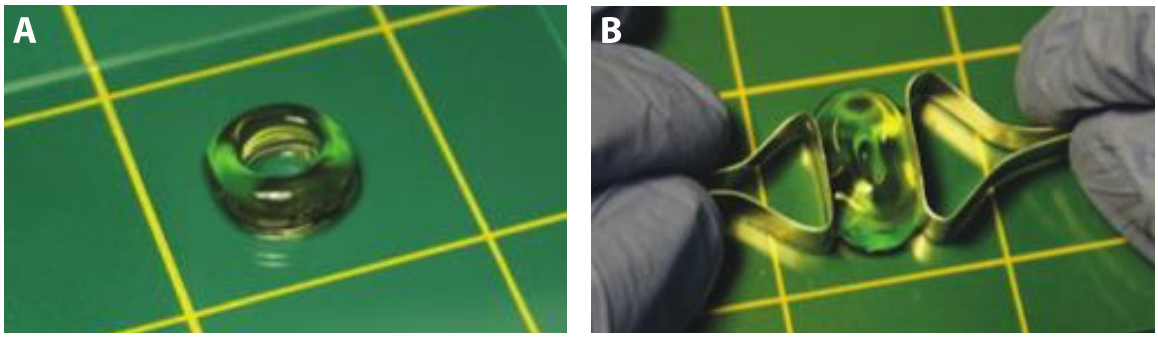

Figure 4-26 (A) A donut shaped or toroid geometry printed in gelatin methacrylate. (B) A demonstration of the compliance of the printed geometry as it is easily squished by hand from the sides.

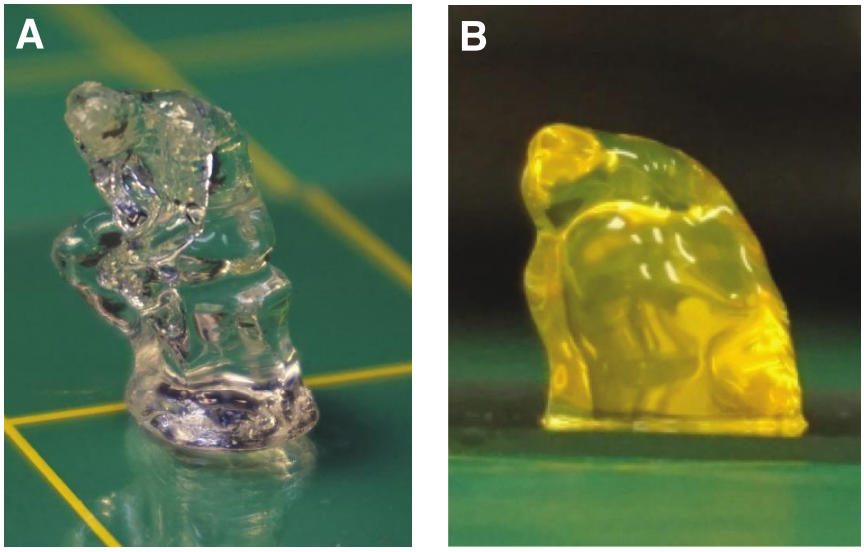

Figure 4-27 When printed in the gelatin methacrylate hydrogel, the thinker geometry immediately deforms under its own weight. This is evident from the comparison of the GelMA structure in (B) compared to the BPAGDA/PEGDA structure in (A).

The gelatin methacrylate hydrogel used was obtained from Advanced Biomatrix (San Diego, CA). The polymer is mixed at 10% by weight in an aqueous solution. A different photoinitiator system was used for hydrogel printing because CQ has poor solubility in water. The photoinitiator used for hydrogel printing was a two-part visible light initiator consisting of ruthenium (Ru) and sodium persulfate (SPS) (*91*). Ru and SPS were mixed at concentrations of 2 mM and 20 mM respectively into the gelatin methacrylate hydrogel. The green color channel of the projector was used for GelMA hydrogel samples because the absorbance of ruthenium in the blue part of the spectrum was too high. When the blue channel was used, the required concentration of Ru for reasonable absorbance values was too low to overcome oxygen inhibition. Absorption spectra for both BPAGDA/PEGDA and GelMA materials are given in Figure 4-28. Hydrogel samples were cooled in a commercial refrigerator to ~5° C to form a gel before photocrosslinking.

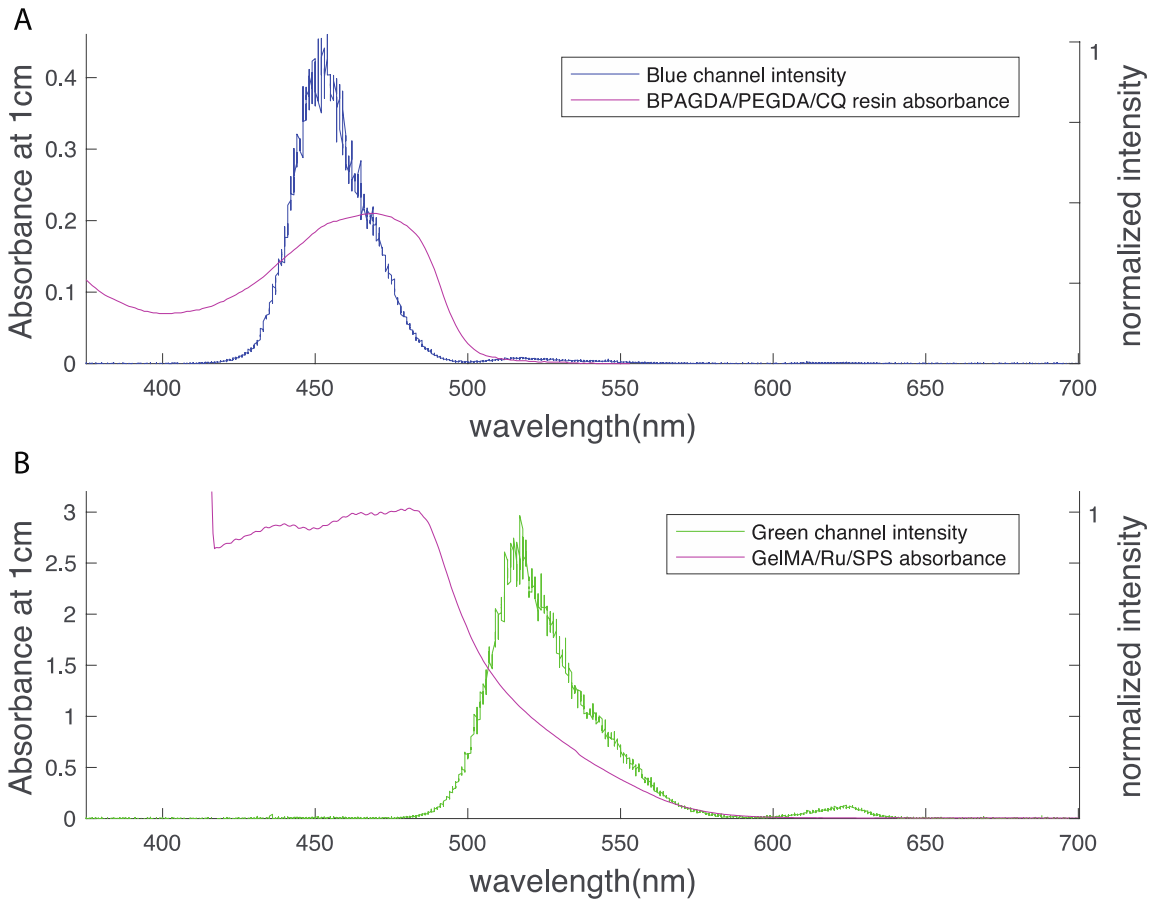

Figure 4-28 Resin absorbance spectra for (A) BPAGDA/PEGDA resin and (B) GelMA hydrogel, and corresponding illumination spectra for (A) blue color channel and (B) green color channel. Reported absorbances are for a penetration distance of 10 mm.

Chapter 5 Conclusions and Future Work

The invention of Computed Axial Lithography represents a new avenue in additive manufacturing. A new paradigm of volumetric fabrication of complex geometries enables rethinking of the way parts are designed and manufacturing is carried out. Looking forward, this naturally fosters potential for innovation in system and materials development. CAL can serve as a baseline for development of new technologies that leverage its core principles.

5.1 Capabilities Comparison

As discussed in Chapter 4, CAL in its current embodiment already brings a slew of fabrication advantages compared to incumbent AM processes. This section takes a slightly closer look at how CAL and volumetric fabrication compare to existing technologies in each of the ASTM process categories. Figure 5-1 presents a qualitative representation of performance of technologies in each ASTM category across a range of quality metrics based on geometry, process, materials, and final parts. While no AM process is perfectly suited to all fabrication needs and each will likely have areas where it excels above others, we believe that CAL performs well when considering a broad range of quality metrics simultaneously. It should be noted that the areas considered are motivated by requirements and challenges of existing AM processes and are selected independent of the developments in this thesis. The core advantages of CAL and volumetric fabrication have already been directly presented in Chapter 4.

		Vat Photopolymerization	Powder Bed Fusion	Binder Jetting	Material Jetting	Sheet Lamination	Material Extrusion	Directed Energy Deposition	CAL
Geometry	Overhang constraint								
	Bridge constraint								
	Interlocking joints								
Process	Support removal								
	Thermal management								
	Heterogeneous substrates								
Materials	High strength								
	soft/rubbery								
	Multimaterial								
Parts	Surface Finish								
	Porosity								
	Isotropy								

Figure 5-1 Qualitative comparison of various performance metrics and capabilities for polymer AM processes. Green corresponds to strong capability of the technology subgroup in the particular

metric of consideration, yellow corresponds to average or mediocre, and red corresponds to poor. Color selection is justified in Section 5.1.

5.1.1 Geometry

As touched upon in Chapter 4, volumetric fabrication brings distinct advantages compared to layered methods with regards to final part geometry. The ability to print disconnected parts in a single build was already discussed in Section 4.4.4. This capability can help to facilitate printing of interlocking joint structures that can be difficult, impossible, or require support structures on most other AM processes. In addition to printing disconnected geometries, CAL can also readily get around overhang and bridge considerations which are prevalent across other process physics (*92*).

5.1.2 Process

CAL also presents some advantages compared to other categories when considering the printing process. For example, as highlighted in Figure 5-1, processes which rely on heating of a material for printing tend to require some degree of thermal management during the print. Similarly, many processes rely on some form of in situ feedback during print to prevent failure or improve print quality (*93*). The inclusion of support material removal as part of the printing process can also affect the overall quality and ease of use of the process.

5.1.3 Materials

A wide variety of materials can be currently be used in AM processes (*94*) and many AM processes are aimed specifically at enabling printing of better or different materials. We have already discussed the unique ability of volumetric fabrication to print soft materials. The ability of CAL to print new materials through viscous resins will be discussed in Sections 5.2.1 and 5.2.2. We believe that CAL can readily compete on materials with existing vat photopolymerization technologies as well as enable distinct materials advantages compared to all techniques.

5.1.4 Parts

When considering final part quality, independent of materials, we again note that CAL demonstrates the ability to print parts with exceptional finish, offers a route to more isotropic material properties through elimination of layering, and allows for fully dense parts by virtue of the photocrosslinking process.

5.2 Material Development

Computed Axial Lithography brings distinct advantages in photoresin design and development. These advantages are directly enabled by a system architecture that is fundamentally different that that used in pointwise or layerwise vat photopolymerization 3D printing systems based on stereolithography, DLP

projection, or CLIP. In the incumbent vat photopolymerization technologies, a constraint exists limiting the maximum viscosity of the liquid resin used in the system. When using these technologies, the resin viscosity typically must be low enough to enable re-flow of the resin over a previously cured layer. Highly viscous resins flow slowly and limit print speed or even printability of the material. The BPAGDA/PEGDA resin used in Chapter 4 is already beyond the viscosity of resins used in commercial 3D printing systems at ~5000 cP.

5.2.1 Viscous Acrylates

In stereolithography resin formulation, it is often the case that resin oligomer formulations are cut with reactive diluent monomers or other functional polymers in order to decrease the viscosity of the cured liquid precursor. These diluent components serve to improve the processability of the material and allow for flow during the printing process. However, the inclusion of diluent components in a resin formulation tends to have an adverse effect of the final mechanical properties of the cured part. With CAL, resins could be formulated with this major constraint removed, which could enable printing of higher quality materials.

5.2.2 Silicones

Silicone materials currently present some difficulty in 3D printing, in part due to similar considerations on formulation viscosity. Existing 3D printed silicone materials lack the desired properties for a number of applications due to additives suspended in the material for viscosity reduction. CAL could provide a route to printing of pure silicone materials for end-use applications in for example wearable electronics and medical devices (*95*).

5.2.3 Cyanate Esters

Cyanate Esters represent a class of materials that tend to exhibit high thermal resistance at high temperatures as well as a low dielectric constant and high strength. These materials can achieve glass transition temperatures (T_g) as high as 400 ˚C (*96*). They have found application in printed electronics as well as in the aerospace industry for components where high thermal stability is required, including engine parts. Typically, cyanate esters are formed through thermal activation at elevated temperatures. In the presence of reaction catalysts, they can be cured at lower temperatures. There have been various attempts to additively manufacture cyanate ester materials. However, for various reasons, in order to become printable, typically they must be diluted by a secondary chemistry or component. In the case of extrusion-based printing, additives are included to provide the appropriate rheological properties (*28*). In photopolymer methods, the cyanate ester curing reaction is too slow and an acrylate chemistry must be added to give the part its structure during print. CAL could potentially offer a route to direct printing of pure cyanate esters by direct patterning of a metal catalyst

volumetrically within the volume. A thermal post-cure could then be performed on the entire volume to form the structure.

5.2.4 Metal 3D Printing

Recently, interest in additive manufacturing of metals has grown greatly as the ability to reap the benefits of AM in metal materials opens up new applications. Similar to polymer AM, metal parts are still produced by processes which repeat unit printing operations of less than three dimensions. The most common techniques involve Selective laser melting (SLM) and Direct Metal Laser Sintering (DMLS). Both technologies use a laser to fuse metal particles in a powder bed. DMLS follows a process similar to plastic SLS (described in section 1.3.3) while the SLM process fully melts metal particles to join them. Each of these technologies utilizes a scanning laser beam to build parts point-by-point. An electron beam can also be used, as is the case in technologies relying on Electron Beam Melting (EBM). Line-at-once metal 3D printing techniques have emerged recently and generally involve deposition of a polymer binder material into a metal powder bed.

The challenge of applying volumetric printing to metal AM comes from two major directions. For one, metal powders absorb, reflect, and scatter incident light. Second, the power required to melt, metal particles is very high and is thus difficult to achieve over large areas, though progress has been made recently to move metal 3DP toward layer at once fabrication (*97*).

The application of CAL and volumetric fabrication to metal AM is major challenge but could represent an exciting future research direction. It has been shown that stereolithography can be used to produce metal parts by encapsulating metal powder suspensions (*98*) and sintering in a post-processing step. Potentially this could offer a route towards metal additive manufacturing by CAL. In the current embodiment of CAL, sufficient light penetration could potentially be achieved through a combination of low enough metal particle concentration and small build volume. A more effective route could include use of a source that more readily penetrates metal, such as X-Rays.

5.3 Dimensional Scaling

A likely important direction in the future development of CAL is the scaling to larger build volumes. Build volumes on commercial 3D printing systems show some variation in size but typically fall in the range of 100s of mm on a side. The largest parts printed thus far by CAL have a maximum radial dimension of ~30 mm. Scaling to larger sizes in the vertical (z) dimension is relatively straightforward. The challenge in scaling comes in the (x, y) radial plane as moving to larger dimensions requires a larger container and light penetration to greater depths. Following the procedure of Section 3.7.2, the required photoinitiator concentration at larger build volumes can be readily calculated. The dissociation rate will likely be slowed from reduction of the product $\epsilon(\lambda) * [I](x, y, z) * I_s(x, y, z)$ in Equation 2.5 which could adversely affect the final part at some scales. This would arise from the finite optical

contrast limiting the extent of the reaction in volume and could be potentially accounted for by addition of inhibitor molecules to the resin.

5.4 Chemical Modeling

While the photochemical model in Chapter 2 sets the basis for the operating principles of the systems in Chapters 3 and 4, there is still potential to better build in the chemical response of the resin to the projection design algorithm. Currently, the algorithm is designed for patterning in the inhibition phase of polymerization. As a next step, inclusion of propagation, termination, and refractive index change to the projection algorithm could improve the quality, uniformity, and dimensional accuracy of printed parts.

5.5 CAL Hardware Redesign

The current implementation of CAL represents the introduction of a novel additive manufacturing method that ushers in a host of fabrication advantages as described in the previous sections. We, however, consider the current system to be a proof-of-principle for future hardware developments. There are some logical amendments to the prototyped system that we will look to be implement in future work.

5.5.1 Rotating Optics

To start, some improvements can be made through the design of a system where the resin volume is static and the optics rotate around it. The advantage of this system design is that the optics can potentially be rotated at a much higher speed than the volume. This possibility arises from the constraint of fluid motion in the resin volume at higher rotation speeds, which can cause distortions in the printed geometry. The only constraints on the speed with which the optics can be rotated are motor rotation speed limits and the maximum frame rate of the optical system. Neither limit has been nearly approached in the current implementation. A design concept for a rotating optics system is shown in Figure 5-2. Here, both the projection optics and the build volume, or photopolymer vat, remain static. Time multiplexing of projections and delivery from selected angles is achieved by rotation of a mirror assembly.

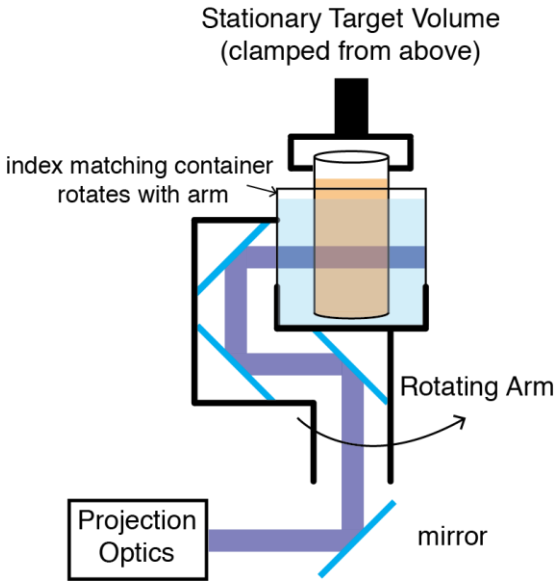

Figure 5-2 A potential future CAL hardware modification. A rotating assembly allows for rotation of the patterned optical images around a static build volume.

5.5.2 Lightfield projection

We are also interested in the prospect of creating a system which eliminates all motion, and which eliminates time-multiplexed projections. In Figure 5-3, a second design concept aimed at single-shot fabrication of 3D geometries is proposed. Such a system would simultaneously project all computed images from all angles. This possible embodiment of a single-shot 3D lithography system is inspired by the Lytro plenoptic camera that images an angular as well as spatially resolved ray space (*99*). Prior work on near-eye lightfield displays also implements a related system (*100*). Here, in order to simultaneously illuminate all angular pixels as well as spatial pixels, we propose to use a microlens array, with subpixels of LEDs, placed at the focal plane under each microlens. The microlens array could wrap around the target volume in a concentric manner as shown in Figure 5-3. The inset shows a single microlens with multiple LED subpixels.

In the tomographic construction procedure, we aim to have both a high spatial and angular resolution. If we consider the illustrated geometry, this allows us to enumerate a tradeoff between angular and spatial resolution. For concrete numbers, let us consider a 10 cm target volume radius and 30 cm outer radius. The spatial pixel shown in the inset is required to project the set of angles from θ_1 to θ_3 given by the overall geometry of the system. Angular sampling consideration suggests that the number of angular samples over 180^o should be a factor of $\pi/2$ higher than the number of spatial samples. This ensures that the angular sampling at the boundaries of the Fourier space is at least equal to the spatial sampling. In this example, if we were to use 500 spatial samples in each transverse dimension, this would lead to 785 angular samples. The angular spacing is then 0.23^o, which leads to 160 angular subpixels under one spatial pixel. With 500 spatial samples spread

across a target region of size 10 cm, this leads to a 200 μm spatial pixel size, with the LED size given by 1.25 μm.

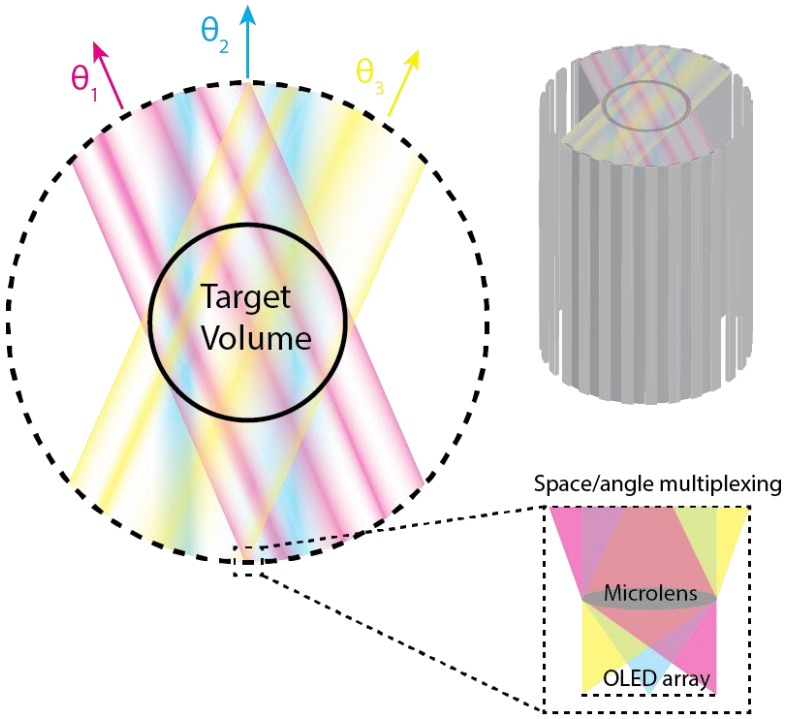

Figure 5-3 A second potential CAL hardware modification. A lightfield projection system composed of LED arrays and microlenses surrounds the static build volume and provides a means for simultaneous delivery of patterned images from all angles.

To generalize slightly and explicitly consider how this implementation will scale, we consider a target radius of r, outer radius of R, minimum subpixel size of λ and N the number of spatial pixels in each dimension. Then, the number of angular samples is $\pi\, {}^{N}/_{2}$leading to an angular sample every $2/N$ radians. Thus, the number of subpixels under one microlens will be $N \tan^{-1}(r/R)$ with the microlens size being r/N. This leads to the subpixel size $\lambda = r/N^2 \tan^{-1} r/R$. Therefore, if we set the spatial resolution, target volume size and minimum subpixel size, we can calculate the required number of samples and outer radius. For instance, in order to print a 5 cm target radius with 100 μm resolution using 10 μm subpixels would require 1000 spatial samples and an outer radius of 10 m. The impractically large outer radius helps to achieve a small angular resolution using a limited subpixel size. This suggests that reducing the number of angular samples while maintaining spatial resolution is going to be an important problem to address for this implementation. The non-linear thresholding properties of a sensitive resin may well be one solution to help achieve accurate reconstruction with sparse angular sampling.

5.6 New System: Roll-to-Roll Nanofabrication

Roll-to-roll nanofabrication represents a somewhat removed area where volumetric printing enabled by CAL could find useful application. Roll-to-roll fabrication describes a process in which a thin material substrate is translated relative to a printing system, often in order to achieve printing over much larger areas than would be achievable without translation of the substrate. In these systems printing can be performed through a number of different mechanisms including imprint (*101–103*) deposition (*104*), or optical patterning (*105*,*106*). This type of manufacturing system is often used for the production of electronic devices. Roll-to-roll processing brings fabrication advantages by enabling high throughput (through fast, large-area patterning) at relatively low costs by producing films on the order of a meter wide and potentially many tens, hundreds, or thousands of meters long with features at the nanoscale.

A variant of CAL could offer a unique path towards high-throughput printing of 3D micro- or nanostructures over such larger areas. Roll-to-roll fabrication is often done on flexible substrates which translate over a roller as depicted in Figure 5-4. The rotating roller could offer a natural route to providing the angular multiplexing in needed in the CAL process.

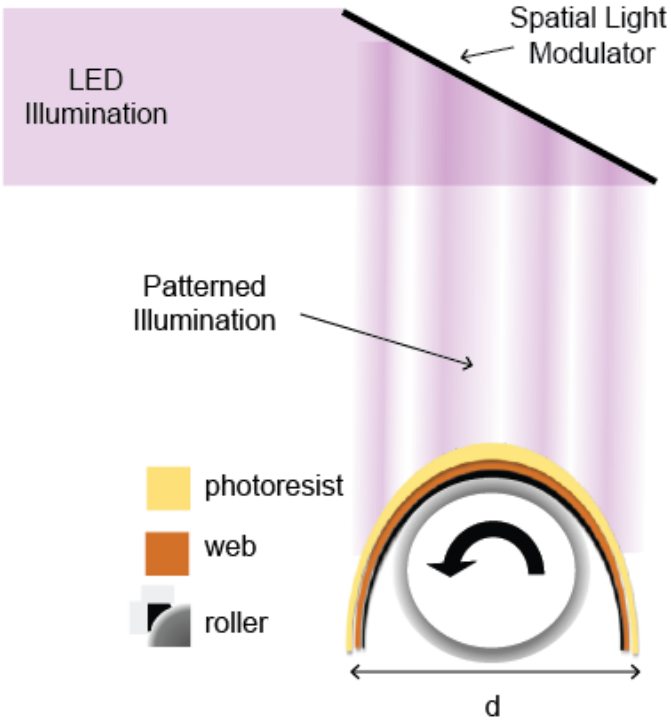

Figure 5-4 Simple schematic for the application of CAL to roll-to-roll patterning. Patterned illumination is directed toward a web of photoresist rolling over a roller. The roller modulates the relative angle between the incident illumination and the resist.

Application of CAL to roll-to-roll micro-/nano-patterning does present some significant challenges that would need to be addressed. For one, in the current

implementation of CAL, collimated light (infinite depth of focus) is assumed throughout the volume. In order to scale down to micro- or nano-scale lateral resolution, a much higher numerical aperture optical system would likely be required. This would result in much smaller depth of focus, which could be especially challenging to overcome when the substrate is curved rather than planar. Routes to addressing this challenge could include patterning using a smaller number of angles on a planar substrate or adjusting the focal depth laterally through the use of a microlens array with spatially varying focal length. Significant development steps remain but this does present a compelling future utilization of the CAL concept.

5.7 Closing Remarks

Overall, this thesis represents the conception and implementation of an entirely new class of additive manufacturing technologies. The results presented hint at the potential capabilities of volumetric fabrication for arbitrary geometries. Chapter 1 lays the basis for understanding incumbent AM methods, Chapter 2 explains the photochemistry, Chapters 3 and 4 introduce the new methods, and Chapter 5 lays out potential future directions. We believe that these technologies and this thesis are just the beginning in a new realm of additive manufacturing.

References

1. Dornfeld D, Lee D-E. Precision Manufacturing. Springer; 2008.
2. Dornfeld D. Course Lecture. Mechanical Engineering 220. Precision Manufacturing. Berkeley, CA;
3. Hull CW. Apparatus for production of three-dimensional objects by stereolithography. USA; US4575330, 1984.
4. ASTM International F42 Committee. Terminology for Additive Manufacturing Technologies. 2012.
5. Wang X, Xu S, Zhou S, Xu W, Leary M, Choong P, et al. Topological design and additive manufacturing of porous metals for bone scaffolds and orthopaedic implants: A review. Biomaterials. 2016 Mar;83:127–41.
6. Bhargav A, Sanjairaj V, Rosa V, Feng LW, Yh JF. Applications of additive manufacturing in dentistry: A review. J Biomed Mater Res Part B Appl Biomater. 106(5):2058–64.
7. Murphy S V, Atala A. 3D bioprinting of tissues and organs. Nat Biotechnol. 2014;32(8):773–85.
8. Gissibl T, Thiele S, Herkommer A, Giessen H. Two-photon direct laser writing of ultracompact multi-lens objectives. Nat Photonics. 2016 Aug 27;10(8):554–60.
9. Nguyen DT, Meyers C, Yee TD, Dudukovic NA, Destino JF, Zhu C, et al. 3D-Printed Transparent Glass. Adv Mater. 2017 Jul;29(26):1701181.
10. Vanderploeg A, Lee S-E, Mamp M. The application of 3D printing technology in the fashion industry. Int J Fash Des Technol Educ. 2017 May;10(2):170–9.
11. Gong H, Bickham BP, Woolley AT, Nordin GP. Custom 3D printer and resin for 18 μm × 20 μm microfluidic flow channels. Lab Chip. 2017 Aug 22;17(17):2899–909.
12. Ngo TD, Kashani A, Imbalzano G, Nguyen KTQ, Hui D. Additive manufacturing (3D printing): A review of materials, methods, applications and challenges. Compos Part B Eng. 2018 Jun;143:172–96.
13. Alexander C. Streamlining Automotive Production with Additive Manufacturing. Qual Troy. 2018 May;57(5):37–9.
14. Sachs E, Wylonis E, Allen S, Cima M, Guo H. Production of Injection Molding Tooling With Conformal Cooling Channels Using the Three Dimensional Printing Process. Polym Eng Sci. 2000;40(5):1232–47.
15. Pearce JM. Building Research Equipment with Free, Open-Source Hardware. Science (80-). 2012;337.
16. MacDonald E, Wicker R. Multiprocess 3D printing for increasing component functionality. Science (80-). 2016;353(6307).
17. Gibson I, Rosen DW, Stucker B. Design for Additive Manufacturing. In: Additive Manufacturing Technologies: Rapid Prototyping to Direct Digital Manufacturing. Boston, MA: Springer US; 2010. p. 299–332.
18. Valdevit L, Jacobsen AJ, Greer JR, Carter WB. Protocols for the Optimal Design of Multi-Functional Cellular Structures: From Hypersonics to Micro-Architected Materials. Pollock TM, editor. J Am Ceram Soc. 2011 Jun;94:s15–

34.
19. Zheng X, Smith W, Jackson J, Moran B, Cui H, Chen D, et al. Multiscale metallic metamaterials. Nat Mater. 2016 Oct 18;15(10):1100–6.
20. Jang T-S, Jung H-D, Pan H, Tun Han W, Chen S, Song J. 3D printing of hydrogel composite systems: Recent advances in technology for tissue engineering. Vol. 4, International Journal of Bioprinting. 2018.
21. Zhang X, Jiang XN, Sun C. Micro-stereolithography of polymeric and ceramic microstructures. Sensors and Actuators. 1999;77:149–56.
22. Choong YYC, Maleksaeedi S, Eng H, Wei J, Su P-C. 4D printing of high performance shape memory polymer using stereolithography. Mater Des. 2017 Jul 15;126:219–25.
23. Williams JM, Adewunmi A, Schek RM, Flanagan CL, Krebsbach PH, Feinberg SE, et al. Bone tissue engineering using polycaprolactone scaffolds fabricated via selective laser sintering. Biomaterials. 2005;26:4817–27.
24. Ganeriwala R, Zohdi TI. A coupled discrete element-finite difference model of selective laser sintering. Granul Matter. 2016;18(21).
25. Zein I, Hutmacher DW, Cheng Tan K, Teoh SH. Fused deposition modeling of novel scaffold architectures for tissue engineering applications. Biomaterials. 2002;23:1169–85.
26. Crump SS. Apparatus and method for creating three-dimensional objects. US5121329A, 1989.
27. Lewis JA. Direct Ink Writing of 3D Functional Materials. Adv Funct Mater. 2006 Nov 3;16(17):2193–204.
28. Chandrasekaran S, Duoss EB, Worsley MA, Lewicki JP. 3D printing of high performance cyanate ester thermoset polymers. J Mater Chem A. 2018;6:853–8.
29. Deubel M, Von Freymann G, Wegener M, Pereira S, Busch K, Soukoulis CM. Direct laser writing of three-dimensional photonic-crystal templates for telecommunications. Nat Mater Lett. 2004;444–7.
30. Thiel M, Fischer J, Von Freymann G, Wegener M. Direct laser writing of three-dimensional submicron structures using a continuous-wave laser at 532 nm. Appl Phys Lett. 2010;97(22):1–4.
31. Schmidt V, Kuna L, Satzinger V, Houbertz R, Jakopic G, Leising G. Application of two-photon 3D lithography for the fabrication of embedded ORMOCER (R) waveguides - art. no. 64760P. Optoelectron Integr Circuits IX. 2007;6476:P4760.
32. Chichkov BN, Ostendorf A. Two-Photon Polymerization: A New Approach to Micromachining. Photonics Spectra. 2006;40(October):72–79.
33. Infuehr R, Pucher N, Heller C, Lichtenegger H, Liska R, Schmidt V, et al. Functional polymers by two-photon 3D lithography. Appl Surf Sci. 2007;254:836–40.
34. Highley CB, Rodell CB, Burdick JA. Direct 3D Printing of Shear-Thinning Hydrogels into Self-Healing Hydrogels. Adv Mater. 2015 Sep;27(34):5075–9.
35. Sun C, Fang N, Wu DM, Zhang X. Projection micro-stereolithography using digital micro-mirror dynamic mask. Sensors Actuators A Phys. 2005 May 31;121(1):113–20.

36. Zheng X, Deotte J, Alonso MP, Farquar GR, Weisgraber TH, Gemberling S, et al. Design and optimization of a light-emitting diode projection micro-stereolithography three-dimensional manufacturing system. Rev Sci Instrum. 2012;83(2012):0–6.
37. Gauvin R, Chen YC, Lee JW, Soman P, Zorlutuna P, Nichol JW, et al. Microfabrication of complex porous tissue engineering scaffolds using 3D projection stereolithography. Biomaterials. 2012;33(15):3824–34.
38. Zhou C, Chen Y, Yang Z, Khoshnevis B. Digital material fabrication using mask-image-projection-based stereolithography. Rapid Prototyp J. 2013 Apr 19;19(3):153–65.
39. Dean D, Wallace J, Siblani A, Wang MO, Kim K, Mikos AG, et al. Continuous digital light processing (cDLP): Highly accurate additive manufacturing of tissue engineered bone scaffolds. Virtual Phys Prototyp. 2012 Mar;7(1):13–24.
40. Wallace J, Wang MO, Thompson P, Busso M, Belle V, Mammoser N, et al. Validating continuous digital light processing (cDLP) additive manufacturing accuracy and tissue engineering utility of a dye-initiator package. Biofabrication. 2014 Jan 15;6(1):015003.
41. Dendukuri D, Panda P, Haghgooie R, Kim JM, Hatton TA, Doyle PS. Modeling of oxygen-inhibited free radical photopolymerization in a PDMS microfluidic device. Macromolecules. 2008;41:8547–56.
42. O'Brien AK, Bowman CN. Impact of oxygen on photopolymerization kinetics and polymer structure. Macromolecules. 2006;39(7):2501–6.
43. Tumbleston JR, Shirvanyants D, Ermoshkin N, Janusziewicz R, Johnson AR, Kelly D, et al. Continuous Liquid Interface Production of 3D Objects. Science (80-). 2015;347(6228):1349–52.
44. Janusziewicz R, Tumbleston JR, Quintanilla AL, Mecham SJ, DeSimone JM. Layerless fabrication with continuous liquid interface production. Proc Natl Acad Sci U S A. 2016 Oct 18;113(42):11703–8.
45. Johnson AR, Caudill CL, Tumbleston JR, Bloomquist CJ, Moga KA, Ermoshkin A, et al. Single-Step Fabrication of Computationally Designed Microneedles by Continuous Liquid Interface Production. Yamamoto M, editor. PLoS One. 2016 Sep 8;11(9):e0162518.
46. Lin Y, Harb A, Lozano K, Xu D, Chen KP. Five beam holographic lithography for simultaneous fabrication of three dimensional photonic crystal templates and line defects using phase tunable diffractive optical element. Opt Express. 2009 Sep 14;17(19):16625.
47. Ohlinger K, Lutkenhaus J, Arigong B, Zhang H, Lin Y. Spatially addressable design of gradient index structures through spatial light modulator based holographic lithography. J Appl Phys. 2013 Dec 7;114(21):213102.
48. Ning H, Pikul JH, Zhang R, Li X, Xu S, Wang J, et al. Holographic patterning of high-performance on-chip 3D lithium-ion microbatteries. Proc Natl Acad Sci U S A. 2015 May 26;112(21):6573–8.
49. Jacobs PF. Fundamentals of Stereolithography. In: solid freeform fabrication symposium. 1992. p. 196–211.
50. Jacobs PF. Rapid Prototyping & Manufacturing: Fundamentals of

StereoLithography.
51. Miller G a., Gou L, Narayanan V, Scranton a. B. Modeling of photobleaching for the photoinitiation of thick polymerization systems. J Polym Sci Part A Polym Chem. 2002;40(September 2001):793–808.
52. Fairbanks BD, Schwartz MP, Bowman CN, Anseth KS. Photoinitiated polymerization of PEG-diacrylate with lithium phenyl-2,4,6-trimethylbenzoylphosphinate: polymerization rate and cytocompatibility. Biomaterials. 2009 Dec;30(35):6702–7.
53. Bowman CN, Kloxin CJ. Toward an enhanced understanding and implementation of photopolymerization reactions. AIChE J. 2008;54(11):275–2795.
54. Fick A. On liquid diffusion. Poggendorffs Ann. 1855;94(59).
55. Einstein A. Über die von der molekularkinetischen Theorie der Wärme geforderte Bewegung von in ruhenden Flüssigkeiten suspendierten Teilchen. vol. 322,. Annalen der Physik; 1903. 549-560 p.
56. Laoire CO, Mukerjee S, Abraham KM, Plichta EJ, Hendrickson M a. Elucidating the mechanism of oxygen reduction for lithium-air battery applications. J Phys Chem C. 2009;113:20127–34.
57. Hecht E, Ganesan AR. Optics. Dorling Kindersley (India) Pvt. Ltd; 2008.
58. Goodman JW. Introduction to Fourier Optics. New York, NY: McGraw-Hill; 1996.
59. Wan X, Menon R. Proximity-effect correction for 3D single-photon optical lithography. Appl Opt. 2016;55(3):A1--A7.
60. Jenness NJ, Wulff KD, Johannes MS, Padgett MJ, Cole DG, Clark RL. Three-dimensional parallel holographic micropatterning using a spatial light modulator. Opt Express. 2008;16(20):15942–8.
61. Jenness NJ, Cole DG, Clark RL. Three-Dimensional Holographic Lithography Using a Spatial Light Modulator. Detc2008 Proc Asme Int Des Eng Tech Conf Comput Inf Eng Conf , Vol 4. 2009;783–7.
62. Jenness NJ, Hill RT, Hucknall A, Chilkoti A, Clark RL. A versatile diffractive maskless lithography for single-shot and serial microfabrication. Opt Express. 2010;18(11):11754–62.
63. Zhang Z, You Z, Chu D. Fundamentals of phase-only liquid crystal on silicon (LCOS) devices. Light Sci Appl. 2014;3(10):e213.
64. Meyer-Arendt JR. Introduction to Classical and Modern Optics. Addison-Wesley; 1994.
65. Waller L. Course Lecture. UC Berkeley Electrical Engineering 218A. Introduction to Optical Engineering. Berkeley, CA; 2014.
66. Gerchberg RW, Saxton WO. A practical algorithm for the determination of phase from image and diffraction plane pictures. Optik (Stuttg). 1972;35:237–46.
67. Zhang H, Xie J, Liu J, Wang Y. Elimination of a zero-order beam induced by a pixelated spatial light modulator for holographic projection. Appl Opt. 2009;48(30):5834–41.
68. Dunn W, Improso G, Leonard P, Hilario A, Tapang G. Zero Order Diffraction Suppression in a Phase-only Spatial Light Modulator via the GS Algorithm.

2014;(1):3–4.
69. Wong DWK, Chen G. Redistribution of the zero order by the use of a phase checkerboard pattern in computer generated holograms. Appl Opt. 2008;47(4):602–10.
70. Liang J, Wu S-Y, Fatemi FK, Becker MF. Suppression of the zero-order diffracted beam from a pixelated spatial light modulator by phase compression. Appl Opt. 2012;51(16):3294.
71. Ronzitti E, Guillon M, de Sars V, Emiliani V. LCoS nematic SLM characterization and modeling for diffraction efficiency optimization, zero and ghost orders suppression. Opt Express. 2012;20(16):17843.
72. Shabtay G. Three-dimensional beam forming and Ewald's surfaces. Opt Commun. 2003 Oct 15;226(1–6):33–7.
73. Whyte G, Courtial J. Experimental demonstration of holographic three-dimensional light shaping using a Gerchberg–Saxton algorithm. 117.
74. Dainty JC, Goodman JW, Parry G, McKechnie TS, Francon M, Ennos AE. Topics in Applied Physics. Laser Speckle and Relate Phenomena. Springer Berlin Heidelberg; 1975.
75. Willig KI, Harke B, Medda R, Hell SW. STED microscopy with continuous wave beams. Nat Methods. 2007 Nov 21;4(11):915–8.
76. Nägerl UV, Willig KI, Hein B, Hell SW, Bonhoeffer T. Live-cell imaging of dendritic spines by STED microscopy. Proc Natl Acad Sci U S A. 2008 Dec 2;105(48):18982–7.
77. Klar TA, Jakobs S, Dyba M, Egner A, Hell SW. Fluorescence microscopy with diffraction resolution barrier broken by stimulated emission. Proc Natl Acad Sci U S A. 2000 Jul 18;97(15):8206–10.
78. Mueller P, Thiel M, Wegener M. 3D direct laser writing using a 405 nm diode laser. Opt Lett. 2014;39(24):6847–50.
79. Wollhofen R, Katzmann J, Hrelescu C, Jacak J, Klar T a. 120 nm resolution and 55 nm structure size in STED-lithography. Opt Express. 2013;21(9):10831–40.
80. Scott TF, Kowalski BA, Sullivan AC, Bowman CN, McLeod RR. Two-color single-photon photoinitiation and photoinhibition for subdiffraction photolithography. Science. 2009 May 15;324(5929):913–7.
81. Forman DL, Cole MC, McLeod RR. Radical diffusion limits to photoinhibited superresolution lithography. Phys Chem Chem Phys. 2013 Sep 28;15(36):14862–7.
82. Hounsfield GN. Method and apparatus for measuring x- or {65 -radiation absorption or transmission at plural angles and analyzing the data. U.S.; 3,778,614, 1973.
83. Kastner J, Heinzl C. Integrated Imaging and Vision Techniques for Industrial Inspection. Springer, London; 2015. 227-250 p.
84. Kelly B, Bhattacharya I, Shusteff M, Panas RM, Taylor HK, Spadaccini CM. Computed Axial Lithography (CAL): Toward Single Step 3D Printing of Arbitrary Geometries. ArXiv. 2017 May 16;
85. Kelly BE, Bhattacharya I, Shusteff M, Taylor HK, Spadaccini CM. Computed Axial Lithography For Rapid Volumetric 3D Additive Manufacturing. In:

Proceedings of the 28th Annual Solid Freeform Fabrication Symposium, Austin, TX. 2017.
86. Bortfeld T, Bürkelbach J, Boesecke R, Schlegel W. Methods of image reconstruction from projections applied to conformation radiotherapy. Phys Med Biol. 1990;35(10):1423–1434.
87. Deshpande VS, Fleck NA, Ashby MF. Effective properties of the octet-truss lattice material. J Mech Phys Solids. 2001 Aug 1;49(8):1747–69.
88. Jia W, Gungor-Ozkerim PS, Zhang YS, Yue K, Zhu K, Liu W, et al. Direct 3D bioprinting of perfusable vascular constructs using a blend bioink. Biomaterials. 2016;106:58–68.
89. Hinton TJ, Jallerat Q, N. PR, Park HJ, Grodzicki MS, Shue H-J, et al. Three-dimensional printing of complex biological structures by freeform reversible embedding of suspended hydrogels. Sci Adv. 2015;1(9).
90. Knowlton S, Onal S, Yu CH, Zhao JJ, Tasoglu S. Bioprinting for cancer research. Trends Biotechnol. 2015;33(9):504–13.
91. Lim KS, Schon BS, Mekhileri N V., Brown GCJ, Chia CM, Prabakar S, et al. New Visible-Light Photoinitiating System for Improved Print Fidelity in Gelatin-Based Bioinks. ACS Biomater Sci Eng. 2016;2(10):1752–62.
92. Gaynor AT, Guest JK. Topology Optimization for Additive Manufacturing : Considering Maximum Overhang Constraint. 2014;(June):1–8.
93. Everton SK, Hirsch M, Stravroulakis P, Leach RK, Clare AT. Review of in-situ process monitoring and in-situ metrology for metal additive manufacturing. Mater Des. 2016 Apr 5;95:431–45.
94. Ligon SC, Liska R, Stampfl J, Gurr M, Mülhaupt R. Polymers for 3D Printing and Customized Additive Manufacturing. Chem Rev. 2017 Aug 9;117(15):10212–90.
95. Valint PL, McGee JA, Salamone JC, Ozark RM. Surface treatment of silicone medical devices with reactive hydrophilic polymers. US10005560, 1999.
96. Hamerton I. Chemistry and Technology of Cyanate Ester Resins. Springer; 1994.
97. Matthews MJ, Guss G, Drachenberg DR, Demuth JA, Heebner JE, Duoss EB, et al. Diode-based additive manufacturing of metals using an optically-addressable light valve. Opt Express. 2017 May 15;25(10):11788.
98. Lee JW, Lee IH, Cho DW. Development of micro-stereolithography technology using metal powder. Microelectron Eng. 2006;83(4–9 SPEC. ISS.):1253–6.
99. Ng R, Levoy M, Bredif M, Duval G, Horowitz M, Hanrahan P. Light Field Photography with a Hand-held Plenoptic Camera. 2005.
100. Lanman D, Luebke D. Near-Eye Light Field Displays. ACM Trans Graph. 2013;32(6).
101. Tan H, Gilbertson A, Chou SY. Roller nanoimprint lithography. J Vac Sci Technol B. 1998;16(6):3926–8.
102. Ahn SH, Guo LJ. Large-area roll-to-roll and roll-to-plate nanoimprint lithography: a step toward high-throughput application of continuous nanoimprinting. ACS Nano. 2009;3(8):2304–10.
103. Lim H, Choi KB, Kim G, Lee S, Park H, Ryu J, et al. Roll-to-roll nanoimprint lithography for patterning on a large-area substrate roll. Microelectron Eng.

2014;123:18–22.
104. Pudas M, Halonen N, Granat P, Vähäkangas J. Gravure printing of conductive particulate polymer inks on flexible substrates. Prog Org Coatings. 2005 Dec 1;54(4):310–6.
105. Lee SH, Lee JH, Park C, Kwak MK. Roll-type photolithography for continuous fabrication of narrow bus wires. J Micromechanics Microengineering. 2016 Nov 1;26(11):115008.
106. Ok JG, Kwak MK, Huard CM, Youn HS, Guo LJ. Photo-Roll Lithography (PRL) for Continuous and Scalable Patterning with Application in Flexible Electronics. Adv Mater. 2013 Dec 1;25(45):6554–61.